DYADIC BEHAVIOR IN CO-MANIPULATION: FROM HUMANS TO ROBOTS

Waldez Azevedo Gomes Júnior

Dissertação de Mestrado apresentada ao Programa de Pós-graduação em Engenharia Elétrica, COPPE, da Universidade Federal do Rio de Janeiro, como parte dos requisitos necessários à obtenção do título de Mestre em Engenharia Elétrica.

Orientador: Fernando Cesar Lizarralde

Rio de Janeiro
Abril de 2018

DYADIC BEHAVIOR IN CO-MANIPULATION: FROM HUMANS TO ROBOTS

Waldez Azevedo Gomes Júnior

DISSERTAÇÃO SUBMETIDA AO CORPO DOCENTE DO INSTITUTO ALBERTO LUIZ COIMBRA DE PÓS-GRADUAÇÃO E PESQUISA DE ENGENHARIA (COPPE) DA UNIVERSIDADE FEDERAL DO RIO DE JANEIRO COMO PARTE DOS REQUISITOS NECESSÁRIOS PARA A OBTENÇÃO DO GRAU DE MESTRE EM CIÊNCIAS EM ENGENHARIA ELÉTRICA.

Examinada por:

Prof. Fernando Cesar Lizarralde, D.Sc.

Prof. Carlos Julio Tierra Criollo, D.Sc.

Prof. Antônio Padilha Lanari Bó, Ph.D.

RIO DE JANEIRO, RJ – BRASIL
ABRIL DE 2018

Gomes Júnior, Waldez Azevedo

Dyadic Behavior in Co-Manipulation: From Humans to Robots/Waldez Azevedo Gomes Júnior. – Rio de Janeiro: UFRJ/COPPE, 2018.

XIX, 105 p.: il.; 29, 7cm.

Orientador: Fernando Cesar Lizarralde

Dissertação (mestrado) – UFRJ/COPPE/Programa de Engenharia Elétrica, 2018.

Referências Bibliográficas: p. 79 – 91.

1. Co-Manipulation. 2. Human-Robot Collaboration. 3. Human Motor Behavior. 4. Adaptive Admittance Control. 5. Human in the Loop. 6. Electromyography. I. Lizarralde, Fernando Cesar. II. Universidade Federal do Rio de Janeiro, COPPE, Programa de Engenharia Elétrica. III. Título.

Aos meus pais Waldez e Valdires
e às minhas irmãs Crisane,
Carolina e Cristiane

Acknowledgments

Firstly, I would like to thank my parents, Waldez and Valdires, who are not only always supportive of my academic endeavors, but are also a constant example of perseverance.

I would like to thank my sisters, Crisane, Carolina, and Cristiane, that are always there to share their life experiences. And I give a special thanks to Cristiane who was able to be present on my presentation.

I would like to thank my girlfriend, Lidia, for making my days lighter and easier even when life gets tough.

I would like to thank all of the students I met during my time as a master student in UFRJ, and I give a special thanks to Raphael, Jéssica, Pâmela, Rodrigo, Jonathan, and Thaís for simply being great friends at all times, for every occasion.

I would like to thank Danilo for the rides from home to university, and the occasional brainstorms on the way to the lab.

I would like to thank Dr. Serena Ivaldi, and Dr. Pauline Maurice for guiding me through unsailed waters, introducing me to human-robot collaboration, helping me with the experiments design, and with the text review.

I would like to thank COPPE/UFRJ for the scholarship awarded to me, and for the world class education and experience I received from all of my professors. Especially, I would like to thank my advisor, Prof. Fernando Lizarralde, for the robotics classes, the recommendations, the advices, and mentoring throughout this work.

Resumo da Dissertação apresentada à COPPE/UFRJ como parte dos requisitos necessários para a obtenção do grau de Mestre em Ciências (M.Sc.)

COMPORTAMENTO DIÁDICO DURANTE CO-MANIPULAÇÃO: DE HUMANOS PARA ROBÔS

Waldez Azevedo Gomes Júnior

Abril/2018

Orientador: Fernando Cesar Lizarralde

Programa: Engenharia Elétrica

Para tanto diminuir o esforço físico de um humano, quanto aumentar a percepção de um ambiente por um robô, um díade humano-robô pode ser usado para co-manipulação de um objeto compartilhado.

Partindo da premissa de que humanos são eficientes trabalhando juntos, a abordagem deste trabalho é a de investigar díades humano-humano co-manipulando um objeto compartilhado. A co-manipulação é avaliada a partir de dados de um sistema de captura de movimentos, sinais de eletromiografia (EMG), e de sensores de contato customizados para análise qualitativa de desempenho.

Um experimento de co-manipulação com díades humano-humano foi projetado no qual cada humano é instruído a se comportar como um líder, um seguidor, ou simplesmente agir tão naturalmente quanto possível. A análise de dados do experimento revelou que os humanos modulam a rígidez mecânica do braço a depender de que tipo de comportamento eles foram designados antes da co-manipulação.

Para emular o comportamento humano durante uma tarefa de co-manipulação, um controle por admitância com rigidez variável é apresentado neste trabalho. A rigidez desejada é continuamente variada com base em uma função escalar suave que define o grau de liderança do robô. Além disso, o controlador é analisado por meio de simulações, e sua estabilidade é analisada pela teoria de Lyapunov. As trajetórias resultantes do uso do controlador mostraram um padrão de comportamento muito parecido ao do experimento com díades humano-humano.

Abstract of Dissertation presented to COPPE/UFRJ as a partial fulfillment of the requirements for the degree of Master of Science (M.Sc.)

DYADIC BEHAVIOR IN CO-MANIPULATION: FROM HUMANS TO ROBOTS

Waldez Azevedo Gomes Júnior

April/2018

Advisor: Fernando Cesar Lizarralde

Department: Electrical Engineering

To both decrease the physical toll on a human worker, and increase a robot's environment perception, a human-robot dyad may be used to co-manipulate a shared object.

From the premise that humans are efficient working together, this work's approach is to investigate human-human dyads co-manipulating an object. The co-manipulation is evaluated from motion capture data, surface electromyography (EMG) sensors, and custom contact sensors for qualitative performance analysis.

A human-human dyadic co-manipulation experiment is designed in which every human is instructed to behave as a leader, as a follower or neither, acting as naturally as possible. The experiment data analysis revealed that humans modulate their arm mechanical impedance depending on their role during the co-manipulation.

In order to emulate the human behavior during a co-manipulation task, an admittance controller with varying stiffness is presented. The desired stiffness is continuously varied based on a scalar and smooth function that assigns a degree of leadership to the robot. Furthermore, the controller is analyzed through simulations, its stability is analyzed by Lyapunov. The resulting object trajectories greatly resemble the patterns seen in the human-human dyad experiment.

Contents

List of Figures

List of Tables

List of Symbols

C	Coriolis matrix, p. 24
D_d	Desired damping matrix, p. 25
F_c	Forces at the end-effector correspondent to τ_c, p. 25
F_g	Forces at the end-effector correspondent to g, p. 25
F_h	Human force applied at the EEF, p. 55
F_{ext}	External forces vector, p. 24
I_n	Identity matrix of n order, p. 61
$J(q)$	Geometric Jacobian, p. 18
$J^\dagger$	Jacobian moore-penrose pseudo inverse, p. 19
$J_o(q)$	Orientation Jacobian, p. 18
$J_p(q)$	Position Jacobian, p. 18
$J_r(\phi)$	Representation Jacobian, p. 19
J_{on}	n-th column of the orientation Jacobian, p. 18
J_{pn}	n-th column of the position Jacobian, p. 18
K_d	Desired stiffness matrix, p. 25
K_h	Human endpoint stiffness, p. 56
K_p	Kinematic control feedback proportional gain, p. 22
K_{d0}	Maximum variation of desired stiffness, p. 55
K_{d1}	Minimum desired stiffness, p. 55
K_{h0}	Maximum human endpoint stiffness, p. 56

M	Inertia matrix, p. 24
$R_k(\alpha)$	Rotation matrix that applies a rotation around an axis $\vec{k}$, by an angle of α, p. 13
Λ	Apparent inertia, p. 25
Λ_d	Desired apparent inertia matrix, p. 25
β	Parameter matrix for the Lyapunov candidate function V_2, p. 104
γ	Scalar parameter for stability analysis, p. 58
$\lambda_{MAX}(\cdot)$	Maximum eigenvalue operator, p. 58
$\lambda_{min}(\cdot)$	Minimum eigenvalue operator, p. 58
$\mathcal{F}_a$	Orthonormal cartesian frame a with unit vectors $\vec{x_a}, \vec{y_a}, \vec{z_a}$, p. 12
$\mathcal{I}$	Vector identity operator, p. 18
$\mathcal{N}(\cdot)$	Null space operator, p. 19
$\mathcal{Q}$	Quaternion, p. 14
$\mathcal{Q}^*$	Quaternion conjugate, p. 14
$\mathcal{Q}_s$	Quaternion scalar component, p. 14
$\mathcal{Q}_v$	Quaternion vector component, p. 14
$\mathcal{R}(\cdot)$	Range or column space operator, p. 23
μ	Coriolis matrix in operational space, p. 25
ν	Control signal for secondary goals in redundant kinematic control, p. 23
ω_e	End-effector angular velocity, p. 18
ϕ_e	End-effector orientation representation with respect to frame $\mathcal{F}_B$, p. 17
σ_m	m-th singular value of J, p. 21
τ_c	Control torque, p. 24

$\vec{u}_m$	m-th eigenvector of $JJ^\top$, p. 21
${}^aR_o$	Rotation matrix from $\mathcal{F}_o$ to $\mathcal{F}_a$, p. 12
e	Kinematic controller tracking error, p. 22
e_h	Human desired trajectory error, p. 54
e_o	Kinematic controller orientation tracking error, p. 22
e_p	Kinematic controller position tracking error, p. 22
e_r	Robot trajectory error, p. 25
$f(\cdot)$	Forward kinematic operator, p. 17
g	Gravitational torque at the robot joints, p. 24
icc^s_{fol}	ICC value for a subject s behaving as a follower in the dyad, p. 45
icc^s_{lead}	ICC value for a subject s behaving as a leader in the dyad, p. 45
icc^s_{nat}	ICC value for a subject s behaving without any pre-assigned behavior, p. 45
icc_k	Index of Co-Contraction with respect to human joint k, p. 35
icc_{max}	Maximum ICC, p. 54
icc_{min}	Minimum ICC, p. 54
p_e	End-effector position with respect to frame $\mathcal{F}_B$, p. 17
q_i	Robot joint variable i, p. 17
u	Kinematic control signal, p. 22
u_c	Control signal for impedance control, p. 26
u^i_{fil}	Filtered EMG signal for a muscle i, p. 34
u^i_{norm}	Normalized EMG signal for a muscle i, p. 34
u_{raw}	Raw EMG signal, p. 31
v_e	End-effector velocity, p. 18
x_e	End-effector pose with respect to frame $\mathcal{F}_B$, p. 17

x_r	Desired robot trajectory, p. 25
x_{ref}	end-effector reference pose trajectory, p. 22
${}^aT_b$	Homogeneous transformation from $\mathcal{F}_b$ to $\mathcal{F}_a$, p. 16
${}^ap_b$	Position coordinates of frame $\mathcal{F}_b$ with respect to $\mathcal{F}_a$, p. 15
SE(n)	n-Dimensional Special Euclidean Group, p. 15
SO(n)	n-Dimensional Special Orthonormal Group, p. 12

List of Abbreviations

BIC	Biceps, p. 42
DA	Deltoid Anterior, p. 42
DP	Deltoid Posterior, p. 42
DoF	Degrees of Freedom, p. 19
ECR	Extensor Carpi Ulnaris, p. 42
EEF	End-effector, p. 11
EMG	Electromyography, p. 2
EoM	Equation of Motion, p. 11
FCR	Flexor Carpi Ulnaris, p. 42
FES	Functional Electrical Stimulation, p. 34
HH	Human-Human, p. 3, 6
HRC	Human-robot collaboration, p. 1
HR	Human-Robot, p. 3
IAD	Intelligent Assistive Device, p. 5
ICC	Index of Co-Contraction, p. 28
MU	Motor Unit, p. 28
MVC	Maximum Voluntary Contraction, p. 32
RMS	Root Mean Square, p. 32
RR	Robot-Robot, p. 3
SSH	Secure Shell, p. 42

TCP Tool Control Point, p. 2

TRI Triceps, p. 42

Chapter 1

Introduction

Robots have been very successful automatizing daily tasks with different levels of complexity in varied industries. Nowadays, it is common to see robots executing tasks such as picking and placing parts or assembling/sorting products in factories, which essentially require robot capabilities such as power generation, precision and repeatability. On the other hand, there are also tasks that will require human cognition, perception, and learning capabilities. Depending on the task it could be very challenging to implement those skills in robots. A solution to this dilemma may include humans and robots mutually collaborating towards the execution of a common task. Furthermore, aside from usual applications in industrial environments, robots can also be used to aid humans in fine manipulation scenarios, like in robot-assisted surgeries for instance (Enayati *et al.*, 2016; Hoeckelmann *et al.*, 2015).

Human-robot collaboration (HRC) also provides advantages that go beyond mere task execution. From the human operator standpoint, HRC may allow the user to profit from less fatigue, stress, and incidence of musculoskeletal disorders (MSDs) (Punnett and Wegman, 2004), especially when the robot design and control take into consideration the human biomechanical ergonomics (Bestick *et al.*, 2015; Busch *et al.*, 2017; Maurice, 2015). Small and medium sized factories with production flexibility requirements may also greatly benefit from HRC (Michalos *et al.*, 2015) since their human workers would not need to be separated from the robots, resulting in less constraints for work cell organization, and more flexibility at the factory floor.

Some issues also arise from the use of robots in the same workspace as humans. For instance, safe and dependable robot architectures are an absolute necessity (Santis *et al.*, 2008) since robots are usually able to generate much more physical power and could potentially harm human beings. In addition, the robot control design has to consider the human workers' comfort, and intuitive human-robot interactions, so that the human workers feel comfortable when working alongside robots, and that there will not be additional causes for psychological stress to the humans, or even additional disturbances for the execution of tasks.

Figure 1.1: From isolated robots in the past, to robots and humans coexisting nowadays, and robots and humans seamlessly collaborating in the future (Siciliano and Khatib, 2016)

1.1 Human-Robot Collaboration

HRC has advanced greatly in the recent past, and it is expected for it to advance even further in the future (fig. 1.1). In order for that to happen, there are several topics currently in active research that are extremely relevant, which include: safety; motion intention communication; and physical interaction stability.

1.1.1 Safety

Recently, many safety standards have been developed to take into account tasks where robots are at least in the same work environment as humans. They impose dynamic and kinematic constraints at the tool control point (TCP) of the robot, as well as control system performance, robot stopping functions, collision avoidance, and other safety constraints (Fryman and Matthias, 2012; Matthias *et al.*, 2011; Michalos *et al.*, 2015). Along with the evolution of the safety standards there have been also advances in hardware actuation safety (Bicchi *et al.*, 2005; Vanderborght *et al.*, 2013).

1.1.2 Physical Interaction Stability

The stability in human-robot co-manipulation is heavily dependent on the human limb stiffness, which can be estimated by bio-signals like voltage measures from electromyography (EMG) sensors placed on the human skin (Gallagher *et al.*, 2014). The human natural behavior is to modulate his/her endpoint Cartesian stiffness in the presence of instability (Burdet *et al.*, 2001; Franklin *et al.*, 2007, 2008) while executing accurate tasks (Osu and Gomi, 1999). For this reason, some works have

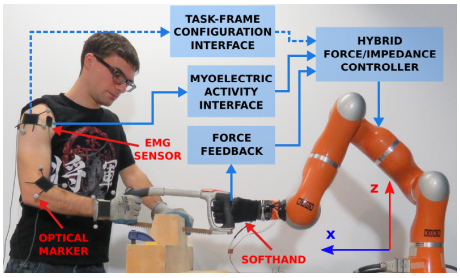

(a) (Peternel *et al.*, 2017)

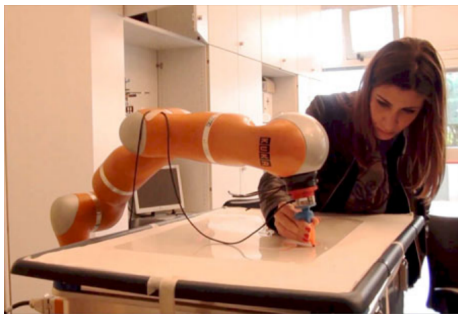

(b) (Ficuciello *et al.*, 2014)

Figure 1.2: Human robot dyads physically coupled

adapted the stiffness of robots based on a human stiffness estimation through EMG signals (Ajoudani *et al.*, 2014, 2015; Gallagher *et al.*, 2014; Grafakos *et al.*, 2016; Li *et al.*, 2017; Peidong Liang and Li, 2016). It is also possible to measure human stiffness by measuring force/displacement at the TCP (Tsumugiwa *et al.*, 2002).

In lieu of human arm stiffness estimation, Dimeas and Aspragathos (2016) proposed an instability index that monitors high frequency oscillations at the TCP. In Gopinathan *et al.* (2017), the authors propose a similar solution to Dimeas and Aspragathos (2016) that also varies the stiffness online, but the variation is dependent on personalized force measures acquired for each user. In their experiments, the personalized stiffness adaptation strategy was associated with good trajectory tracking and interaction force stability for more complex tasks, while the fixed medium stiffness strategy showed good performance for simpler tasks. Further analysis of their results also indicated that the manipulability (Yoshikawa, 1985) of the human arm is closely related to a good execution of the task.

1.1.3 Motion Intention Communication

In order to achieve an efficient HRC, a robot should be aware of all agents that take part in the system: the environment, other robots, objects to be physically manipulated, and human partners.

In the case of a physically coupled human-robot dyad (HR-dyad) [1] (fig. 1.2), which will be the case for the remainder of this section unless stated otherwise, the physical interaction between the partners is usually based on a multimodal communication that comprehends both the physical task, and information to advise the partners about the ongoing action (Jarrassé *et al.*, 2014).

To comprehend the human partner, in the robot perspective, it is to understand what the partner is doing, and possibly to be able to predict his/her motion intentions from the multimodal exchange. Consequently, HRC demands an anticipatory

[1] Dyad: A pair of partners. It may be a Human-Human (HH), Human-Robot (HR), or Robot-Robot (RR) dyad

model of the human dynamics (Bandyopadhyay *et al.*, 2013; Dermy *et al.*, 2017). This may allow the robot to learn from the human's actions or execute actions of its own according to the human's feedback. Studies on dyad physical interaction (Dumora *et al.*, 2012; Reed, 2012) have observed that force/pressure information is insufficient to determine intention of motion. But in spite of that, most works use only force/pressure sensors in contact to the human partner to model human intentions or to control the robot with impedance (or admittance) control strategies (Agravante *et al.*, 2014; Ajoudani *et al.*, 2017b; Duchaine and Gosselin, 2007; Gribovskaya *et al.*, 2011; Peternel and Babič, 2013; Rozo *et al.*, 2014).

The robot may use the information regarding the human intention of motion to produce actions that establish HR communication patterns. If those actions are recognizable as natural and intuitive to the human partner, they are also said to be legible (Bauer *et al.*, 2008; Dragan *et al.*, 2013; Jarrassé *et al.*, 2014; Klingspor *et al.*, 1997; Stulp *et al.*, 2015; Zhou *et al.*, 2017). Dragan *et al.* (2015) defined a legible motion as a functional motion that enables the human partner to quickly and confidently infer the robot's goal. The results of their study suggested that legible motions lead to more fluent collaborations in comparison to purely functional motions, or predictable motions (that match prior human expectations).

Recently, despite the studies in Dumora *et al.* (2012); Reed (2012), the new study in Mojtahedi *et al.* (2017) devised an experiment to study physical HH dyad communication without visual feedback (fig. 1.3). The study verified that HH dyads were able to communicate intended direction of movements by modulating directionally the Cartesian impedance of the dyad control point. These results indicated that legible motions are necessary for intuitive HRC, as much as legible impedance/admittance adaptation.

1.2 Partner's Roles in Dyad Collaboration

Communication among agents is therefore very important to the intuitiveness of HRC. Within the topic of dyadic HR co-manipulation, this work focuses closely on the leadership hierarchy relationship among agents in the dyad. There is still a lack of precise terminology on the distribution of roles in general HR interactions due to the complexity of the multimodal communications, nevertheless, Ong *et al.* (2008) identified 5 types of HR interaction : Master-slave, supervisor-subordinate, partner-partner, teacher-learner, and fully autonomous robot.

For this work, the relationship hierarchy is limited by the roles of leader and follower, which may be assigned to any of the agents in the dyad.

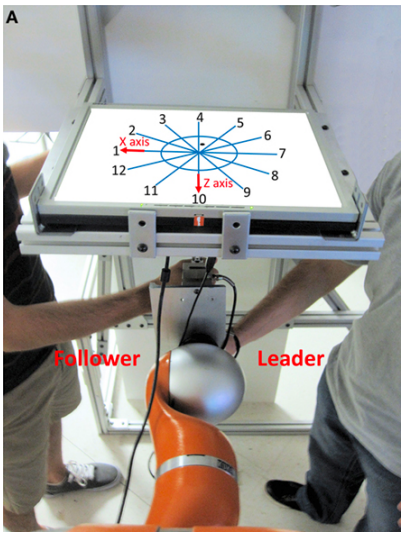

Figure 1.3: Experiment to evaluate human-human dyad communication of intention Mojtahedi *et al.* (2017)

1.2.1 Robot as a Follower

In some works, the robot (follower) in a HR dyad will act exclusively upon commands from the human operator (leader). Many applications have been developed with this role assignment, most notably robots that are able to assist humans in lifting and carrying heavy or bulky parts/objects (Kosuge and Hirata, 2004). In this category, there are exoskeletons that augment the human's physical capabilities (Dollar and Herr, 2008; Kazerooni *et al.*, 2005), and intelligent assistive devices (IADs) (Colgate *et al.*, 2003), or cobots (collaborative robots) as defined by Colgate *et al.* (1996), that not only constrain and guide the motion of a human partner, but also decrease the human efforts.

Other more sophisticated control strategies include the work in Ficuciello *et al.* (2014, 2015), where there is a Cartesian impedance adaptation that explores the null-space dynamics matrix of a redundant robot in order to decouple the apparent inertia at the TCP, reportedly improving the intuitiveness of the task for the human leader.

1.2.2 Robot as a Leader or a Follower

Most of the research in dyadic HR co-manipulation has focused on control strategies that assign the robot exclusively as a follower to the human agent. However, Jarrassé *et al.* (2014) suggest that more efficient collaboration could be achieved by switching the robot's role between leader or follower at some points in time, resulting in a symmetric relationship overall.

Cherubini *et al.* (2016) swaps the usual roles, assigning the robot as leader, giving the robot its own trajectory to track, but it also enables the robot to deviate from

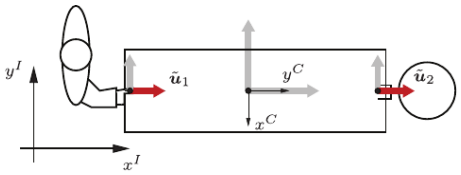

(a) Equal Share of the Voluntary Effort

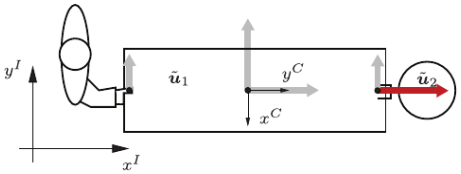

(b) Robot Takes All of the Voluntary Effort

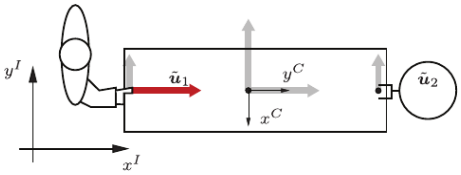

(c) Human Takes All of the Voluntary Effort

Figure 1.4: Dynamic role allocation (Mörtl *et al.*, 2012)

its own trajectory based on visual and haptic cues communicated by the human partner. The robot calculates the deviation based on an admittance control used by a regular robot with position controlled joints. Likewise, this robot application also features robot-environment interactions, trajectory optimization to help the human partner throughout the entire task and not just compensate the weight like in some IADs. In Navarro *et al.* (2016), the authors use an adaptive admittance control law, that like in Cherubini *et al.* (2016) also requires compliance to the standard ISO10218-1 (ISO, 2006).

Mörtl *et al.* (2012) developed dynamic role allocation strategies that continuously share the required effort (force/torque) among the partners in a dyad that cooperatively manipulated a table. The role allocation, described the leadership as a matter of voluntary effort in a preset direction that is redundant for both partners, that is, each partner could act in the redundant direction independently. If one of the partners was to act solely as a leader of the task, the entire required effort would be expected of the leader (fig. 1.4). The dynamic role allocation strategies were compared to fixed role strategies. But even though dynamic role allocation had better quantitative measures, the subjective measures (questionnaires to the experiment subjects) suggest that their fixed role allocation strategy was more intuitive.

The idea that both partners in the dyad behave between the extremes of pure leader or pure follower is also explored in Evrard and Kheddar (2009a,b) using an homotopy (interpolation) between two distinct controllers. The authors followed up by developing a human-human (HH) experiment to lift a table, in which a probabilistic framework based on a gaussian mixture model learned how the robot should

act as a pure leader and as a pure follower by looking at the robot force and velocity at the TCP. Then, the authors used a gaussian mixture regression to apply the homotopy between both extremes into the homotopy controller for the robot (Evrard *et al.*, 2009). However, the reproduction of the task did not seem to be in agreement with the human-human dyads, especially lacking adaptability to different human motor behaviors from the ones previously learned.

In Li *et al.* (2015a,b) the authors approach the problem by modeling it as a two player game (human and robot as players). Then, a role adaptation law based on game theory is implemented. One boundary condition gives total control of the task to the robot, and the other to the human.

Whitsell and Artemiadis (2017) introduced the concept of asymmetric collaboration, where the leader/follower roles could be independently exchanged in 6 degrees of freedom. The human would be needed to correct the TCP trajectory every now and then, and the robot would change from leader to follower in the required degrees of freedom. Instead of an interpolation-like strategy from leader to follower boundaries, they used three different states: robot as leader; intermediate; and robot as follower;

In addition to role exchange and robot control, Beton *et al.* (2017) also investigated the impact that each one of the roles (leader/follower) have on the human's perception of the robot competence and safety towards the human. The preliminary results seem to indicate that the assignment of the follower role to the robot influences the human to view the robot as more knowledgeable and competent.

1.2.3 Human-Human Co-Manipulation

The major problem with the role-exchange strategies mentioned above is that they are mostly heuristics based on knowledge of human motor control for individual manipulation only. A HH dyad co-manipulation requires planning and coordination from two different persons that, just as in the HR case, are constantly communicating through various kinds of information channels (visual, haptic, etc.). This is much more complicated than an individual manipulation. For a HR dyad to behave as natural as a HH dyad behaves, the robot has to know what kinds of information to look for in the human partner, and most importantly, how to adapt to it in a way that is natural to the human partner. To do that, it is of the utmost importance to analyze and extract information on natural HH dyad behavior. The works in Noohi *et al.* (2016); Takagi *et al.* (2017) are examples of HH dyad studies that lead to HRC applications.

In van der Wel *et al.* (2011) the authors designed an experiment to compare a task that could be executed by an individual or by a physically coupled HH dyad. They

observed that the HH dyad exerted higher forces at the shared object, suggesting that HH dyads communicate haptically throughout the task execution. This result is in accordance with Reed (2012) that also verified this increase in force in a HH dyad related to haptic communication, along with faster times of execution for the HH dyad.

Melendez-Calderon *et al.* (2011) explored, and classified how human dyads modulated their mechanical impedance while physically coupled in order to attenuate disturbances and ensure interaction stability. Notwithstanding, as previously mentioned, Mojtahedi *et al.* (2017) investigated the haptic communication not only as a function of the interaction force, but also as modulation of Cartesian impedance.

In Townsend *et al.* (2017), the authors trained a neural network to predict intentions of motions based on an experiment where HH dyads manipulated a table. The neural network was trained using only motion data without wrench sensors at the human partners. In a HR experiment, it was able to predict the partner velocity up to .25s into the future.

It can be concluded that knowledge of dyadic HH behavior leads to better control strategies for robots in HRC.

1.3 Objectives

It is still an open question in the human motor behavior scientific community how humans work together to co-manipulate objects. This work aims to understand how leader/follower roles are naturally distributed in a HH dyad, which signals can be used to infer the distribution, and how this distribution can be efficiently reproduced in a robot within a HR dyad.

To this matter, the *first objective* of this work is to investigate the behavior of HH dyads manipulating an object. Thus, making it possible to infer what is a natural behavior to a HH dyad regarding dynamic role exchange among the dyad agents.

The *second objective* is to develop a robot controller for a HR co-manipulation scenario (fig. 1.5) based on the findings from the first objective. This controller should be able to take into account the human partner kinematics/dynamics, and generate a human-like behavior.

1.4 Methodology

To achieve the *first objective*, a HH dyad experiment is designed to obtain information for different role assignments to the human agents. Every human agent behavior in the HH dyad co-manipulation experiment is analyzed by acquiring kinematic data

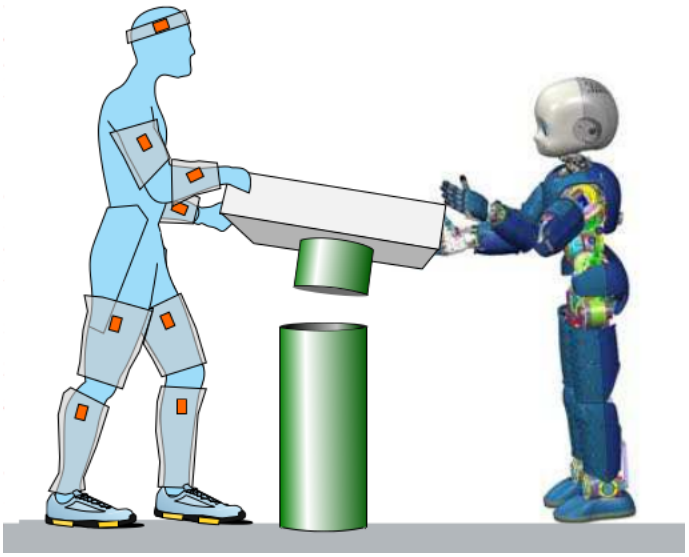

Figure 1.5: Human-robot dyad in a co-manipulation task

across time (trajectories), alongside stiffness estimations from EMG sinals, and performance metrics designed for the experiment. After preliminary results of the HH experiment, another experiment exhibiting only one human agent was designed to gather more information, especially on the hand trajectory.

Then, to achieve the *second objective*, the results of the human experiment are used to design an adaptive admittance controller that enables a robot to dynamically change its role in a HR dyad co-manipulation, from a total leader to a total follower. The controller is tested with numerical simulations for a planar robot and simulated human forces. Similar simulations are also employed with a 7 DoF robot in a simulator with a physics engine, and an additional experiment with a real robot is executed as well.

1.5 Contributions

The manipulation experiments verified that humans change their stiffness according to their role in a dyad that is co-manipulating an object. Moreover, their change in stiffness is associated with the tracking of its own desired trajectory for the manipulated object. The object trajectory is a blend of the desired trajectories from both agents in the dyad.

The results from the HH, and single human manipulation experiments served as inspiration for an adaptive admittance controller that adapts the robot stiffness and damping parameters according to an estimate of the human partner arm stiffness variation. This controller produced similar trajectories blending as in the HH exper-

iment. In addition, conditions for the global asymptotic stability of the controller equilibrium point are also devised here.

1.6 Organization

The remainder of this dissertation is organized as follows:

- Chapter 2: Describes fundamental concepts regarding modeling robot kinematics and dynamics; basic kinematic, and impedance/admittance controllers. It also presents the mathematical notation used in this dissertation;
- Chapter 3: Describes the nature of EMG signals, as well as guidelines to obtain the signal, and how it is usually processed. Furthermore, it also presents the concept of index of co-contraction;
- Chapter 4: Describes details regarding the design of the HH dyad co-manipulation experiment, and the single human manipulation experiment and their respective experiment protocols. Moreover, the data analysis is also shown in this chapter;
- Chapter 5: Describes the development of an admittance robot controller that allows the robot to automatically change its role in a manipulation task based on EMG signals from a human partner for instance. The controller is validated through simulations, and a real robot experiment with virtual human force;
- Chapter 6: Final considerations regarding this work and its results. It also proposes routes for future work.

Chapter 2

Robotic Manipulators Modeling and Control

This work describes a robotic manipulator as an open chain of rigid bodies (links) connected through revolute or prismatic joints. In order to execute a task, the manipulator needs a tool located at the end of the chain, which is named end-effector (EEF).

This chapter delves into how one can describe the EEF position and orientation (*pose*) with respect to a reference frame based on the configuration of the manipulator joints (*forward kinematics*). Then, the chapter follows by describing how the joint velocities and the EEF linear and angular velocities are related (*differential kinematics*), and how the EEF can track pose trajectories (*kinematic control*). Furthermore, it includes an analysis of redundancy, and how it can be used to improve the kinematic control.

This chapter also describes the dynamic equation of motion (EoM) of a manipulator and how to specify and control a relationship between a wrench (force and torque) applied at the EEF and the EEF pose using impedance or admittance control in the operational space (also known as Cartesian space).

2.1 Rigid Body Transformations

A rigid body is defined as a collection of particles with a fixed distance among any two particles regardless of any forces applied to the body, or any movements executed by the body (Murray *et al.*, 1994).

In other words, given any two particles in a rigid body with position trajectories $p(t) = (x_p(t), y_p(t), z_p(t))^\top \in \mathbb{R}^3$, and $q(t) = (x_q(t), y_q(t), z_q(t))^\top \in \mathbb{R}^3$, in which the coordinates are with respect to an inertial orthonormal cartesian frame $\mathcal{F}_a =$

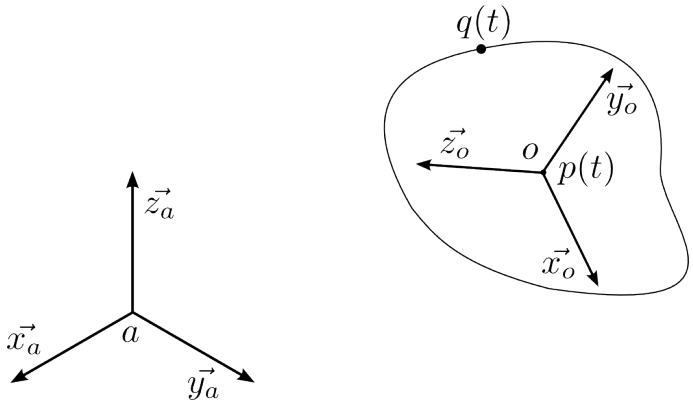

Figure 2.1: Inertial frame $\mathcal{F}_a$, and frame $\mathcal{F}_o$ attached to a rigid body

$(\vec{x_a}, \vec{y_a}, \vec{z_a})$ the following is valid:

$$\|p(t) - q(t)\| = \|p(0) - q(0)\|, \forall t \geq 0 \tag{2.1}$$

Thus, it is only necessary to choose one point in the rigid body to describe its position trajectory. Nonetheless, to describe the orientation trajectory, another orthonormal frame $\mathcal{F}_o = (\vec{x_o}, \vec{y_o}, \vec{z_o})$ has to be fixed at the object, for example, in $p(t)$ (fig. 2.1).

2.1.1 Rigid Body Rotation

Rotation Matrix

The object orientation in fig. (2.1) can be described by a rotation matrix, that relates the two orthonormal coordinate frames.

Given the coordinates of the frame $\mathcal{F}_o$ with respect to the $\mathcal{F}_a$ frame in the column vectors $x_o^a, y_o^a, z_o^a \in \mathbb{R}^3$, a rotation matrix from $\mathcal{F}_o$ to $\mathcal{F}_a$ is defined as (Spong *et al.*, 2005):

$$^aR_o = \begin{bmatrix} x_o^a & y_o^a & z_o^a \end{bmatrix} \in \mathbb{R}^{3\times 3} \tag{2.2}$$

And since the right-hand rule is used here, ^aR_o also possesses the following properties:

$$(^aR_o)^\top = (^aR_o)^{-1} \tag{2.3}$$

$$det(^aR_o) = +1 \tag{2.4}$$

As a matter of fact, every 3×3 matrix with the same properties belongs to the 3-dimensional special orthonormal group SO(3) . Moreover, the special orthonormal

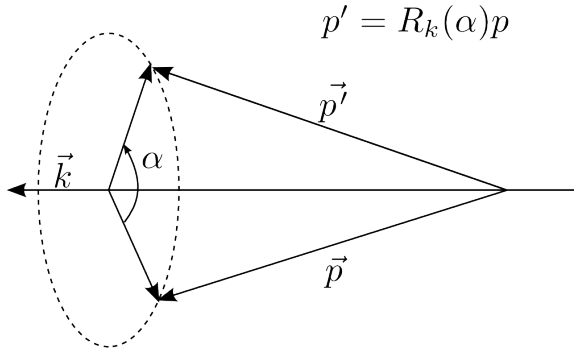

Figure 2.2: Vector $\vec{p}$ rotated by an angle α around an axis $\vec{k}$

group can be generalized for other dimensions:

$$SO(n) = \{R \in \mathbb{R}^{3\times 3} \mid RR^\top = I, det(R) = +1\} \tag{2.5}$$

The rotation of a position vector in $\mathcal{F}_o$ coordinates to $\mathcal{F}_a$ coordinates is:

$$^a p = {}^a R_o \, {}^o p \tag{2.6}$$

One may also concatenate rotation matrices, for example, a rotation matrix from $\mathcal{F}_c$ to $\mathcal{F}_a$ is equivalent to a rotation from $\mathcal{F}_a$ to $\mathcal{F}_b$, then a rotation from $\mathcal{F}_b$ to $\mathcal{F}_c$ (post-multiplication):

$$^a R_c = {}^a R_b \, {}^b R_c \tag{2.7}$$

Axis and Angle

By the Euler theorem (Murray *et al.*, 1994) a rotation matrix $R_k(\alpha) \in SO(3)$ can be interpreted as a rotation operator for a vector $\vec{p}$ around a fixed axis represented by a unit vector with coordinates $k = (k_x, k_y, k_z)^\top \in \mathbb{R}^3$ by an angle $\alpha \in [0, 2\pi)$ (fig. 2.2). Therefore, the rotated vector is:

$$p' = R_k(\alpha)p \tag{2.8}$$

where,

$$R_k(\alpha) = e^{\hat{k}\alpha} \tag{2.9}$$

And,

$$\hat{k} = \begin{bmatrix} 0 & -k_z & k_y \\ k_z & 0 & -k_x \\ -k_y & k_x & 0 \end{bmatrix} \tag{2.10}$$

Finally, we can calculate $e^{\hat{k}\alpha}$ by using the Rodrigues formula (Murray *et al.*, 1994):

$$e^{\hat{k}\alpha} = I + \hat{k}\sin(\alpha) + \hat{k}^2(1 - \cos(\alpha)) \tag{2.11}$$

To complete the equivalence, given R, it is also possible to retrieve $k \in \mathbb{R}^3, \alpha \in \mathbb{R}$:

$$\alpha = \arccos\left(\frac{tr(R)-1}{2}\right) \tag{2.12}$$

$$\hat{k} = \frac{1}{2\sin(\alpha)}(R - R^\top) \tag{2.13}$$

Quaternion

Another very common way to represent a body orientation is to use unit quaternions, which have no singularities, and use less mathematical operations when calculating rotations if compared to rotation matrices (Murray *et al.*, 1994; Siciliano *et al.*, 2008).

Quaternions are a generalization of complex numbers, and a quaternion $\mathcal{Q}$ is given by $\mathcal{Q} = a + bi + cj + dk$, where $a, b, c, d \in \mathbb{R}$, and $i, j, k \in \mathbb{C}$ are unit imaginary numbers. Its scalar component is given by $\mathcal{Q}_s = a$, and its vector component by $\mathcal{Q}_v = [b, c, d]^\top$. Commonly, a quaternion is represented by a 4-dimensional vector space $\mathbb{Q}$ such that:

$$\begin{bmatrix} \mathcal{Q}_s \\ \mathcal{Q}_v \end{bmatrix} = \begin{bmatrix} a \\ b \\ c \\ d \end{bmatrix} \in \mathbb{Q} \tag{2.14}$$

A quaternion multiplication between $\mathcal{Q}_1, \mathcal{Q}_2 \in \mathbb{Q}$, which is distributive and associative, but not commutative is defined as:

$$\mathcal{Q}_1 \cdot \mathcal{Q}_2 = \begin{bmatrix} \mathcal{Q}_{1s}\mathcal{Q}_{2s} - \mathcal{Q}_{1v}^\top \mathcal{Q}_{2v} \\ \mathcal{Q}_{1s}\mathcal{Q}_{2v} + \mathcal{Q}_{2s}\mathcal{Q}_{1v} + \widehat{\mathcal{Q}_{1v}}\mathcal{Q}_{2v} \end{bmatrix} \tag{2.15}$$

The conjugate of a quaternion $\mathcal{Q} = [\mathcal{Q}_s, \mathcal{Q}_v]^\top$ is $\mathcal{Q}^* = [\mathcal{Q}_s, -\mathcal{Q}_v]^\top$ such that:

$$\mathcal{Q} \cdot \mathcal{Q}^* = \begin{bmatrix} 1 \\ 0 \\ 0 \\ 0 \end{bmatrix} \tag{2.16}$$

where $[1, 0, 0, 0]^\top$ is the identity element with respect to quaternion multiplication.

Finally, Murray *et al.* (1994) defines *unit quaternions* as a subset of all $\mathcal{Q} \in \mathbb{Q}$ such that $\|\mathcal{Q}\|^2 = a^2 + b^2 + c^2 + d^2 = 1$. Moreover, the rotation of θ rad around an axis $\vec{k}$ is associated with the following unit quaternion:

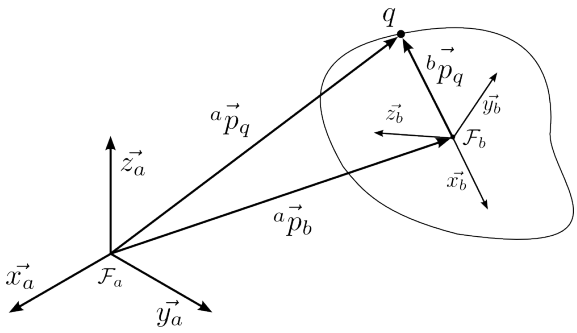

Figure 2.3: Coordinate transformation from orthonormal frame $\mathcal{F}_b$ to orthonormal frame $\mathcal{F}_a$

$$\mathcal{Q} = \begin{bmatrix} \cos\left(\frac{\theta}{2}\right) \\ k\sin\left(\frac{\theta}{2}\right) \end{bmatrix} \tag{2.17}$$

And the associated rotation matrix $R_k(\theta)$ is:

$$R_k(\theta) = (2\mathcal{Q}_s^2 - 1)I + 2(\mathcal{Q}_v\mathcal{Q}_v^\top + \mathcal{Q}_s\widehat{\mathcal{Q}}_v) \tag{2.18}$$

The unit quaternions are a group that gives a global parameterization for the group $SO(3)$.

2.1.2 Homogeneous Transformation Matrix

A position $^ap_b \in \mathbb{R}^3$, and orientation $^aR_b \in SO(3)$ with respect to an inertial frame $\mathcal{F}_a$ fully describes free motion of a rigid body in space. The rigid body configuration space is then the product space of $\mathbb{R}^3$ and $SO(3)$, denominated 3-dimensional special euclidean group (SE(3)) :

$$SE(3) = \{(p, R) \mid p \in \mathbb{R}^3, R \in SO(3)\} = \mathbb{R}^3 \times SO(3) \tag{2.19}$$

Which also generalizes to n dimensions:

$$SE(n) = \mathbb{R}^3 \times SO(3) \tag{2.20}$$

If desired to transform the coordinates of a point q from $\mathcal{F}_b$ to the $\mathcal{F}_a$ frame, that is, obtain ^ap_q from ^bp_q, then the pair $(^ap_b, ^aR_b)$ is used (fig. 2.3):

$$^ap_q = {}^ap_b + {}^aR_b{}^bp_q \tag{2.21}$$

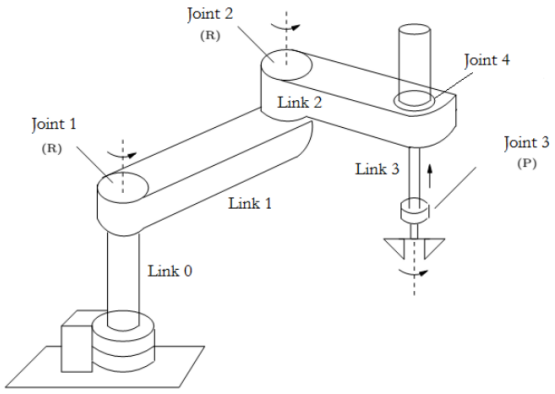

Figure 2.4: Robot manipulator with revolution and prismatic joints (Leite, 2005)

Which can be rewritten in matrix form as:

$$\begin{bmatrix} {}^{a}p_q \\ 1 \end{bmatrix} = \begin{bmatrix} {}^{a}R_b & {}^{a}p_b \\ 0 & 1 \end{bmatrix} \begin{bmatrix} {}^{b}p_q \\ 1 \end{bmatrix} \tag{2.22}$$

where we define a homogeneous transformation matrix as:

$${}^{a}T_b = \begin{bmatrix} {}^{a}R_b & {}^{a}p_b \\ 0 & 1 \end{bmatrix} \tag{2.23}$$

Note that differently from the rotation matrix, with homogeneous transformations we have that $({}^{a}T_b)^{\top} \neq {}^{b}T_a$. Moreover, the inverse transformation is given by:

$${}^{b}T_a = \begin{bmatrix} {}^{b}R_a & -{}^{b}R_a\,{}^{b}p_a \\ 0 & 1 \end{bmatrix} \tag{2.24}$$

Nonetheless, it is also possible to concatenate homogeneous transformations:

$${}^{a}T_c = {}^{a}T_b\,{}^{b}T_c \tag{2.25}$$

2.2 Forward Kinematics

The goal of the forward kinematics is to calculate the pose of the EEF with respect to a base frame based on the configuration of the robot joints.

An open chain robotic manipulator has $n+1$ links, and n joints, in which a frame is placed at the end of every link from the first link (link 0, usually fixed to the base) until the last link (link n, where the EEF is fixed) (fig. 2.4).

The pose of each posterior frame with respect to the anterior frame is given by a homogeneous transformation ${}^{i-1}T_i(q_i)$ that is dependable on a joint variable

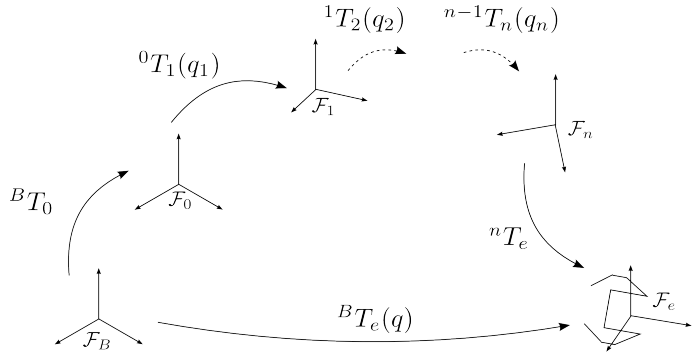

Figure 2.5: Forward kinematics in an open-chain manipulator

$q_i \in \mathbb{R} \mid i \in \mathbb{N}$ and $i \in [0, n]$.

The transformation from link 0 to link n is obtained by concatenating transformations (fig. 2.5):

$$ {}^{0}T_n(q) = {}^{0}T_1(q_1){}^{1}T_2(q_2)\dots{}^{i-1}T_i(q_i)\dots{}^{n-1}T_n(q_n) \tag{2.26} $$

where the variable $q \in \mathbb{R}^n$ is formed by stacking up the q_i variables. Moreover, q forms the joint configuration space of the robot.

Finally, to obtain the forward kinematics homogeneous transformation matrix, one has to concatenate two additional transformations, one from the base to the link 0, and another from link n to the EEF:

$$ {}^{B}T_e(q) = {}^{B}T_0\,{}^{0}T_n(q)\,{}^{n}T_e \tag{2.27} $$

A robot forward kinematics is usually expressed as an equation of the form:

$$ x_e(q) = f(q) = \begin{bmatrix} p_e \\ \phi_e \end{bmatrix} \tag{2.28} $$

where p_e is the EEF position taken from eq. (2.27), and ϕ_e is a representation of the EEF orientation, possibly an unit quaternion $\mathcal{Q}_e \in \mathbb{Q}$ like in eq. 2.17.

Remark. *From now on, unless stated otherwise, it is assumed that any coordinates are taken with respect to a base frame $\mathcal{F}_B$.*

Since a task trajectory requirements for the EEF are usually described in position and orientation representations, $x_e(q) \in SE(\cdot)$ denotes the task operational (or cartesian) space, while $q \in \mathbb{R}^n$ denotes the task joint (or configuration) space.

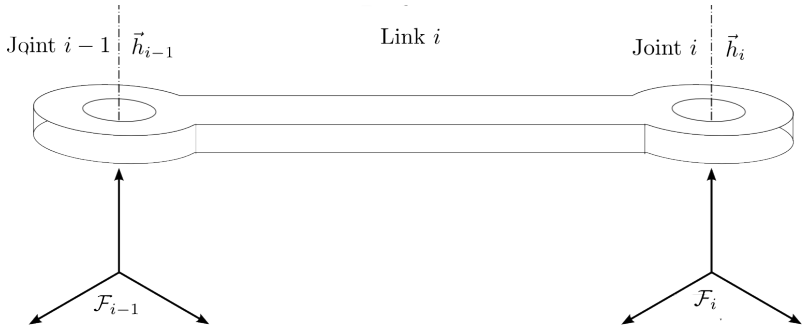

Figure 2.6: Placement of joint i axis for the Jacobian calculation

2.3 Differential Kinematics

The goal of differential kinematics is to find a relationship between the joint velocities ($\dot{q}$) and the EEF velocity (linear, $\dot{p}_e(q)$, and angular, ω_e):

$$v_e = \begin{bmatrix} \dot{p}_e \\ \omega_e \end{bmatrix} = \begin{bmatrix} J_p(q) \\ J_o(q) \end{bmatrix} \dot{q} = J(q)\dot{q} \tag{2.29}$$

where $J_p(q) \in \mathbb{R}^{3\times n}$ is the position Jacobian, and $J_o(q) \in \mathbb{R}^{3\times n}$ is the orientation Jacobian, when stacked together they form the geometric Jacobian $J(q) \in \mathbb{R}^{6\times n}$.

2.3.1 Jacobian Calculation

Every column i of the Jacobian matrix corresponds to one joint i of the manipulator.

$$J_n(q) = \begin{bmatrix} J_{p1} & \dots & J_{pn} \\ J_{o1} & \dots & J_{on} \end{bmatrix} \tag{2.30}$$

Given a unit vector $\vec{h}_i$ correspondent to the joint i axis (fig. 2.6), the link i velocities at frame $\mathcal{F}_{i-1}$ are related to $\dot{q}_i$ by:

$$\begin{bmatrix} {}^{i-1}\vec{v}_i \\ {}^{i-1}\omega_i \end{bmatrix} = \begin{cases} \begin{bmatrix} 0 \\ \vec{h}_i \end{bmatrix} \dot{q}_i, & i \text{ is revolute} \\ \\ \begin{bmatrix} \vec{h}_i \\ 0 \end{bmatrix} \dot{q}_i, & i \text{ is prismatic} \end{cases} \tag{2.31}$$

Then, the velocities at the frame $\mathcal{F}_n$ are taken using the adjoint transformation Murray *et al.* (1994):

$$\begin{bmatrix} {}^{n}\vec{v}_i \\ {}^{n}\omega_i \end{bmatrix} = \begin{bmatrix} \mathcal{I} & -{}^{i}\vec{p}_n\times \\ 0 & \mathcal{I} \end{bmatrix} \begin{bmatrix} {}^{i-1}\vec{v}_i \\ {}^{i-1}\omega_i \end{bmatrix} \tag{2.32}$$

where ${}^{i}\vec{p}_n$ is the position vector from frame $\mathcal{F}_n$ with respect to the frame $\mathcal{F}_i$.

Depending on the joint type we have:

$$\begin{bmatrix} J_{pi} \\ J_{oi} \end{bmatrix} = \begin{bmatrix} {}^{n}\vec{v}_i \\ {}^{n}\omega_i \end{bmatrix} = \begin{cases} \begin{bmatrix} \vec{h}_i \times {}^{i}\vec{p}_n \\ \vec{h}_i \end{bmatrix} \dot{q}_i, & i \text{ is revolute} \\ \\ \begin{bmatrix} \vec{h}_i \\ 0 \end{bmatrix} \dot{q}_i, & i \text{ is prismatic} \end{cases} \tag{2.33}$$

If the EEF is exactly at the frame $\mathcal{F}_n$, then $J_n(q) = J(q)$, otherwise, the Jacobian at the EEF is given by:

$$J(q) = \begin{bmatrix} \mathcal{I} & -{}^{e}\vec{p}_n\times \\ 0 & \mathcal{I} \end{bmatrix} J_n(q) \tag{2.34}$$

Remark. *J(q) must be expressed in any given frame coordinates before being used in an equation like eq. 2.29.*

If we want to use the operational space along with the orientation representation (eq. 2.28), we should find the representation Jacobian $J_r(\phi)$ that relates $\dot{\phi}$ with ω:

$$\dot{\phi} = J_r(\phi)\omega \tag{2.35}$$

Therefore,

$$\dot{x}_e(q) = \begin{bmatrix} \dot{p}_e \\ \dot{\phi}_e \end{bmatrix} = \begin{bmatrix} I & 0 \\ 0 & J_r(\phi) \end{bmatrix} J(q)\dot{q} = J_a(q)\dot{q} \tag{2.36}$$

where $J_a(q)$ is denoted analytic Jacobian. Moreover, one should note that if the task space does not require orientation, only translational movements, then the analytical Jacobian and the geometric Jacobian is the same ($J_a(q) = J(q)$).

2.3.2 Manipulator Redundancy

The Jacobian is a linear mapping from the joint velocity space ($\dot{q} \in \mathbb{R}^n$), into the EEF velocity space ($\dot{x}_e \in \mathbb{R}^m$).

If $m < n$ then the manipulator is kinematically redundant with respect to the given task, and there are $n - m$ redundant DoF .

Moreover,

$$dim(\mathcal{N}(J(q))) = n - m \neq 0 \iff \mathcal{N}(J(q)) \neq 0 \tag{2.37}$$

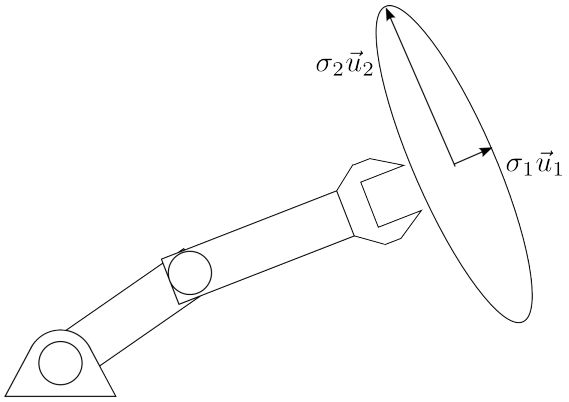

Figure 2.7: Velocity manipulability ellipsoid for a two-link manipulator in a planar task (non-redundant)

Many control algorithms use the Jacobian inverse to map joint velocities from velocities at the operational space. However, in the case of redundant manipulators, the null space of the Jacobian is no longer zero (eq. 2.37), therefore, the Jacobian is not invertible anymore. The solution to this problem is to use the pseudo-inverse matrix $J^\dagger$ instead of the inverse of J:

$$J^\dagger = J^\top (JJ^\top)^{-1} \tag{2.38}$$

$$JJ^\dagger = I \in \mathbb{R}^{m \times m} \tag{2.39}$$

2.3.3 Velocity Manipulability

If $J(q_s) \in \mathcal{N}(J(q))$, then q_s is a *singular configuration* of the manipulator that leads to a $\dot{x}_e = 0$, which implies that singular configurations should be avoided when controlling a robot. As a matter of fact, near a singular configuration, the robot may require high joint velocity rates to move the EEF pose in certain directions.

The *velocity manipulability* serves as an index that measures the ability of the robot to move freely in all directions in the robot workspace.

Infinitesimal EEF pose motion is related to infinitesimal joint motion through the Jacobian matrix (eq. 2.29), for that reason the Jacobian is usually the base for *local manipulability* measures (ability to change its pose at a given configuration). There are many different ways to define a manipulability measure, but they are usually related to the velocity manipulability ellipsoid.

The set of joint velocities of constant (unit) norm is given by:

$$\dot{q}^\top \dot{q} = 1 \tag{2.40}$$

It describes the points on the surface of a sphere in the joint velocity space,

which for a redundant manipulator, where $\dot{q} = J^{\dagger}(q)\dot{x}_e$, translates to:

$$\dot{x}_e^{\top} \left(J(q)^{\dagger\top} J^{\dagger}(q) \right) \dot{x}_e = 1 \tag{2.41}$$

That yields,

$$\dot{x}_e^{\top} \left(J(q) J^{\top}(q) \right)^{-1} \dot{x}_e = 1 \tag{2.42}$$

Which is a quadratic expression equivalent to the equation of an ellipsoid surface in the EEF velocity space. Along the direction of the major axis of the ellipsoid the EEF move at a larger velocity easier than along the direction of the minor axis of the ellipsoid (fig. 2.7). Note that the closer the ellipsoid is to a sphere, the better the robot is able to move in all directions.

The ellipsoid axes can be calculated by obtaining the eigenvectors of $JJ^{\top}$: $\vec{u}_1, \ldots, \vec{u}_m$. And the dimensions of the axes are given by the singular values from J that can be obtained from singular value decomposition: $\sigma_1, \ldots, \sigma_m$ (Siciliano *et al.*, 2008).

Finally, some examples of manipulability measure include (Murray *et al.*, 1994):

- Minimum singular value of J:

$$w_1(q) = \sigma_{min}(J(q)) \tag{2.43}$$

  Which corresponds to the minimum velocity in the operational space that can be produced by a unit joint velocity vector.

- Inverse of the condition number of J:

$$w_2(q) = \frac{\sigma_{min}(J)}{\sigma_{max}(J)} \tag{2.44}$$

- Velocity ellipsoid volume (Yoshikawa, 1985):

$$w_3(q) = \sqrt{\det\left(JJ^{\top}\right)} = \sigma_1 \ldots \sigma_m \tag{2.45}$$

  This measure gives a more global measure of velocity manipulabity, however, it may produce significant values of manipulability if a singular value of J is very large in one direction, and another singular value is very small in another direction.

Note that all those measures produce 0 manipulability levels at a singular configuration q_s, therefore, they are usually interpreted as a measure of distance from a given configuration q to a singular configuration q_s.

2.4 Kinematic Control

Slow movement of robotic manipulators with high performance joint speed control, and high gear ratios, can be controlled without considering the effects of its intrinsic dynamics (inertia matrix, coriolis matrix, and gravity).

The EEF movement in time is given by eq. 2.36. The kinematic control problem consists in designing a $\dot{q}(t) \in \mathbb{R}^n$ that takes the EEF pose trajectory $x_e(t)$ to a reference pose trajectory $x_{ref}(t)$, that is, take a tracking error $e(t)$ to zero:

$$e(t) = \begin{bmatrix} e_p(t) \\ e_o(t) \end{bmatrix} \tag{2.46}$$

$$\lim_{t\to\infty} e(t) = 0 \leftrightarrow \lim_{t\to\infty} x_e(t) = x_{ref}(t) \tag{2.47}$$

Where e_p, e_o are the position and orientation errors respectively.

2.4.1 Position Control

In the case of position control $e(t) = e_p(t) = x_e(t) - x_{ref}(t)$. Then, deriving e to get the error dynamics:

$$\dot{e} = J(q)\dot{q} - \dot{x}_{ref} \tag{2.48}$$

If $J \in \mathbb{R}^{n\times n}$, and J is invertible, then we can linearize the system designing $\dot{q}$ with J^{-1} and a control signal $u \in \mathbb{R}^n$ as:

$$\dot{q} = J^{-1}u \tag{2.49}$$

$$\dot{e} = u - \dot{x}_{ref} \tag{2.50}$$

Then, assuming $\dot{x}_{ref}$ is available, it is used as a feedforward term along with a feedback term to design u:

$$u = -K_p(x_e - x_{ref}) + \dot{x}_{ref} \tag{2.51}$$

That leads to the system:

$$\dot{e} + K_p e = 0 \tag{2.52}$$

Which is exponentially stable if $K_p > 0$.

2.4.2 Position Control with Redundant Manipulators

If a manipulator is redundant to its required task ($m < n$, and $J \in \mathbb{R}^{m \times n}$), its Jacobian matrix is longer be invertible, therefore, eq. 2.49 is not available as an option for kinematic control anymore.

So, instead of using the inverse of J, we use its pseudo-inverse matrix $J^{\dagger}$ in eq. 2.49 so we have:

$$\dot{q} = J^{\dagger}(\dot{x}_{ref} - K_p e) \tag{2.53}$$

Which leads to the same error system as in eq. 2.52.

Exploring Redundancies

Because of its null space a redundant manipulator has an infinite number of solutions $\dot{q}$ that satisfy eq. 2.36. In other words, given an EEF velocity, there are an infinite number of velocity configurations that are able to achieve it (due to internal motions).

Notwithstanding, it is possible to use that knowledge to try to obtain different secondary goals, by using a matrix whose range is in the null space of $J(q)$ (Siciliano *et al.*, 2008):

$$\mathcal{R}(I - J^{\dagger}J) \in \mathcal{N}(J) \tag{2.54}$$

And applying it into the kinematic control law for redundant manipulators (eq. 2.53):

$$\dot{q} = J^{\dagger}(\dot{x}_{ref} - K_p e) + (I - J^{\dagger}J)\nu \tag{2.55}$$

where ν is usually assigned the secondary goal of maximizing a function $w(q)$:

$$\nu = K_0 \left(\frac{\partial w(q)}{\partial q}\right)^{\top} \tag{2.56}$$

Common secondary goals are given by functions that describe desired behavior that is not essential to the task completion, like maximizing the distance to obstacles, or trying to guarantee maximum distance from singular configurations while executing a movement by using the task manipulability (eq. 2.45).

2.4.3 Position and Orientation Control with Quaternions

To be able to control an EEF orientation, first, a definition for error orientation is needed. In the case of a unit quaternion representation we can compare orientations by the following error quaternion:

$$\mathcal{Q}_{error} = \mathcal{Q}_e(t) \cdot \mathcal{Q}^*_{ref}(t) = \begin{bmatrix} \mathcal{Q}_{es} \\ \mathcal{Q}_{ev} \end{bmatrix} \tag{2.57}$$

If the desired orientation $\mathcal{Q}_{ref}$ is the current orientation $\mathcal{Q}_e$ we have $\mathcal{Q}_{es} = 1$, and $\mathcal{Q}_{ev} = [0, 0, 0]^\top$. Then, since $\mathcal{Q}_{e0} = 1 \leftrightarrow \mathcal{Q}_{ev} = \vec{0}$, we define an orientation error for a quaternion representation by only using $\mathcal{Q}_{ev}$:

$$e_o(t) = \mathcal{Q}_{ev} \tag{2.58}$$

Now, similarly to the position control scenario we may propose a linearizing control law for the EEF entire pose:

$$\dot{q} = J^\dagger \left(\begin{bmatrix} -K_p & 0 \\ 0 & -K_o \end{bmatrix} \begin{bmatrix} e_p(t) \\ e_o(t) \end{bmatrix} + \begin{bmatrix} \dot{p}_{ref} \\ 0 \end{bmatrix} \right) \tag{2.59}$$

Notwithstanding, eq. 2.59 is known to make the equilibrium point $e(t) = 0$ almost globally asymptotically stable (Slotine and Li, 1991; Wen and Kreutz-Delgado, 1991).

2.5 Dynamic Equation of Motion

A dynamic model for a manipulator with n DoF ($q \in \mathbb{R}^n$) in its joint space may be given by the following EoM[1](Murray *et al.*, 1995):

$$M(q)\ddot{q} + C(q, \dot{q})\dot{q} + g(q) = \tau_c - J^\top(q)F_{ext} \tag{2.60}$$

where $M(q) \in \mathbb{R}^{n \times n}$ is the inertia matrix; $C(q, \dot{q}) \in \mathbb{R}^{n \times n}$ is the Coriolis matrix; $g(q) \in \mathbb{R}^n$ is a vector with gravitational torques for each joint; $J(q) \in \mathbb{R}^{3 \times n}$ is the manipulator Jacobian; $F_{ext} \in \mathbb{R}^{3 \times 1}$ is the equivalent external force vector applied to the EEF); and $\tau_c \in \mathbb{R}^n$ is a control vector used to achieve a desired dynamic behavior for the manipulator.

It is also useful to realize the manipulator dynamics in the operational space referred in subsection 2.2. Thus, the EoM turns into:

$$\Lambda(q)\ddot{x}_e + \mu(q, \dot{q})\dot{x}_e + F_g(q) = F_c + F_{ext} \tag{2.61}$$

[1]In this work, only external forces (without external torques) are considered to the dynamic equation of motion.

$$\Lambda = (JM^{-1}J^{\top})^{-1} \tag{2.62}$$

$$\mu\dot{x}_e = \Lambda(JM^{-1}C - \dot{J})\dot{q} \tag{2.63}$$

$$F_g = \left(J^{\top}\right)^{\dagger} g \tag{2.64}$$

$$F_c = \left(J^{\top}\right)^{\dagger} \tau_c \tag{2.65}$$

where $\Lambda(q) \in \mathbb{R}^{3\times3}$ is the EEF inertia matrix, also referred as apparent inertia, (Ficuciello *et al.*, 2014), $\mu\dot{x}_e$ represents the forces at the EEF correspondent to the Coriolis matrix in joint space, and F_g and F_c to the forces at the EEF correspondent to the gravitational, and control torques.

2.6 Impedance and Admittance Control

A mechanical impedance (or admittance) is a relationship between a body motion and the effort applied to it. It can be seen both in the joint space, with angular displacements and external torques, and in the operational space, with displacements and external forces.

If the system receives effort as input, and outputs motion it behaves as a mechanical admittance. On the other hand, if the input is motion and the output is effort then it behaves as an impedance.

It is possible to specify this relationship in terms of a *mass-spring-damper* system. In the operational space for instance, the impedance/admittance at the EEF level is modeled as the following differential equation:

$$\Lambda_d\ddot{e}_r + D_d\dot{e}_r + K_d e_r = F_{ext} \tag{2.66}$$

$$e_r(t) := x_e(t) - x_r(t) \tag{2.67}$$

where $\Lambda_d \in \mathbb{R}^{3\times3}$ is the desired apparent inertia; $D_d \in \mathbb{R}^{3\times3}$ is the desired damping; and $K_d \in \mathbb{R}^{3\times3}$ is the desired stiffness. Furthermore, Λ_d, D_d and K_d are all positive definite and symmetric.

The system in eq. (2.66) has its equilibrium point defined by a robot desired trajectory ($x_r(t)$, $\dot{x}_r(t)$, $\ddot{x}_r(t)$), and it receives a position/velocity feedback, or a force feedback, which depends on the controller, either an impedance controller, or an admittance controller.

Both controllers, the impedance controller and the admittance controller, feature advantages and disadvantages depending on the environment stiffness, and the available robot. Further readings regarding the admittance/impedance duality can be found in Ott *et al.* (2010); Siciliano *et al.* (2008).

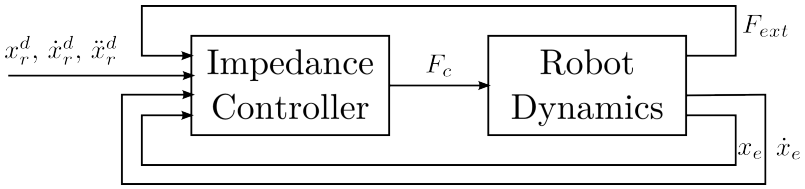

Figure 2.8: Impedance Control Implementation

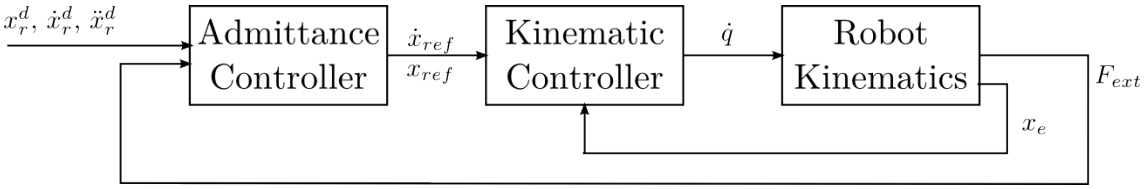

Figure 2.9: Admittance Control Implementation

2.6.1 Impedance Controller

In impedance control (fig. 2.8), the system (eq. 2.61) is linearized by force control (Siciliano *et al.*, 2008):

$$F_c = \Lambda u_c + \mu \dot{x}_e + F_g - F_{ext} \tag{2.68}$$

Substituting eq. 2.68 into eq. 2.61 we have:

$$\ddot{x}_e = u_c \tag{2.69}$$

And inspecting eq. 2.66 we choose the input control, u_c, as:

$$u_c = \ddot{x}_r + \Lambda_d^{-1}(-D_d \dot{e}_r - K_d e_r + F_{ext}) \tag{2.70}$$

2.6.2 Admittance Controller

Very compliant environments associated with a low K_d may degrade the rejection of disturbances using impedance control (Siciliano *et al.*, 2008) (fig. 2.8), to solve this issue, admittance control separates the kinematic control problem from the impedance control problem, in such a way that the kinematic controller is designed as to guarantee the disturbances rejection. Therefore, there are two separate controllers (fig. 2.9): an outer loop controller (the admittance controller) that specifies a reference velocity, or position, $\dot{x}_{ref}$ or x_{ref}, given the external forces vector (F_{ext}); and an inner loop kinematic controller that receives x_{ref}, or $\dot{x}_{ref}$ and outputs joint velocities commands.

Both controllers are separately designed. The velocity control may be designed as in (2.53), while the admittance controller is implemented substituting e_r by $(x_{ref} - x_r)$ in (2.66) (Siciliano *et al.*, 2008), *i.e.*:

$$\Lambda_d \left(\ddot{x}_{ref} - \ddot{x}_r\right) + D_d \left(\dot{x}_{ref} - \dot{x}_r\right) + K_d(t) \left(x_{ref} - x_r\right) = F_h(t) \tag{2.71}$$

2.7 Conclusions

The fundamental concepts presented in this chapter may be used not only to model, analyze and control open-chain serial robots, but also to model a human arm as a robot with 7 degrees of freedom, allowing an unified analysis of performance for both the human arm and the robot arm.

However, in the case of the human arm, some informations, like torque applied at every joint or intention of movement are likely not readily available in real application scenarios. To settle some of these issues, one approach used by many researchers is to use biological signals such as EMG.

Chapter 3

Electromyography and Co-Contraction

This chapter describes the nature of the EMG signal, and overviews some of its applications. It provides guidelines to the signal acquisition, and processing. Furthermore, it points out common pitfalls regarding the usage of EMG signal and its acquisition.

It ends by discussing human arm stiffness, the concept of co-contraction, how to obtain an index of co-contraction (ICC), and how those concepts are related.

3.1 Electromyography

Electromyography is an experimental technique concerned with the development, recording, and analysis of myoelectric signals, which are formed by physiological variations in the state of muscle fiber membranes (Basmajian and De Luca, 1985).

The muscle fiber membranes are part of the motor unit (MU). A MU is the smallest functional unit of a muscle. It comprises a α-motoneuron, its axon, and a set of muscle fibers attached to it. Whenever a MU is activated by an action potential (electrical signal from the central nervous system), its muscle fibers will contract. The activation of several MUs will contract several groups of muscle fibers and will result in the muscle contraction. These activations superpose themselves and may be detected by surface EMG sensors placed on the human skin (fig. 3.1). Properly placed surface EMG sensors are able to roughly detect the EMG signal of a single muscle. If the muscle that is desired for the EMG signal acquisition is located internally in a human limb then needles and wire electrodes will be used instead of skin surface electrodes. Those types of sensors require very specialized training and a special room/laboratory for an experiment. Therefore, all EMG sensors used in this work are the simpler surface electrodes.

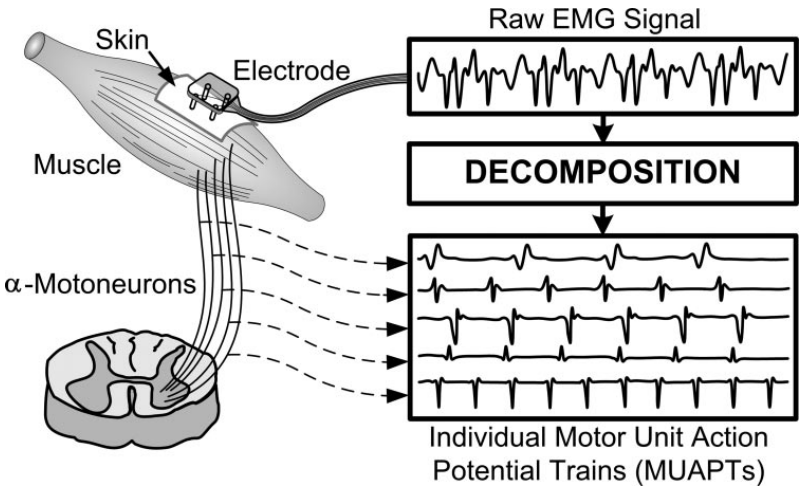

Figure 3.1: A surface EMG signal composed of several motor unit action potentials (Luca *et al.*, 2006)

3.1.1 Applications

The EMG signal may be used to estimate or measure data from individual muscles, or sets of muscles. It is possible to estimate torque/force in isometric contractions; estimate the muscle activation; indicate fatigue in a muscle; or compare the behavior of different sets of muscles in different experiment trials for different human subjects.

EMG signal is used in real world applications in the most diverse areas of knowledge, such as medical research; rehabilitation; ergonomics; sports science; or in HRC. EMG signal provides information regarding intention of motion, which could be voluntary or not. Due to communication delay, the EMG signal shows activity before the muscle actually starts contracting (Luca, 2008). In this work, EMG signal is used to quantify muscle activation levels.

3.1.2 EMG Acquisition Pitfalls

The acquisition of EMG signal and its interpretation, however, can be dramatically influenced by several factors, of which the most prominent are:

- Cross-talk from other muscles (fig. 3.2a);
- Sensor location (fig. 3.2b);
- Sensor quality;
- Changes in muscle geometry during signal acquisition (fig. 3.2c)
- Sensor not properly attached to the skin;
- Electrode-Skin high impedance;

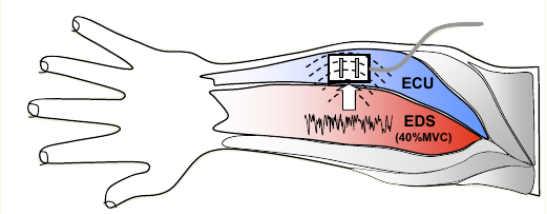

(a) The conductivity of the skin and other human tissues generate cross talk even when the sensor is perfectly placed on top of the desired muscle at all times (Luca, 2008)

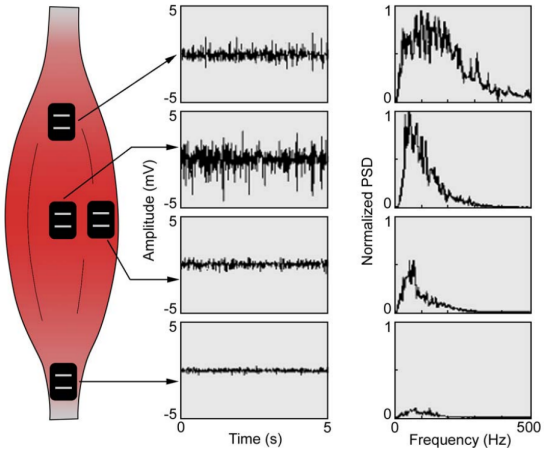

(b) The sensor location greatly influences both the amplitude and the frequency of the EMG signal (Luca, 1997)

(c) When the biceps contracts, the muscle moves away of the EMG sensor in this figure (Konrad, 2005)

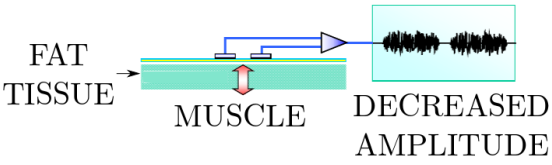

(d) Some human tissues, such as subcutaneous fat, with high impedance will alter the EMG signal (Konrad, 2005)

Figure 3.2: Difficulties that arise when acquiring EMG signal

- High impedance of other human tissues (fig. 3.2d);

The crosstalk is caused by the inherent conductivity of the human skin and other tissues, thus, making it possible for other muscles' signals to interfere in the signal from the desired muscle.

As can be seen on fig. 3.2b, both the amplitude and frequency of a muscle EMG signal greatly vary according to the sensor location relative to the desired muscle. Higher signal amplitudes are to be found with sensors placed on the muscle belly. This also implies that, whenever a muscle changes its geometry while contracting, the EMG sensor may not be in ideal condition for signal acquisition anymore (fig. 3.2c).

Another sensitive aspect consists of the human skin impedance, that may be too high mostly due to dirt, dead cells, etc. To decrease the skin-electrode impedance, the skin is usually cleaned prior to the signal acquisition. Furthermore, other tissues may decrease the signal quality, like subcutaneous fat tissue with high impedance values (fig. 3.2d).

3.1.3 Guidelines to EMG acquisition

General guidelines for EMG acquisition can be found in the books/website by the former European project SENIAM (Surface ElectroMyoGraphy for the Non-Invasive Assessment of Muscles) (Stegeman and Hermens, 2007) (`www.seniam.org`), or in (Luca, 2008). The guidelines can be summarized as:

- Use differential sensors (with two electrodes and one differential amplifier) to reduce noise;
- Place the EMG sensor in the muscle belly, with the electrodes in parallel to the muscle fibers;
  - Perroto (2011) is a good reference for locating muscles, and ideal sensor placement;
- Clean the human subject skin with gaze and alcohol (and allow the alcohol to vaporize) to decrease the skin impedance;
- Use good adhesive to attach the EMG sensor onto the skin;

3.1.4 EMG signal processing

Raw EMG signal

The unfiltered and unprocessed superposition of MU action potentials is called a *raw EMG signal* (u_{raw}). Considering that the signal acquisition is being properly done, and the noise sources have been taken care of, whenever a muscle is completely relaxed its baseline should have very little noise, and when it contracts its amplitude spikes are of random nature (Konrad, 2005)(fig. 3.3).

The raw EMG signal typically is in the scale of μV and its frequency ranges up to 500 Hz (Luca, 1997). Some EMG sensors have built-in band pass filters to avoid anti-aliasing effects while sampling. According to the Nyquist sampling theorem, the minimum sampling rate has to be of 1 kHz.

Signal Processing Overview

Due to the random nature of the EMG signal amplitude spikes, the use of the raw EMG signal directly into robot control loops or even in off-line analyses would not be advantageous since it would produce very unreliable data. To overcome this issue, the EMG signal must be properly processed. Lots of works in the literature that use EMG signal to quantify mucle activation levels process it in similar fashion (Ahmadi-Pajouh *et al.*, 2012; Darainy and Ostry, 2008; Grafakos *et al.*, 2016; Luca, 1997; Paul L. Gribble and Mattar, 2003):

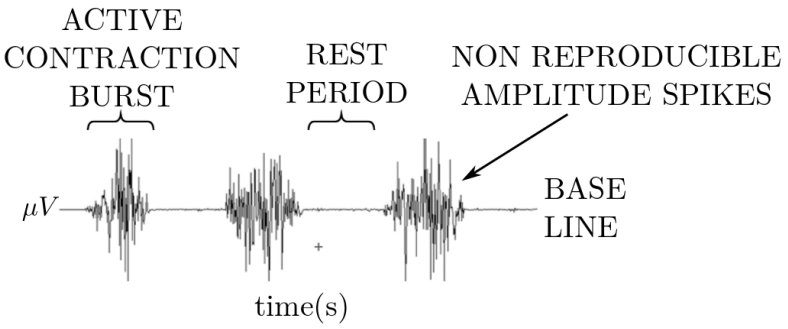

Figure 3.3: Raw EMG signal example (Konrad, 2005)

- Obtain the EMG signal envelope;
  - Apply full-wave signal rectification followed by a low-pass filter;
  - Or apply a windowed RMS filter;
- Normalize the muscle EMG signal with respect to a maximum voluntary contraction signal (MVC);

Obtaining the signal envelope will smooth as well as remove the negative values of the signal. While the signal normalization will actually calculate a measure of muscle activation that may be compared with other experiment trials, even from other subjects.

To illustrate the signal processing, the steps taken in this work to process the EMG signal are shown in the next section.

EMG Signal Envelope

To obtain an envelope of the signal, in this work, the raw EMG signal (u_{raw}) is passed through a windowed RMS filter with a 100 ms time window which is suitable for most cases (Konrad, 2005). Then, to further smooth the signal, an additional low pass third order Butterworth filter with a cut-off frequency of 10 Hz is applied to it. A summary of the steps taken toward the enveloping of the EMG signal can be seen on the fig. 3.4.

Signal Normalization

The value to which the EMG signal is normalized has to be obtained from an isometric exercise (contraction without limb movement) related to the muscle that will be measured *a posteriori*. The subject usually executes 3 isometric contractions with 1 min rest intervals to avoid muscle fatigue (Luca, 2008), then the highest value is assigned as the MVC for that muscle. The normalized EMG (u^i_{norm}) for a certain

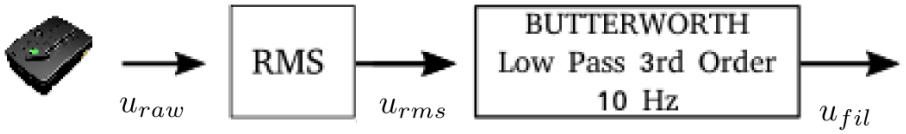

(a) EMG signal processing steps: acquisition from sensor u_{raw}; RMS window of 100 ms (u_{rms}); Butterworth low pass third order filter with 10 Hz cutoff frequency(u_{fil}).

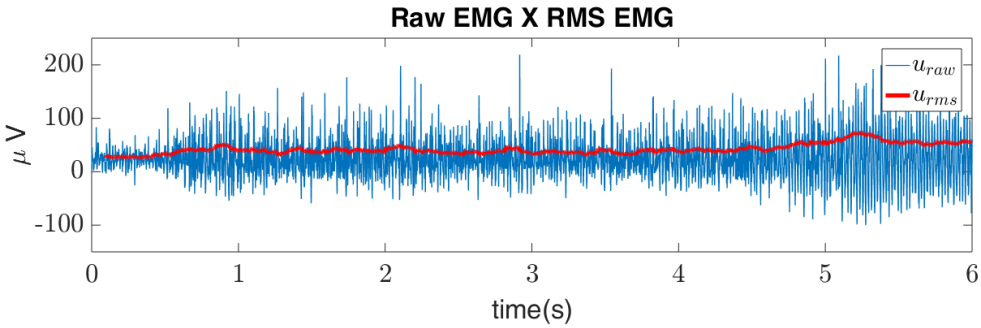

(b) Comparison between u_{raw}, and u_{rms}. It can be seen that u_{rms} is an envelope of u_{raw}.

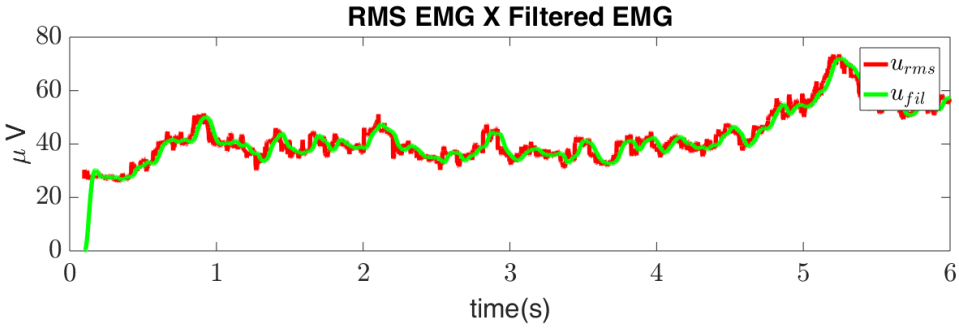

(c) Comparison between u_{rms}, and u_{fil}. The Butterworth filter smooths the RMS signal.

Figure 3.4: Steps to obtain an enveloped EMG signal for this work

muscle i will be given by the ratio between the filtered signal(u^i_{fil}) and the muscle MVC:

$$u^i_{norm}(t) = \frac{u^i_{fil}(t)}{MVC^i} \tag{3.1}$$

3.2 Human Arm Stiffness and Co-Contraction

There are 3 types of stiffness associated with a human arm:

- Muscle stiffness: The resistance of a single muscle to arm displacement;
- Joint stiffness: The resistance of a joint to changes in the joint angle;
- Endpoint stiffness: The resistance of the entire arm to endpoint displacements;

The direct measurement of a human arm stiffness in typical conditions (with very few motion restrictions) is either very difficult or unfeasible. This happens because even though it is possible to measure the force/torque in any given time, the neutral point of displacement is moving as well (Gallagher *et al.*, 2014). Nonetheless, the simultaneous contraction of pairs of antagonist muscles, or *co-contraction*, is related to changes in human joint stiffness (Hogan, 1984; M. Smith, 1981), where antagonist muscle pairs are simply muscles that when contracted produce torque around the same joint, but in opposite directions. This happens because the co-contraction leads to an increase in muscle effort and stiffness without the arm displacement, therefore, increasing joint stiffness for several different joints (and endpoint stiffness). Many studies have already verified experimentally the relationship between co-contraction and human joint stiffness (De Serres and Milner, 1991; Gardner-Morse and Stokes, 2001; Nielsen *et al.*, 1994).

It is important to note that the endpoint stiffness depends not only on the joint stiffnesses, but also on the human arm configuration (posture) (Murray *et al.*, 1995). Therefore, achieving arbitrary endpoint stiffness at arbitrary positions is not feasible (Ajoudani *et al.*, 2017a; McIntyre *et al.*, 1996; Perreault *et al.*, 2002). Furthermore, other studies have verified that humans naturally and simultaneously modulate their arm joint stiffnesses and posture to execute movements while optimizing for secondary objectives such as precision, speed, or stabilization of unstable environment dynamics (Burdet *et al.*, 2001; Paul L. Gribble and Mattar, 2003). In addition, in Bó and Poignet (2010); Bó *et al.* (2009), the authors have used Functional Electrical Stimulation (FES) to co-contract the human wrist joint and attenuate pathological tremors.

3.2.1 Index of Co-Contraction

A common way for quantifying co-contraction is to compare the levels of activation (obtained from normalized EMG signals) from a pair of antagonist muscles, and then use the minimum value of both. This is equivalent to obtaining the amount of activation that is responsible for the change in stiffness since the surplus of activation is responsible for the joint movement. This can be summarized by the equation introduced by Thoroughman and Shadmehr (1999) and also used in Gallagher *et al.* (2014); Grafakos *et al.* (2016); Paul L. Gribble and Mattar (2003), where the ICC of a joint k whose antagonist muscles are i and j is given by:

$$icc_k(t) = min\left(u^i_{norm}(t), u^j_{norm}(t)\right) \tag{3.2}$$

It is also worth mentioning that the ICC does not provide a direct measurement of joint stiffness. It is only directly proportional to the joint stiffness. This means that whenever a joint is more or less stiffen the ICC related to the joint will increase or decrease.

3.3 Conclusions

EMG signals may be used to obtain information regarding motion intentions, and to estimate human joint stiffnesses. Nonetheless, the signal acquisition has to be taken very meticulously so that the signal does not show large noise, and can be interpreted correctly.

Chapter 4

Manipulation Experiments

In order to develop adequate, and efficient robot controllers for HRC, this work investigated patterns in co-manipulation scenarios. Analysis regarding kinematic data, muscle activation data, and custom performance criteria were performed based on the tools provided in the last chapters. This chapter follows by presenting hypotheses about human natural behavior during co-manipulation of an object. The hypotheses were tested by 2 manipulation experiments, one with a single human subject, and another with a HH dyad. The chapter finishes by discussing and concluding about the results in hand.

4.1 Human Motor Behavior Assumptions

In this work, it is considered that in a co-manipulation task, the agent behaving as a leader will dictate the trajectory of the object being co-manipulated as much as possible. So, assigning the role of a leader to a different agent in the dyad may have an impact on the object trajectory. Which leads us to the first hypothesis:

Hypothesis 1. *The manipulated object trajectory changes according to the agent role (leader or follower).*

In addition, since humans modulate their muscles stiffnesses based on their desired level of accuracy to execute a certain task (Burdet *et al.*, 2001; Paul L. Gribble and Mattar, 2003), we hypothesize that the agent behaving as a leader perceives the haptic interaction with the other agent as a disturbance to the execution of its own desired trajectory. Therefore, he/she will increase his/her stiffness to improve his/her own accuracy. Hence, this leads to the second hypothesis:

Hypothesis 2. *A human leader manipulates the object with a higher endpoint stiffness than when behaving as a follower.*

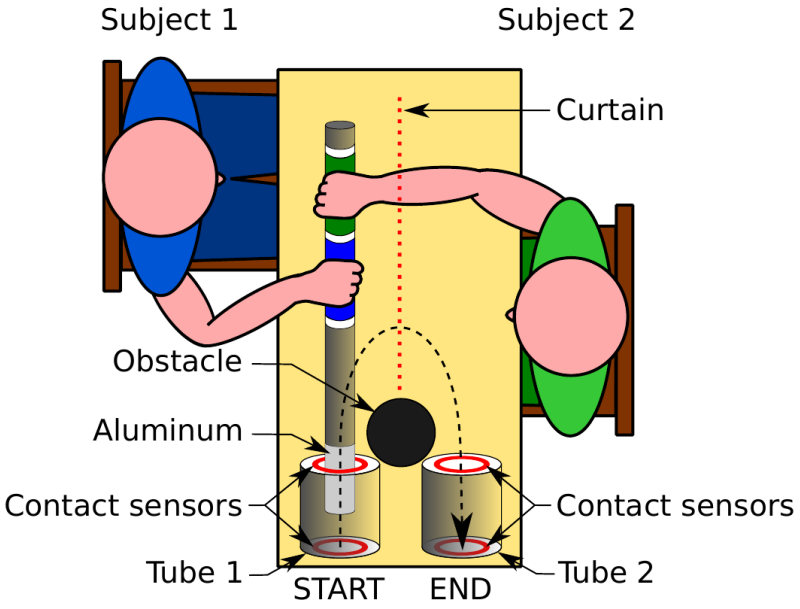

Figure 4.1: Top-down view of the experiment set-up. The black dashed line approximates the pipe trajectory. The red circles are metallic rings attached to the walls of the tubes in order to detect contact with the aluminum that is wrapped around the end of the pipe. The red dashed line represents a curtain placed between both participants.

4.2 Dyad Co-Manipulation Experiment

In order to verify the aforementioned hypotheses, an experiment comprising a HH dyadic co-manipulation of an object was designed. In the experiment, the humans were assigned different roles, and had to constantly collaborate towards a common goal.

4.2.1 Task Description

This experiment demands a HH dyad to co-manipulate a pipe throughout a task that requires bringing the end of a pipe from a start point to an end point (fig. 4.1).

Each participant is asked to sit on a chair, and before the experiment, he/she may adjust the chair position to his/her better comfort. During the experiment participants are instructed to avoid moving their backs during the task execution. However, they are not strapped to the chair.

The participants were instructed to hold the pipe with their right hand with a power grasp, holding the pipe on one of the designated handles (according to their places, like in fig. 4.1).

Initially, the pipe is in contact with the back wall of tube 1 (wall farther away from the subjects), and it has to be to be brought out of the tube 1 while avoiding contact with the front wall (closer to the subjects).

Once out of tube 1, the pipe has to be moved around a cylindrical obstacle, and

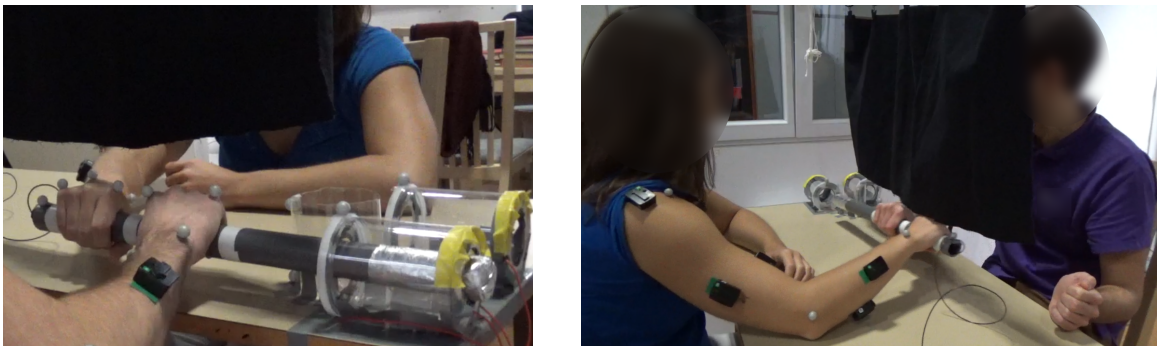

(a) View from subject 1 (b) View from subject 2

Figure 4.2: HH dyad experiment in execution

then inserted into tube 2, once again avoiding the front wall, until the end of the pipe is placed in contact with the back wall of tube 2. The return motion is not recorded nor evaluated.

The task may be classified in three phases according to its physical restrictions:

- Tube 1 restriction;
- Free space;
- Tube 2 restriction;

Although there are no clear physical restrictions to the movement in the free space phase, the participants are instructed to move the pipe around the obstacle, rather than moving the pipe above it.

During any HH dyadic collaboration task, mutual gaze and joint attention are known forms of communication between the dyad agents (Ajoudani *et al.*, 2017b; Tomasello, 2009). In this experiment, any form of audiovisual communication in between the participants was kept away in order to focus on haptic communication.

Hence, a curtain is placed between both participants to prevent visual contact during the task execution (fig. 4.2). In addition, participants were instructed not to talk during the task execution, and not to talk about the experiment in between trials.

Participants do not see any timer during the experiment, but they are told that the whole manipulation (from Start to End) should not take longer than 15 s. If participants take more than 15 s, they are told so and the trial is canceled.

4.2.2 Materials

The manipulated pipe has a 3 cm diameter, a 48 cm length (fig. 4.3). The end of the pipe is covered with aluminum foil for use with the contact sensors mounted on the tube walls. This aluminum part is 8 cm wide, so that it is impossible for the

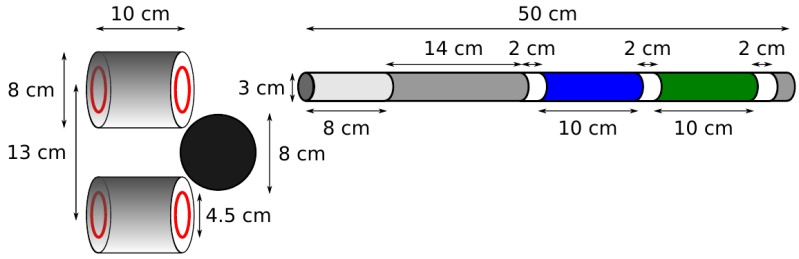

Figure 4.3: Dimensions for the manipulated pipe, for the tubes, and for the cylindrical obstacle

contact sensor to detect a contact at two different walls simultaneously. The handles are 10 cm wide each. Furthermore, the pipe as a whole, weights 218 g.

Each tube is 10 cm long, with a diameter of 8 cm. The diameter of the holes in the front and back walls of each tube is 4.5 cm. The obstacle is a vertical transparent cylinder of diameter 8 cm. Both tubes are set 13 cm apart (distance between the centers of the tubes).

4.2.3 Participants

This experiment was executed by 8 different dyads, therefore, 16 subjects of which 13 were male, and 3 were female. The average age of the subjects was 25.8 years old, the youngest subject was 22 years old, and the oldest was 32 years old. Moreover, 13 subjects were right handed, and only 3 subjects were left handed.

Every subject signed consent forms for their participation and some subjects signed forms for use of their image (photo/video). No participant claimed any chronic motor disease, or health condition that could influence in the experiment results.

4.2.4 Protocol

Each participant was instructed to sit on a chair at one side of the experiment's table according to the number he/she was assigned, either *subject 1* or *subject 2* (fig. 4.1). Subject 1 handles the pipe at handle 1, and subject 2 at handle 2. The subject number is assigned randomly prior to the experiment execution.

The participants execute the task under 3 different behavior conditions:

- *Natural Behavior (no leader/follower role assigned):* Participants are instructed to manipulate the pipe as naturally as possible;
- *Subject 1 Leader and Subject 2 Follower*: Participants are instructed that Subject 1 must lead the movement, while Subject 2 serves the purpose of supporting and following Subject 1's actions;

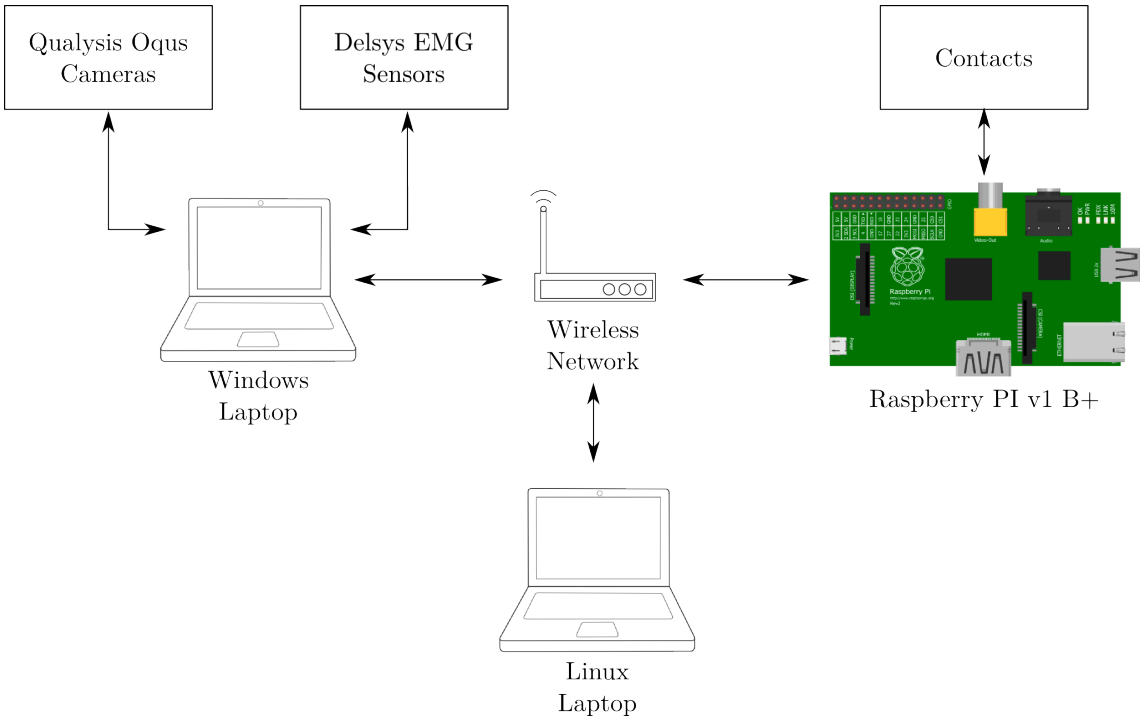

Figure 4.4: Diagram with the sensors and equipment used for data collection.

- *Subject 2 Leader and Subject 1 Follower*: Participants are instructed that Subject 2 must lead the movement, while Subject 1 serves the purpose of supporting and following Subject 1's actions;

The order of the 3 conditions is randomized across dyads to counter-balance any possible effect of human motor learning.

Dyads perform 5 trials for each condition, resulting in a total of 15 trials. For each of the 3 conditions, before starting the recording, the participants can practice for 2 or 3 trials. There is an approximate 45 s break between each trial, but the exact duration of the break is not imposed (participants decide when they want to start the next trial).

4.2.5 Measurements

Figure 4.4 summarizes the equipments used to acquire data for this experiment. The windows laptop synchronizes the data acquisition from Qualysis and Delsys through their proprietary software. The Linux laptop is used to collect data from the contact sensor, and executes a graphical interface for custom software.

Motion Capture

The motion of the participants' right arm is recorded with a Qualisys optical motion capture system with 8 Oqus cameras recording at the rate of 150 Hz. 6 reflective

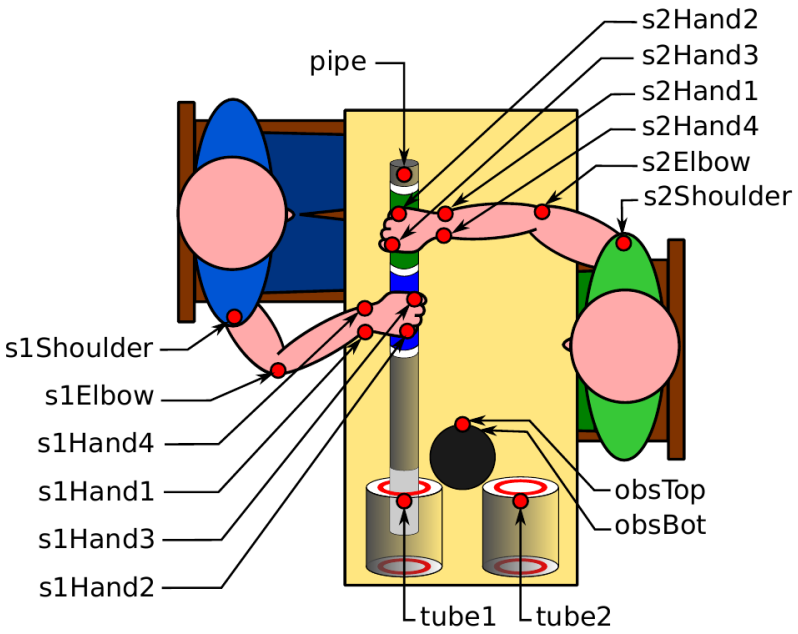

Figure 4.5: Positions and labels of the Qualisys reflective markers placed on the subjects: 6 markers are set on each participant right arm, and 5 markers are set on the pipe, tubes and obstacle. Note that the *obsBottom* marker set on the obstacle is not visible, because it is vertically aligned with the *obsTop* marker.

markers are placed on the participant arm, and their 3D positions in the operational space are tracked. The position of the 6 arm markers are fixed on top of some of the arm bones (fig. 4.5):

- Acromion (referred as *Shoulder*);
- Lateral Epicondyle of the Humerus (referred as *Elbow*);
- Ulnar-Styloid Process (referred as *Hand1*)
- Head of the 5th Metacarpal (referred as *Hand2*);
- Head of the 2nd Metacarpal (referred as *Hand3*);
- Radial-Styloid Process (referred as *Hand4*);

There is also a marker on the pipe to improve position tracking, and additional markers at inertial references like the tubes and obstacle (fig. 4.5):

- At end of the pipe, opposite to the aluminum foil (referred as *pipe*). Participants were told to hold the pipe so that this marker is always facing up;
- At the top of the front wall of each tube (referred as *tube1* and *tube2*);
- At the top of the obstacle wall, farthest away from both tubes (referred as *obsTop*);

- At the bottom of the obstacle wall, farthest away from both tubes (referred as *obsBot*);

EMG

During this experiment, 6 wireless Delsys Trigno EMG sensors were used on 3 pairs of muscles to indicate stiffness at three human arm joints:

- Shoulder Joint:
  - Deltoid Anterior (DA);
  - Deltoid Posterior (DP);
- Elbow Joint:
  - Biceps Brachii (BIC);
  - Triceps (lateral head) (TRI);
- Wrist Joint:
  - Flexor Carpi Ulnaris (FCR);
  - Extensor Carpi Ulnaris (ECR);

The muscles were located according to Perroto (2011). And as described in the chapter 3, a series of isometric exercises was performed for each muscle in order to obtain a MVC prior to the actual experiment. The subjects were asked to contract their muscles as strong and as quick as possible. There were 1 min intervals between the contractions to avoid fatigue, which could bias the MVC acquisition.

During the MVC acquisition only the EMG signal is recorded through a custom MVC calibration software developed especially for this experiment that can be found in: `www.github.com/inria-larsen/emg-processing`. The custom software GUI allows for quick EMG signal verification, simple MVC acquisition, and is intended to serve as a basis for a more ambitious HRC software in the future.

For both the experiment and the MVC calibration, the EMG signal was recorded at a sampling rate of 2 kHz.

Contact Sensor

The experiment participants are explicitly instructed to avoid touching the tube wall with the pipe, when either exiting tube 1 or entering tube 2. This requirement turns the first and the last phase of the experiment into tasks that require a certain level of accuracy. To obtain a qualitative measure of how well the dyad is executing the task, a custom contact sensor is employed.

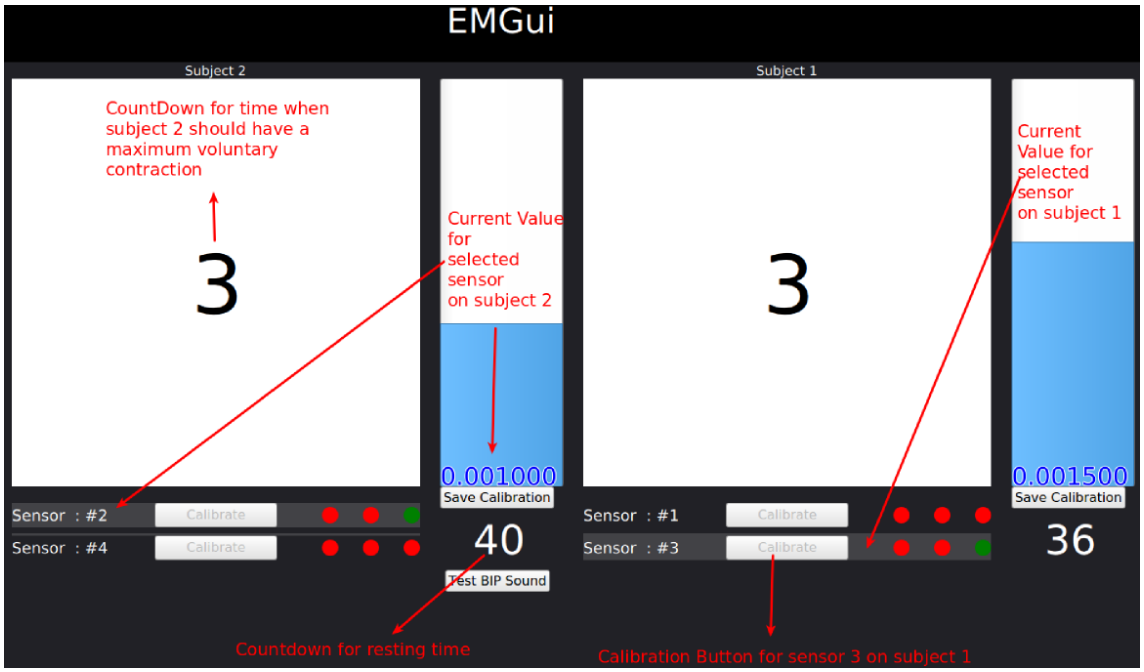

Figure 4.6: EMG custom software for MVC acquisition (`www.github.com/inria-larsen/emg-processing`).

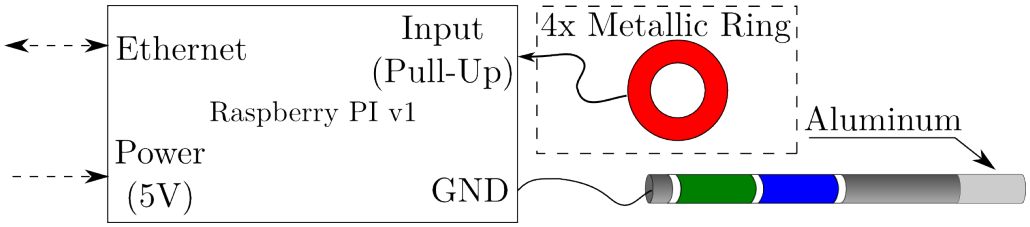

Figure 4.7: Custom Contact Sensor Diagram. Whenever the aluminum touches any of the metallic rings, the Raspberry PI will log the contact onset. The board receives commands through a SSH connection via Ethernet.

The contact sensor is implemented with a Raspberry Pi v1.0 board mounted underneath the table of the experiment. One of the board GPIOs is connected to the pipe via a long wire that is wrapped around the pipe end along with aluminum foil. Additional GPIOs are connected to metallic rings mounted on the tube walls (fig. 4.7).

The board is programmed so that only the onset of a contact between the aluminum foil and any of the metallic rings is logged. That is, whatever the duration of the contact, it will only be logged once as long as it is maintained.

4.2.6 Results

Before discussing the data analysis and results of this experiment, it is important to note that during data analysis subjects in dyad 1 did not follow the task instructions for some trials, having moved the object over the obstacle and not around it as it was

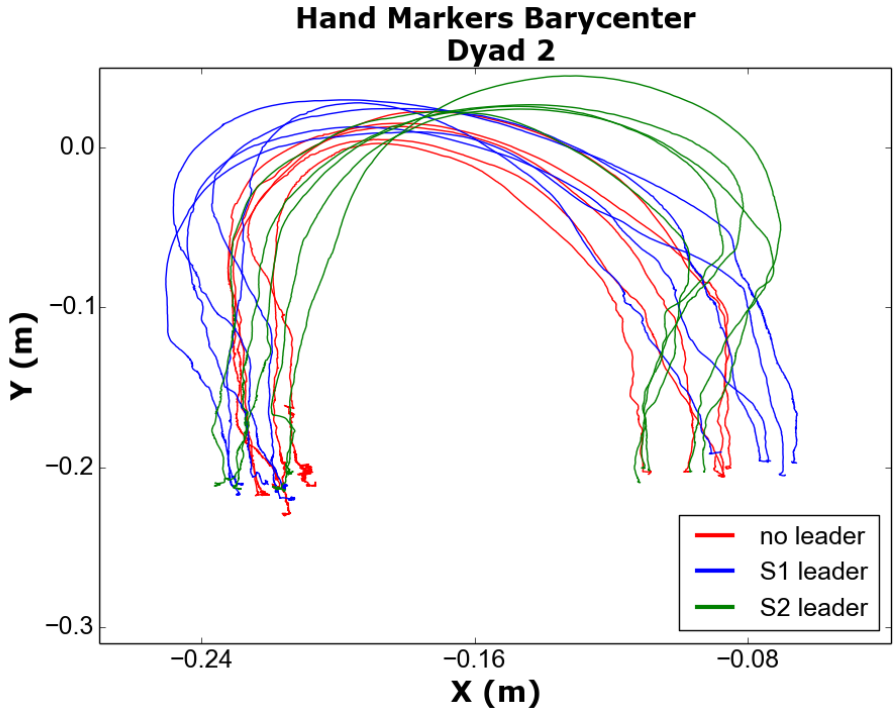

Figure 4.8: Trajectory of the barycenter of the position of the hand markers from both subjects in dyad 2.

explicitly asked, therefore, it was not possible to properly compare and analyze dyad 1 data with the other dyads. For that reason, dyad 1 data analysis was discarded of this section.

It is also important to note that even though the left handed subjects executed the experiment with their right hand the results were similar to the results from the right handed subjects.

The results for all analyzed dyads are explained in detail in the next sections, however, for the trajectory and co-contraction analysis only the plots for dyad 2 are shown. For all the plots, please refer to appendices A and C.

Trajectory

With the purpose of analyzing the object trajectory (position in time), the motion capture marker referred as *pipe* was placed on one of the pipe ends, but in order to improve the tracking robustness the centroid or geometric barycenter of the markers placed on the subjects' hands (fig. 4.5) was calculated at every time instant instead. The variations in trajectory for this task are mostly planar, so the barycenter was analyzed only on the X-Y plane.

The trajectories did change according to whom was assigned the role of the leader of the task (as illustrated by dyad 2 in fig. 4.8). Furthermore, the trajectory was bent towards the task leader, such that when the dyad was told to behave naturally

the trajectory was in between the trajectories with a preassigned leader. These patterns strongly support hypothesis 1.

Co-Contraction

For the 3 pairs of antagonist muscles whose EMG signals were acquired during the experiment, an ICC signal was calculated as in eq. 3.2.

During preliminary analysis, it was found that the pair of muscles for the shoulder joint (DA-DP), and for the elbow joint (BIC-TRI) showed very small values for their respective ICCs, or no variation during the executed task, therefore, the ICC analysis hereafter, covers only the pair of muscles at the forearm (ECR-FCR) related to the wrist joint [1]. It is also noted that in previous related works (Grafakos *et al.*, 2016; Peternel *et al.*, 2016, 2017), the authors also took the decision to use only one joint (either the wrist joint or the elbow joint) for ICC analysis.

In fig. 4.9 it is possible to see the ICC for the forearm muscles of subjects 1 and 2 that form dyad 2 while executing the experiment task. Furthermore, from fig. 4.9 (and the other plots in appendix A) it is possible to observe a trend in certain subjects that relates individual ICC variations that can be summarized in the following inequality:

$$icc^s_{fol} < icc^s_{nat} < icc^s_{lead} \tag{4.1}$$

where,

- icc^s_{fol} is the ICC value for a subject s behaving as a follower in the dyad;
- icc^s_{nat} is the ICC value for a subject s behaving without any pre-assigned behavior, as naturally as possible;
- icc^s_{lead} is the ICC value for a subject s behaving as a leader in the dyad;

[1] Nonetheless, the EMG signals for all joints are still acquired in case they are needed for future work.

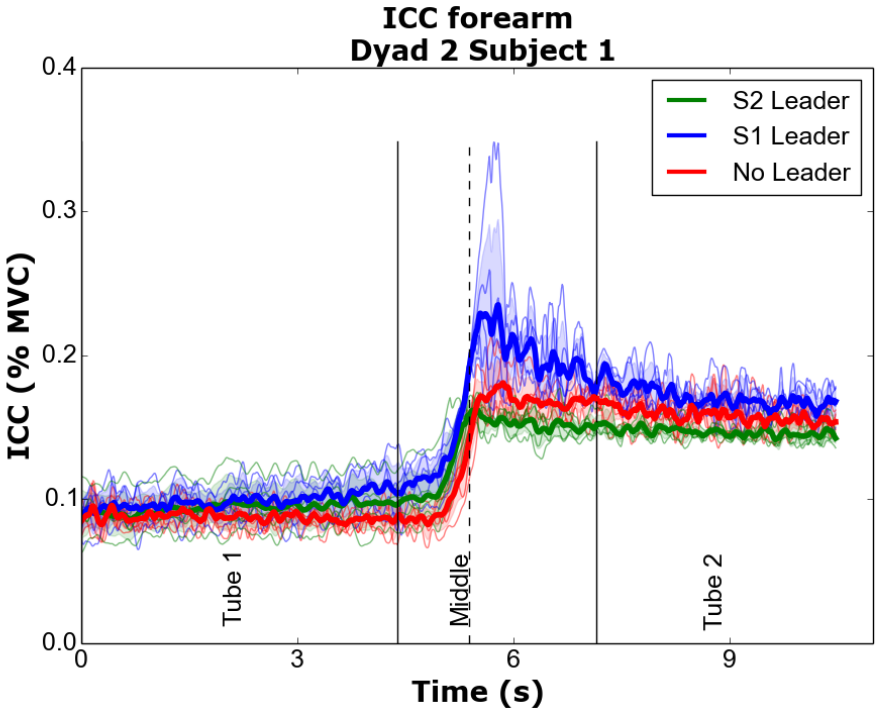

(a) Subject 1 in dyad 2.

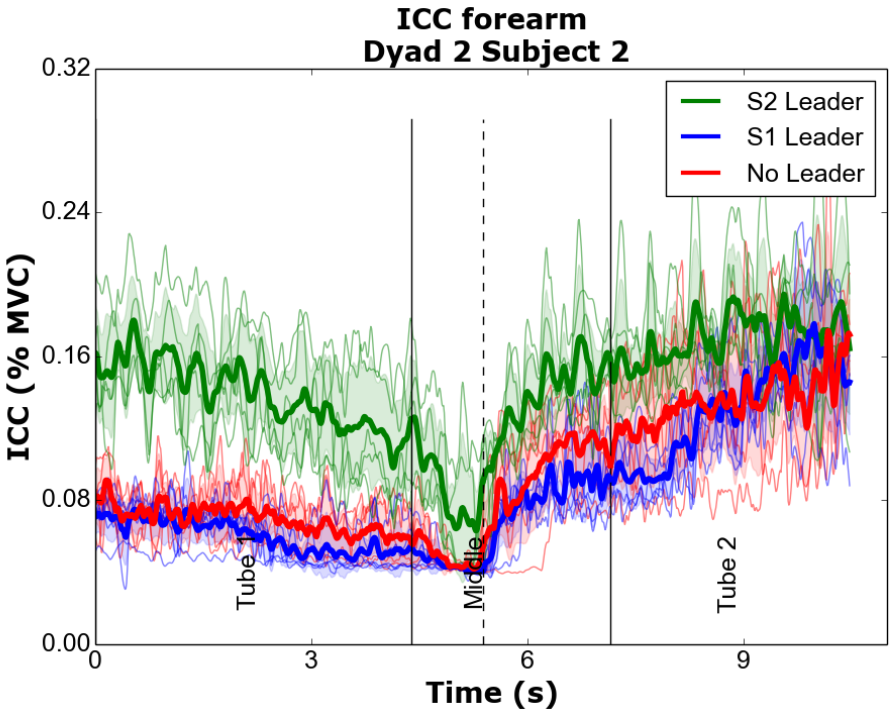

(b) Subject 2 in dyad 2.

Figure 4.9: ICC acquired from forearm muscles relative to the wrist joint. Taken from dyad 2. The average for every trial is in bold color; in light color, every trial; and the shades represent the standard deviation from the average. The plots are time normalized for every dyad. Furthermore, the dashed vertical line represent the time instant when the subject hands barycenter crosses the curtain line (fig. 4.1). With the barycenter, and the measurements from fig. 4.3, it is possible to calculate when the aluminum end of the pipe leaves tube 1, and when it enters tube 2. Those instants are shown in the plots as vertical lines, and they delimit the task phases: restricted by tube 1; free space; and restricted by tube 2.

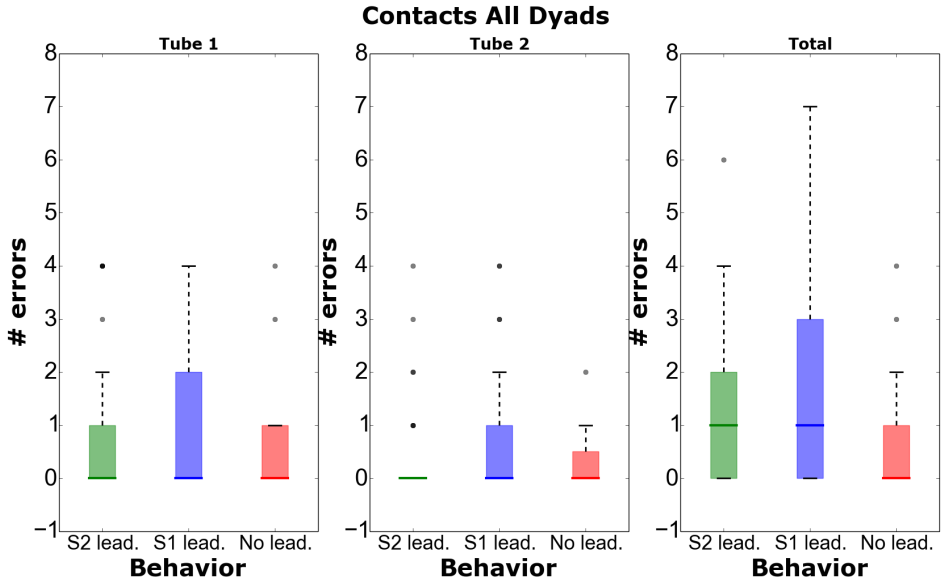

Figure 4.10: Box plots of task execution error measurement acquired by contact sensor during HH dyad experiment.

Task Performance

To measure the performance of the dyads while executing the task, the number of times the aluminum part of the pipe touches the walls of the tubes is acquired by the contact sensor. The contacts at the start and at the end of the task trajectory are only used to delimit the task period, while the contacts sensed when the pipe is leaving tube 1, and entering tube 2 are counted as errors. It is worth mentioning that whenever the aluminum part is dragged while maintaining contact with the sensors several touches are perceived by the sensor. If this happens, the contacts are only counted as one in this analysis.

Figure 4.10 shows box plots of the number of errors for all dyads in tube 1, tube 2, and for both tubes. As a reminder, tube 1 is closer to subject 1, and tube 2 is closer to subject 2 (fig. 4.1).

4.2.7 Discussion

From the trajectories results, beyond supporting the hypothesis 1, it is possible that the variation in the planar trajectory is related to every subject having his/her own desired trajectory, to which he/she tries to follow, especially when he/she is leading the task. This would also implicate that when both subjects are instructed to behave as naturally as possible, their trajectories blend into a new trajectory.

In addition, the cause for the change in trajectory for different role assignments seems to be related with the results from the co-contraction measurements, which are summarized by the inequality (4.1). A high ICC for subject 1 (stiff behavior),

combined with a low ICC for subject 2 (compliant behavior) would result in a better tracking of subject 1 desired trajectory, and vice-versa. Consequently, mid-values of stiffness/compliance for both subjects would result in the blend trajectories perceived by the motion capture system. Furthermore, inequality (4.1) also strongly supports hypotheses 2.

Complementary information from the task performance analysis (fig. 4.10) showed that the number of errors significantly decreases in both tubes whenever the subjects are not assigned a specific role. Therefore, the HH dyad was more efficient when acting naturally. This evokes the idea that humans naturally modulate their stiffness to mid values in order to generate more efficient trajectories. In addition, it is also worth mentioning that mid values of ICC mean less energy spent by the subjects individually, and this could mean that the subjects optimize not only for the desired trajectory tracking but also for individual energy consumption.

On the other hand, it is also possible that the desired trajectory for each of the agents is optimal for different periods of the task, and that every agent tries to minimize his/her stiffness while trying to execute his/her own trajectory. This is also suggested by the fact that errors were generally smaller for the tubes closer to the leaders.

4.3 Single Human Manipulation Experiment

The dyad experiment raised some questions, one of which was related to the form of the ICC signal (fig. 4.9), that changed more noticeably during free space phase of the task, increasing for subject 1, and decreasing for subject 2. This variation could be related to dyad impedance communication similar to what was studied in Mojtahedi *et al.* (2017), or it could also be related to kinematic constraints of the task, and to the individual arm manipulability.In order to try to answer some of those questions a second experiment was designed.

4.3.1 Task Description

This experiment is similar to the first one but with some key differences. The manipulation task is not shared, so there is only one human executing the experiment; and EMG sensors are only placed in the forearm of the participants. The participants were also asked to grab the pipe in the middle of both handles instead of grabbing the handles for subject 1 or 2. The other equipments and measurements are the same from the HH dyad experiment.

4.3.2 Participants

There were 6 participants. They were in average 26.7 years old, the oldest was 29 years old, and the youngest was 23 years old. This time, every participant was right handed. The participants were not aware of the preliminary results from the HH experiment.

Once again, every subject signed consent forms for their participation and some subjects signed forms for use of their image (photo/video). No participant claimed any chronic motor disease, or health condition that could influence in the experiment results.

4.3.3 Protocol

There were no role assignments since there is only one participant. However, there were two different conditions: participant sat at the position of the subject 1; participant sat at the position of subject 2 (fig. 4.1). The conditions were assigned at random. There were 5 trials for each condition, two learning trials in between conditions, and approximately a 45 s break between trials.

4.3.4 Results

The results for all participants are described in detail in the next sections, however, for the trajectory and co-contraction analysis only the plots for participant 4 are shown. For all the plots, please refer to appendices B and D.

Planar Trajectory

With only one participant, the trajectory is the geometric barycenter of the markers on the single participant hand. The planar trajectory for participant 4 is shown in figure 4.11.

In this experiment, the object trajectory still deviates toward the participant, but this time the deviation is much more accentuated. This reinforces the initial hypothesis 1, and the discussed idea that every person has its own desired trajectory.

Co-Contraction

The ICC levels during task execution (fig. 4.12) for all dyads varied inconsistently regarding the object trajectory. For some participants, the ICC level varied when moving the pipe away or inserting it in the tubes, and for other participants it did not change during the whole task.

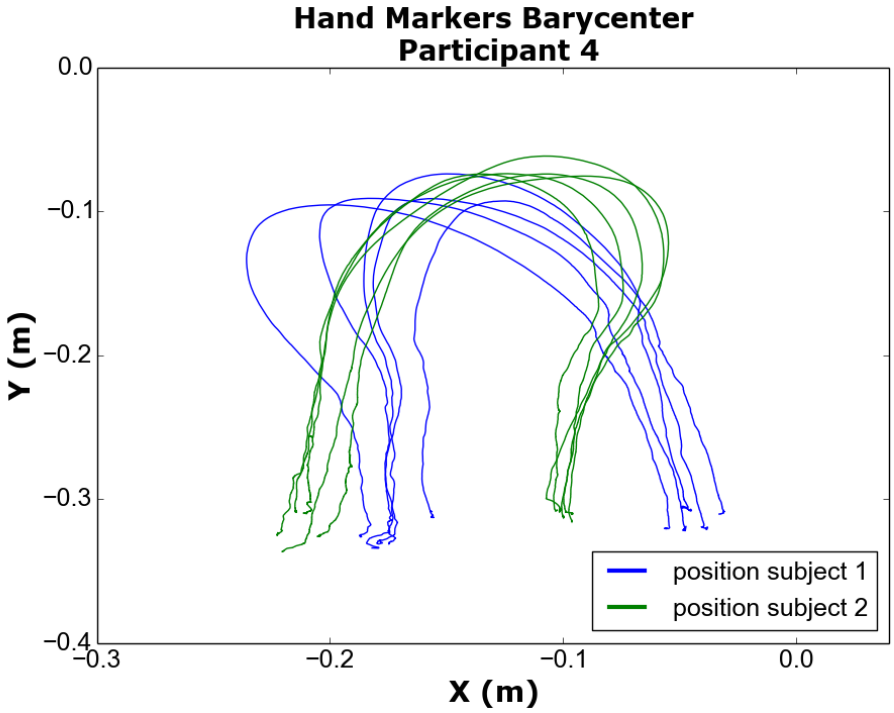

Figure 4.11: Trajectory of the barycenter of the position of the hand markers from participant 4 in single human experiment.

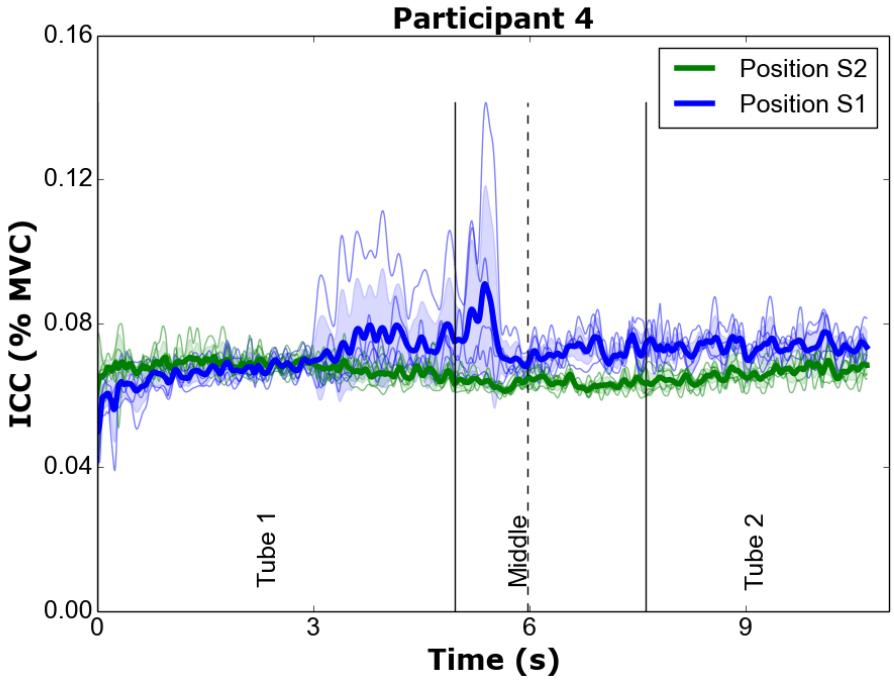

Figure 4.12: ICC acquired from forearm muscles relative to the wrist joint of participant 4 in the single human experiment.

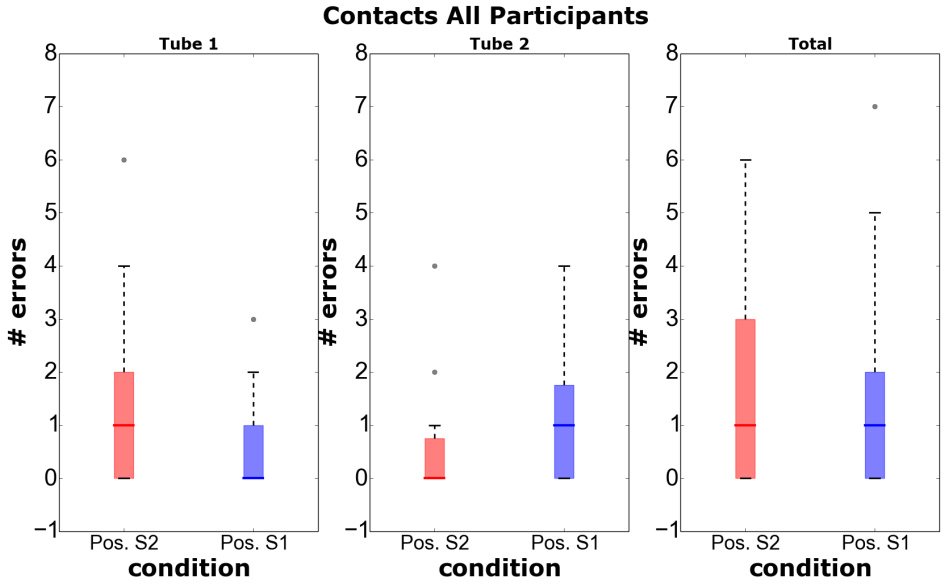

Figure 4.13: Box plots of task execution error measurement acquired by contact sensor during single human experiment

Task Performance

The contact sensor measurement for all participants can be seen on fig. 4.13. This time, the errors on the tube that it is closer to the participant are fewer than errors measured on the tube further away. In the dyad experiment, this happened only for one of the dyads. The total number of errors, however, is larger than for the dyad experiment.

4.3.5 Discussion

The results from the trajectory analysis indicate that for this experiment, the position on which a human is sitting is decisive to his/her desired trajectory. Furthermore, even though the experiments' setup was designed so that in any position the human participant would be able to properly view the object and the tubes at all times, the task performance results (better performance when closer to the tube) indicate that the participant has a better expertise of the task when closer to the tubes. However, when the task performance results are compared to the dyad experiment the participants did not perform as well as the dyads without preassigned roles. Therefore, it is possible that even though humans may perceive each other as disturbances to their own desired trajectories, the final result of the dyad is generally better than when compared to a single person acting alone.

The inconsistency regarding the variation of co-contraction may be related to changes in manipulability instead of the desired object trajectory, or the position in which the participant was sitting. Future work should define manipulability

measures and verify their relationship with ICC variations both for a HH dyad and for a single participant.

4.4 Conclusions

Although more trials for both experiments are needed to ensure statistical significance, it is already possible to infer that a human subject in a dyad increases his/her arm endpoint stiffness when acting as a leader, and decreases it when acting as a follower.

The results also support that each human has its own desired trajectory for the object manipulation and the object trajectory is a blend between the desired trajectories of both agents in the dyad.

And it is likely that the change in stiffness for each agent in the dyad is the cause for the change in the object trajectory.

Chapter 5

Admittance Robot Controller for Human-Robot Co-Manipulation

The previous chapter presented a situation in which a HH dyad behave naturally when co-manipulating an object, and how a HH dyad could be more efficient with respect to a custom performance criteria than a single human manipulating the same object. To replicate this behavior in a HR dyad, this chapter delves into the development of an admittance robot controller designed to provide the robot either a follower or a leader behavior based on a scalar parameter. The stability of the desired admittance is also evaluated by Lyapunov theory.

To illustrate the controller usage, simulations are done with a 3DoF kinematic planar robot, and with a 7DoF robot in a dynamic simulation. Furthermore, a real 7Dof robot is used with a virtual human force.

5.1 Robot Controller Design

The experiments in chapter 4 may suggest that humans in a HH dyad modulate their endpoint stiffness differently when they have been preassigned different roles (leader or follower). Furthermore, for not preassigned roles, the object trajectory seems to be an interpolation between the desired trajectories of both agents because of the humans' mid value endpoint stiffnesses.

Inspired by the stiffness variation with respect to the change in role assignments observed in chapter 4, it is proposed a continuously differentiable scalar role factor $\alpha(t) \in [0, 1] \quad \forall t \geq 0$ such that $\alpha = 0$ assigns to the robot a total leader desired stiffness, $\alpha = 1$ assigns to the robot a total follower stiffness, and the condition $0 < \alpha < 1$ assigns mid value stiffness comparable to the mid value stiffness from the HH dyad experiment, *i.e*:

$$\text{Robot Role Behavior} : \begin{cases} \alpha(t) = 0, & \text{Total Leader} \\ \alpha(t) = 1, & \text{Total Follower} \\ 0 < \alpha(t) < 1, & \text{Mixed} \end{cases} \tag{5.1}$$

The purpose of the role factor $\alpha(t)$ is to define a role to the robot. The role can be defined in different ways, for example, from a manipulability measure (section 2.3.3), or any intention of motion metric (section 1.1.3) from the human partner in the HR dyad. To replicate the results from the HH dyad experiment, $\alpha(t)$ is defined here proportional to the ICC levels around the wrist joint of the human partner, and since the human ICC is bound by individual minimum and maximum values of ICC (respectively acting as a follower or as a leader), α is given by:

$$\alpha(t) = \frac{icc(t) - icc_{min}}{icc_{MAX} - icc_{min}} \tag{5.2}$$

where the individual ICC limits (icc_{min}, icc_{MAX}) are obtained from a calibration task prior to the co-manipulation task, and after the isometric exercises that acquire MVC values for each muscle.

Now, let the robot EEF real position[1] be $x_e(t)$, and the desired robot trajectory be described by $x_r(t), \dot{x}_r(t), \ddot{x}_r(t)$, then the robot position error defined as:

$$e_r(t) := x_e(t) - x_r(t) \tag{5.3}$$

Even though for most case scenarios it is not possible to know the human desired trajectory, $x_h(t)$, the human position error is defined as:

$$e_h(t) := x_e(t) - x_h(t) \tag{5.4}$$

The desired robot behavior defined by (5.1) aims a total leader behavior ($\alpha = 0$) characterized by:

$$\lim_{t \to \infty} e_r(t) = 0 \tag{5.5}$$

and the total follower behavior ($\alpha = 1$) characterized by:

$$\lim_{t \to \infty} e_h(t) = 0 \tag{5.6}$$

Let the robot equation of motion in the operational space ($\mathbb{R}^3$ or $\mathbb{R}^2$) be:

$$\Lambda(q)\ddot{x}_e + \mu(q, \dot{q})\dot{x}_e + F_g(q) = F_h \tag{5.7}$$

[1]Similar to the manipulation experiments, the task here is described by its position only, without considerations on orientation

where $\Lambda(q) \in \mathbb{R}^{3\times3}$ is the EEF apparent inertia matrix, $\mu\dot{x}_e$ represents the forces at the EEF correspondent to the Coriolis matrix in joint space, F_g the force at the EEF correspondent to the gravitational torques, and F_h is the force applied by the human at the robot EEF.

Similarly to Li *et al.* (2015a,b), an impedance model in the operational space with a varying desired stiffness and damping is proposed in order to adapt the robot role:

$$\Lambda_d\ddot{e}_r(t) + D_d(t)\dot{e}_r(t) + K_d(t)e_r(t) = F_h(t) \tag{5.8}$$

where $\Lambda_d \in \mathbb{R}^{3\times3}, D_d \in \mathbb{R}^{3\times3}, K_d(t) \in \mathbb{R}^{3\times3}$ are the desired inertia, damping, and stiffness matrices, such that all of them are positive definite and symmetric for all $t \geq 0$. In addition, Λ_d is a decoupled inertia matrix such that:

$$\Lambda_d = \begin{pmatrix} m_d & 0 & 0 \\ 0 & m_d & 0 \\ 0 & 0 & m_d \end{pmatrix} \tag{5.9}$$

Then, a varying stiffness profile dependent on $\alpha(t)$ is proposed as:

$$K_d(t) = K_{d0}(1 - \alpha(t)) + K_{d1} \tag{5.10}$$

where $K_{d1} \in \mathbb{R}^{3\times3}$ is the minimum robot stiffness matrix, and $K_{d0} \in \mathbb{R}^{3\times3}$ bounds the maximum robot stiffness. Furthermore, K_{d0}, K_{d1} stiffness matrices are known to produce very stiff, and very compliant behaviors respectively.

In addition, the varying damping profile is defined as the critical damping, *i.e.*:

$$D_d(t) = 2\sqrt{K_d(t)m_d} \tag{5.11}$$

As in section 2.6.2, in order to implement (5.8) with an admittance controller block, e_r is substituted by $(x_{ref} - x_r)$, *i.e*:

$$\Lambda_d\left(\ddot{x}_{ref} - \ddot{x}_r\right) + D_d\left(\dot{x}_{ref} - \dot{x}_r\right) + K_d(t)\left(x_{ref} - x_r\right) = F_h(t) \tag{5.12}$$

and the internal kinematic controller, similar to (2.53), is given by:

$$\dot{q} = J^{\dagger}(\dot{x}_{ref} - K_p\left(x_e - x_{ref}\right)) \tag{5.13}$$

The admittance control strategy is summarized in fig. 5.1.

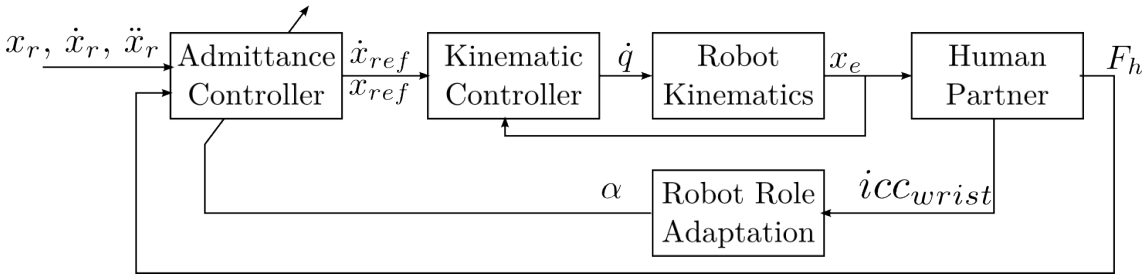

Figure 5.1: Diagram for robot admittance control in a HR dyadic co-manipulation with online robot adaptation based on an ICC signal from the human partner

5.2 Effect on Object Trajectory

The experiments in chapter 4 suggest that the change in stiffness from both subjects is the cause for the change in the object trajectory. In addition, the robot admittance controller proposed aims to replicate the same patterns (eq. (5.3), (5.4)). Therefore, the system in fig. 5.1 needs to be verified analytically for its effects on the object trajectory, which is done in the remainder of this section.

It is hard to simulate perfectly the human natural behavior analytically, but with the purpose of a qualitative analysis, the human force, $F_h(t)$ is considered here to be based on the role factor $\alpha(t)$. The definition of $\alpha(t)$ used in this work (eq. 5.2) states that $\alpha(t)$ is proportional to the ICC around the wrist joint. Moreover, from the discussion in chapters 3 and 4 it is considered that the ICC is an image of the actual joint and human endpoint stiffness. Therefore, it is possible to estimate the human endpoint stiffness $K_h \in \mathbb{R}^{3\times3}$ using a maximum value for the stiffness $K_{h0} \in \mathbb{R}^{3\times3}$, and $\alpha(t)$:

$$K_h(t) = \alpha(t)K_{h0} \tag{5.14}$$

Furthermore, assuming that every human agent has its own desired trajectory for manipulation tasks, the force that the human applies at the robot EEF is similar to a spring with an equilibrium point at the human desired trajectory:

$$F_h(t) = -K_h(t)e_h(t) \tag{5.15}$$

Substituting eq. 5.15 into 5.8, *i.e*:

$$\Lambda_d\ddot{e}_r(t) + D_d(t)\dot{e}_r(t) + K_d(t)e_r(t) = -K_he_h(t) \tag{5.16}$$

In the remainder of this section, with the sole purpose of enabling a simple verification at the boundary conditions of the role switching (total leader, and total follower), α is considered to be constant. With the role factor constant it is possible to apply the Laplace transform at (5.16):

$$s^2\Lambda_d(X_e - X_r) + sD_d(X_e - X_r) + K_d(X_e - X_r) = -K_H X_h \tag{5.17}$$

Then, isolating X_e:

$$X_e = (s^2\Lambda_d + sD_d + K_d + K_h)^{-1}\left((s^2\Lambda_d + sD_d + K_d)X_r + K_h X_h\right) \tag{5.18}$$

Finally, the EEF position can be verified for two conditions: $\alpha = 0$ (robot as total leader); and $\alpha = 1$ (robot as total follower).

- if $\alpha = 0$

Substituting (5.14) and ((5.10)):

$$X_e = (s^2\Lambda_d + sD_d + K_{d0} + K_{d1})^{-1}\left((s^2\Lambda_d + sD_d + K_{d0} + K_{d1})X_r\right) \tag{5.19}$$

implies that when $\alpha = 0$ the EEF position depends only on the robot desired trajectory.

- if $\alpha = 1$

Substituting (5.14) and ((5.10)):

$$X_e = (s^2\Lambda_d + sD_d + K_{d1} + K_h)^{-1}\left((s^2\Lambda_d + sD_d + K_{d1})X_r + K_{h0}X_h\right) \tag{5.20}$$

which implies that if the stiffness terms generate the highest forces in the system (5.16), and K_{d1} defines a small stiffness value (which are usually reasonable conditions), the term in (5.20) associated with X_h has a much higher value than the term associated with X_r. This means, that when $\alpha = 1$ the EEF position depends mostly on the human desired trajectory.

5.3 Stability Analysis

The impedance model (with only one equilibrium point) in eq. (5.16), is guaranteed to be globally asymptotically stable only if the desired stiffness, apparent inertia, and damping matrices are constant, symmetrical, and positive definite. However, in this chapter a varying desired stiffness profile was proposed, so other stability conditions for the system in eq. (5.16) must be found.

In Kronander and Billard (2016), the authors proposed a method to verify stability of mechanical impedance relationships with varying stiffness and damping which is based on the following theorem:

Theorem 1 (Stability Conditions Under Dynamic Decoupling)**.** *Let Λ_d be a constant, symmetric, and positive definite matrix, and $K_d(t), D_d(t)$ be symmetric, positive definite, and continuously differentiable varying stiffness and damping profiles. Then, given $F_e = 0$, the system in eq. (2.66) with varying stiffness and damping profiles is globally asymptotically stable if there exists a $\gamma \in \mathbb{R}^+$, such that $\forall t \geq 0$:*

1. *$\gamma\Lambda_d - D_d(t)$ is negative definite;*
2. *$\dot{K}_d(t) + \gamma\dot{D}_d(t) - 2\gamma K_d(t)$ is negative definite*

The proof for theorem 1 is given in appendix E.

The method in Kronander and Billard (2016) considers that the varying stiffness and damping profiles with respect to time are known *a priori*, which is not the case for this work since $\alpha(t)$ depends on $icc(t)$, that is a signal that depends exclusively on the human agent. So, here, the stability conditions are verified during a HR simulation for 2 different impedance profiles: varying stiffness (5.10); and varying stiffness and damping (5.10),(5.11).

5.3.1 Varying Stiffness

If only the desired stiffness profile varies with time the global asymptotic stability conditions that need to be verified turn into:

$$\gamma\Lambda_d - D_d < 0 \tag{5.21}$$

$$\dot{K}_d(t) - 2\gamma K_d(t) < 0 \tag{5.22}$$

Then, a value of γ that complies with the condition (5.21) $\forall t \geq 0$ may be chosen as:

$$\gamma = min\left(\frac{\lambda_{min}(D_d)}{\lambda_{MAX}(\Lambda_d)}\right) - 1 \tag{5.23}$$

where $\lambda_{min}(\cdot), \lambda_{MAX}(\cdot)$ are the minimum and maximum eigenvalue operators respectively.

5.3.2 Varying Stiffness and Damping

If both the desired stiffness and damping have varying profiles, to comply with the proposed varying damping profile in (5.11), the stability conditions can be rewritten as:

$$\gamma\Lambda_d - D_d < 0 \tag{5.24}$$

$$\dot{k}_y(t)\left(1 + \frac{\gamma m_d}{\sqrt{k_y m_d}}\right) - 2\gamma k_y < 0 \tag{5.25}$$

such that $K_d(t) = k_y I_3$. Note that for this case the γ is chosen as in (5.23).

5.4 Human-Robot Simulation

A human-robot simulation partly inspired in the work in Li *et al.* (2015a) is devised in which a HR contact at a planar robot EEF is expected, and the robot trajectory, $x_r(t)$, and the human trajectory, $x_h(t)$ diverge in certain periods. Moreover, both trajectories are known *a priori*. This emulates situations when the robot is executing a task, but it is not fully aware of its environment and possible obstacles. In this scenario, the human partner would allow the robot to take the leadership of the task while the robot desired trajectory is correct in the eyes of the human, but as soon as the robot desired trajectory becomes problematic for any reason (poor trajectory execution, sudden appearance of obstacles, etc.) the human partner takes the leadership of the task by increasing his/her arm endpoint stiffness.

Firstly, a generic planar 3R robot is kinematically simulated under 4 conditions for $\alpha(t)$: $\alpha = 0$; $\alpha = 1$, $\alpha = 0.5$, and $\alpha(t)$ is adaptive, simulating human motor behavior. For the adaptive α condition, two impedance profiles are simulated: varying stiffness, and varying stiffness and damping. Those conditions with constant α are supposed to give qualitative insight about the controller, and verify the results obtained analytically in the section 5.2. Afterwards, a dynamic simulation of a 7 DoF robot is done under the adaptive α condition.

5.4.1 Planar 3R Robot

In this case, the robot used is a planar robot with 3 revolution joints (fig. 5.2) described by the DH parameters in table 5.1. It is noted that with only the DH parameters of a robot, it is possible to calculate its forward kinematics (Siciliano *et al.*, 2008).

Desired Trajectories

Similarly to (Li *et al.*, 2015a), the robot trajectory is a circular trajectory in the $\vec{x}_b, \vec{y}_b$ plane of the orthogonal frame $\mathcal{F}_b$ placed at the robot base, and it is given by:

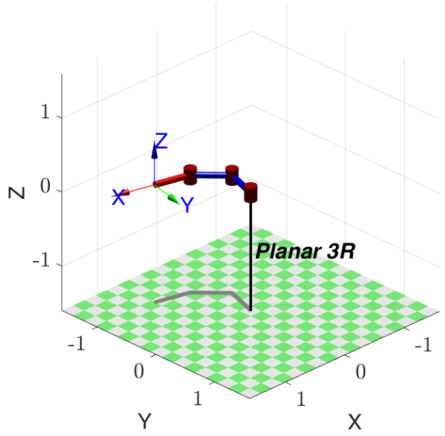

Figure 5.2: Planar robot with 3 revolution joints simulated using the Matlab robotics toolbox (Corke, 2011)

Link i	θ_i	d_i	a_i	α_i
1	θ_1	0	0.5	0
2	θ_2	0	0.5	0
3	θ_3	0	0.5	0

Table 5.1: DH parameters for planar robot

$$x_r(t) = \begin{bmatrix} 0.1\cos(\omega_0 t + \pi/2) \\ 0.4 + 0.1\sin(\omega_0 t) \end{bmatrix} \tag{5.26}$$

where $\omega_0 = \frac{2\pi}{10}$, and the robot trajectory period is 10 s. Meanwhile, the human desired trajectory is given by:

$$x_h(t) = \begin{cases} x_r(t), & t < 1.25 \\ (t-1.25)\frac{p_2-p_1}{1.25} + p_1, & 1.25 \le t < 2.5 \\ (t-2.5)\frac{p_3-p_2}{1.25} + p_2, & 2.5 \le t < 3.75 \\ (t-3.75)\frac{p_4-p_3}{2.5} + p_3, & 3.75 \le t < 6.25 \\ x_r(t), & 6.25 \le t < 10 \end{cases} \tag{5.27}$$

where $p_1 = x_r(1.25)$, $p_2 = [-0.15; 0.4]^\top$, $p_3 = x_r(3.75)$, and $p_4 = x_r(6.25)$ are fixed reference points. And the human trajectory ends at the same time as the robot trajectory. Both trajectories can be seen in fig. 5.3.

Human Stiffness

In this simulation, the human force is once again assumed to correspond to eq. (5.15), and the closed-loop impedance model is given by eq. (5.16). In addition,

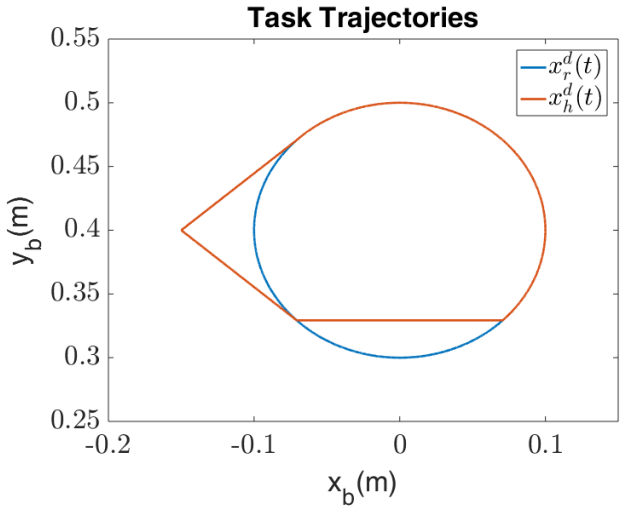

Figure 5.3: Human and robot desired trajectories

Authors	K_h min (N/m)	K_h max (N/m)
Tsumugiwa *et al.* (2002)	0	2400
Duchaine and Gosselin (2008)	1871	5587
Campeau-Lecours *et al.* (2016)	-	550
Ott *et al.* (2010)	10	3200
Ficuciello *et al.* (2015)	-	200

Table 5.2: Human endpoint stiffness values, estimated, or measured in literature

based on the average of the impedance values for the human endpoint stiffness found in literature (table 5.2), a value for the maximum arm endpoint stiffness is defined as:

$$K_{h0} = 2000 I_2 \, (N/m) \tag{5.28}$$

where $I_2 \in \mathbb{R}^{2\times 2}$ is the identity matrix.

Kinematic Controller Parameter

The kinematic controller used by the robot (2.53) has the gain K_p:

$$K_p = 50 I_2 \tag{5.29}$$

Controller Parameters for Varying Stiffness

The robot desired stiffness was defined so that the robot complies with the stability condition in (5.22), and to obtain fast and precise tracking of $x_h(t)$:

$$K_d = \begin{bmatrix} k_x & 0 \\ 0 & k_y \end{bmatrix} = 1000 I_2 (1 - \alpha(t)) + 10 I_2 \tag{5.30}$$

The following desired apparent inertia, and damping matrices are also chosen in such a way that it satisfies the stability condition (5.22) :

$$\Lambda_d = 2I_2 \left(Ns^2/m\right) \tag{5.31}$$

$$D_d = \begin{bmatrix} d_x & 0 \\ 0 & d_y \end{bmatrix} = 32I_2 \left(Ns/m\right) \tag{5.32}$$

With these parameters, considering that $k_x = k_y$, the constant damping ratio, ζ is given by:

$$\zeta = \frac{d_y}{2\sqrt{k_y m_d}} \tag{5.33}$$

and ζ varies from $\zeta = 0.32$ ($\alpha = 0$) to $\zeta = 3.58$ ($\alpha = 1$), which means that the desired impedance is underdamped for low human stiffness, and overdamped for high human stiffness.

Varying Stiffness

For the fixed α conditions, the varying stiffness profile is used, and for the adaptive α condition both profiles are used: varying stiffness (varying ζ); and varying stiffness and damping (constant ζ=1). In the latter case, the *alpha* is adapted through a simulated $icc(t)$ activated by a sigmoid function. The results are shown below.

- Fixed α:

First, the qualitative analysis is verified by simulating the experiment with 3 different fixed values for α: $\alpha = 0$, $\alpha = 0.5$, and $\alpha = 1.0$

For $\alpha = 0$, it can be seen on fig. 5.4 that the EEF almost perfectly follows the robot desired trajectory.

For $\alpha = 1$, it can be seen on fig. 5.5 that the EEF follows the human desired trajectory very closely (as expected from eq. 5.6). The trajectory discontinuities generate some oscillations slightly perceived at the EEF position and trajectory error as well.

For $\alpha = 0.5$, it can be seen on fig. 5.6 that the EEF trajectory is now between the human desired trajectory and the robot desired trajectory. Such behavior highly resembles the mixture of the desired trajectories from the HH dyad experiments when the dyad was asked to behave as naturally as possible.

- Adaptive α with varying stiffness profile:

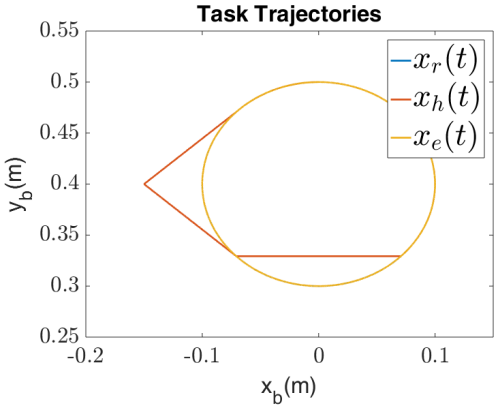

(a) Trajectories on the plane

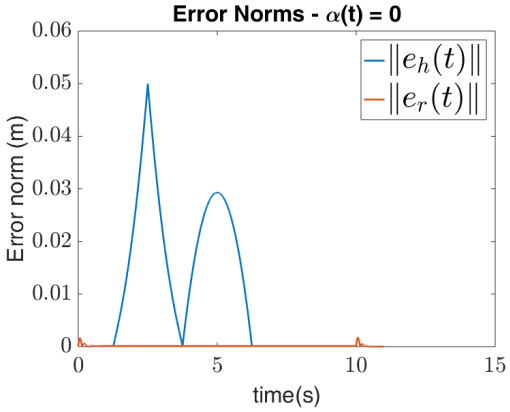

(b) Norm of the errors associated with the robot and human desired Trajectories

Figure 5.4: EEF position for $\alpha = 0$

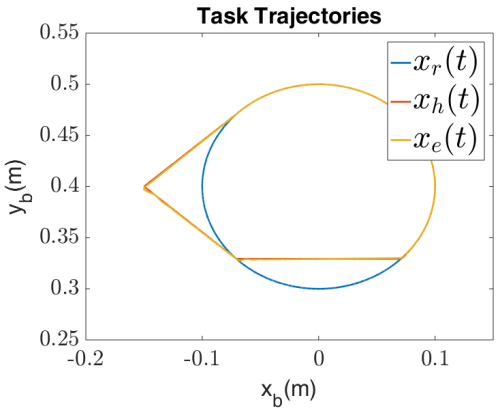

(a) Trajectories on the plane

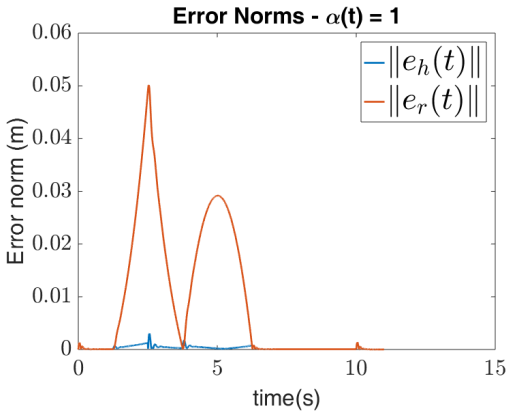

(b) Norm of the errors associated with the robot and human desired Trajectories

Figure 5.5: EEF position for $\alpha = 1$

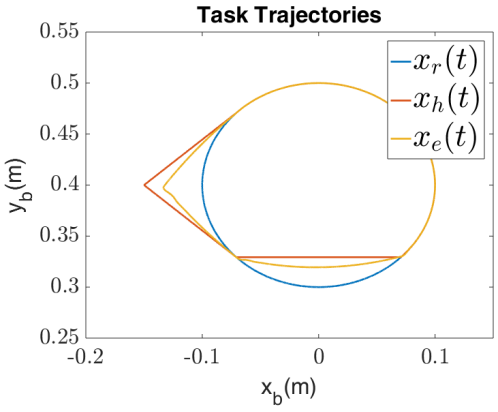

(a) Trajectories on the plane

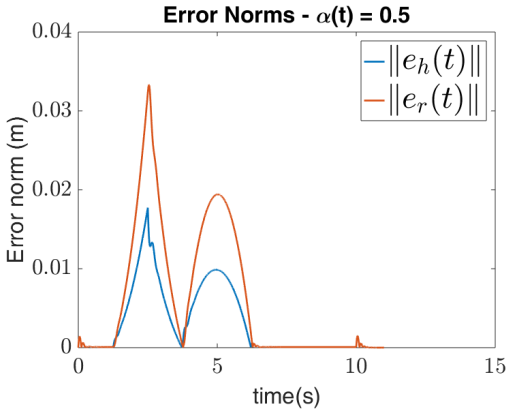

(b) Norm of the errors associated with the robot and human desired Trajectories

Figure 5.6: EEF position for $\alpha = 0.5$

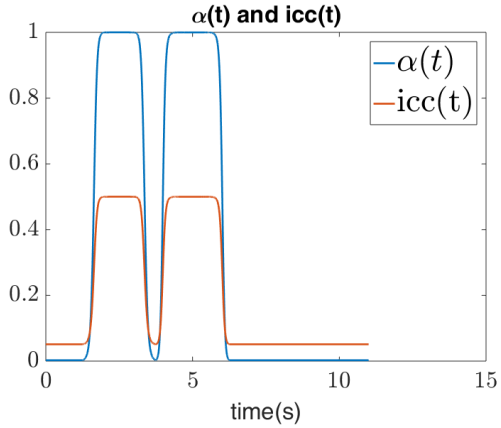

Figure 5.7: Variation of $\alpha(t), icc(t)$ during the adaptive alpha simulation

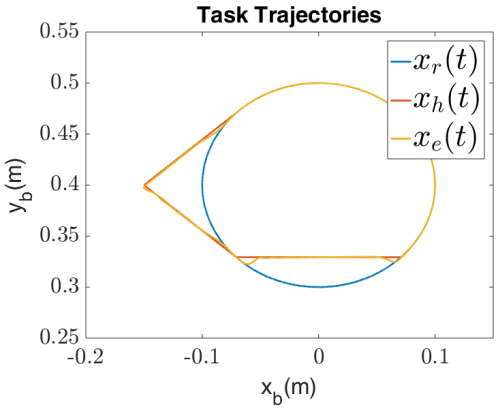

(a) Trajectories on the plane

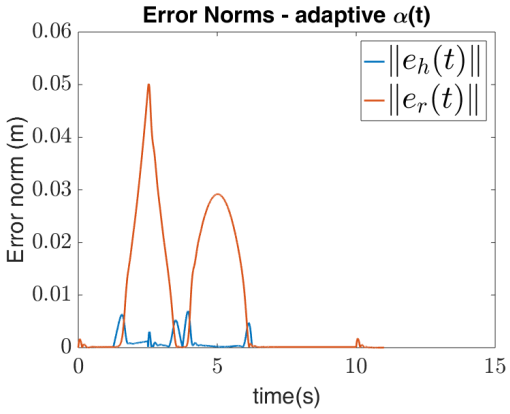

(b) Norm of the errors associated with the robot and human desired Trajectories

Figure 5.8: EEF position for adaptive α with varying stiffness

When α is adaptive, the $icc(t)$ signal also has to be simulated. For that matter, a sigmoid function that depends on $||e_h(t)||$ is used:

$$icc(t) = \frac{(icc_{MAX} - icc_{min})}{1 + exp(-(600\,||e_h(t)||) - 6)} + icc_{min} \tag{5.34}$$

It is noted, however, that this model is used here solely for the purpose of verifying the feasibility of the proposed admittance controller for dyadic HR co-manipulation.

When varying only the stiffness (5.10), in fig. 5.7, we can see the activation of the $icc(t)$ signal, and its correspondence to the role factor $\alpha(t)$. While the $icc(t)$ is smoothly being activated, the robot EEF smoothly moves from robot desired trajectory to human desired trajectory (fig. 5.8).

Then, it is verified that the condition for global asymptotic stability (5.22) is also met by looking at fig. 5.9. Note that only k_y is plotted, since $k_x = k_y$ for this simulation.

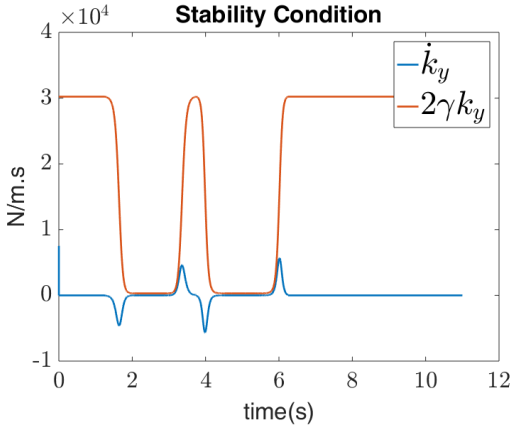

Figure 5.9: Stability condition during adaptive α simulation with varying stiffness

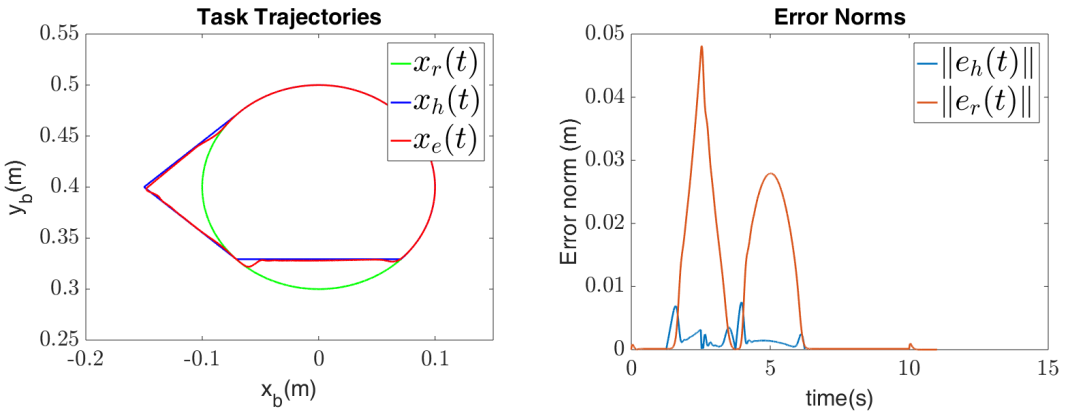

(a) Trajectories on the plane

(b) Norm of the errors associated with the robot and human desired Trajectories

Figure 5.10: EEF position for adaptive α with varying stiffness and damping

In the simulation shown in fig. 5.8, since the role factor $\alpha(t)$ depends on the human desired trajectory there is a larger error when the robot leaves the point p_3 until the $\alpha(t)$ smoothly reaches the full activation, but in spite of that, the stability conditions are still met in great part due to the smooth adaptation of the role factor.

- Adaptive α with varying stiffness and damping profiles:

For the varying stiffness and damping profile that uses (5.10), and (5.11), the stiffness profile is modified in order to comply with the stability condition (5.25), *i.e.*:

$$K_d = \begin{bmatrix} k_x & 0 \\ 0 & k_y \end{bmatrix} = 1000 I_2 (1 - \alpha(t)) + 100 I_2 \tag{5.35}$$

and since the damping profile is the critical damping, the constant damping ratio will be $\zeta = 1, \forall \alpha$. In addition, the desired inertia is the same as in (5.31).

When varying both the stiffness (5.10), and damping (5.11), in order to maintain the damping ratio $\zeta = 1$, the robot trajectory (fig. 5.10a) is similar to the trajectory

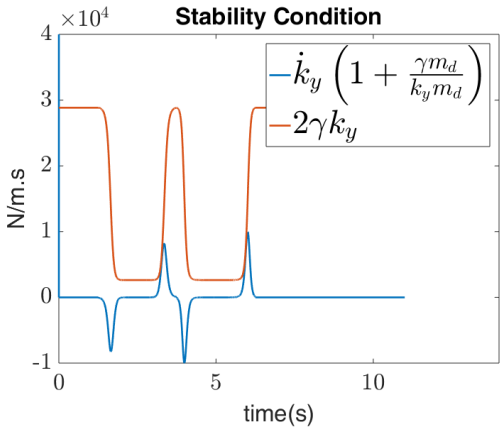

Figure 5.11: Stability condition during adaptive α with varying stiffness and damping

when the desired damping is fixed. However, it is possible to see a slight increase in the error norms when the human and robot desired trajectories diverge (fig. 5.10b). The stability condition (5.25) is also verified graphically in the fig. 5.11.

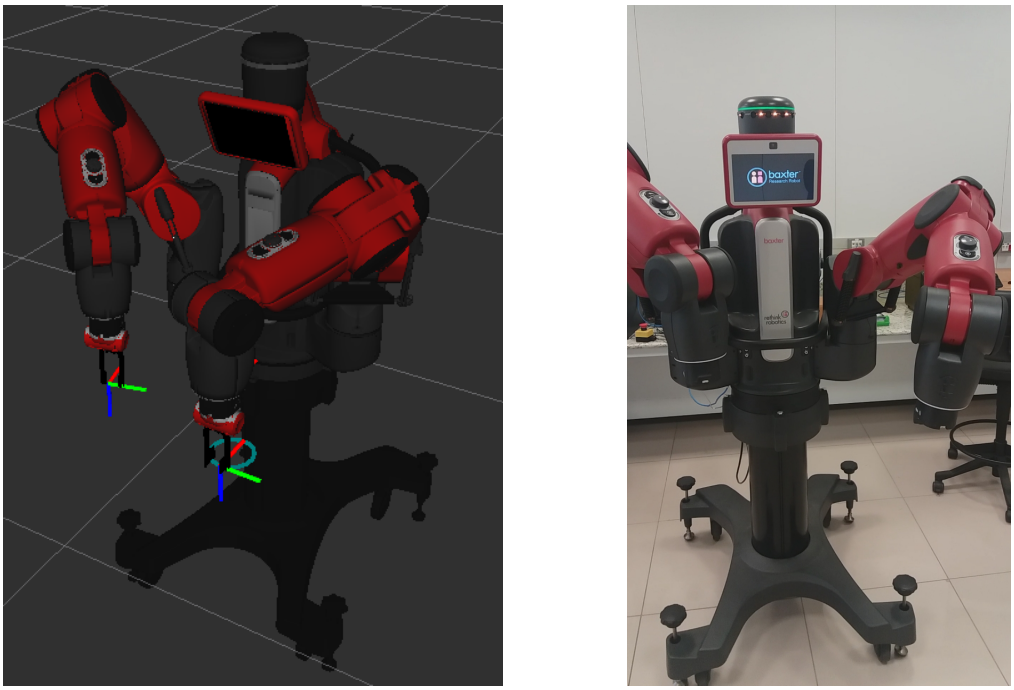

(a) Robot being simulated in ROS/Gazebo (b) Real robot

Figure 5.12: Baxter robot

5.4.2 Baxter Robot

To further evaluate the variation stiffness profile proposed by (5.10), a similar simulation to the one in the previous section is done, but now with the Baxter robot (Rethink Robotics) in the manufacturer's simulation environment that also takes into account the Baxter robot dynamics (5.7). In addition, an experiment with the real robot with virtual human forces is also executed.

Baxter Description

The Baxter robot has 7 DoF per arm. Each arm has torque, velocity, and position sensors for each joint. In this work, only the left arm of the robot is used. Furthermore, the manufacturer provides software for the robot simulation (fig. 5.12) alongside the open-source Robot Operating System (ROS) (Quigley *et al.*, 2009), and the physics simulator Gazebo (Koenig and Howard, 2004).

5.4.3 Desired Trajectories

For this simulation, the desired trajectories are redefined so that the kinematic controller (5.13) does not require to get close to the Baxter singularity configurations,

or to its joint limits, *i.e.*:

$$x_r(t) = \begin{bmatrix} 0.7 + 0.05\cos(\omega_0 t) \\ 0.25 + 0.05\sin(\omega_0 t) \\ 0.15 \end{bmatrix} \tag{5.36}$$

where $\omega_0 = \frac{2\pi}{30}$, and the robot trajectory period is 30 s. Meanwhile, the human desired trajectory is given by:

$$x_h(t) = \begin{cases} x_r(t), \quad t < 3.75 \\ (t - 3.75)\frac{p_2 - p_1}{3.75} + p_1, \quad 3.75 \leq t < 7.5 \\ (t - 7.5)\frac{p_3 - p_2}{3.75} + p_2, \quad 7.5 \leq t < 11.25 \\ (t - 11.25)\frac{p_4 - p_3}{7.5} + p_3, \quad 11.25 \leq t < 18.75 \\ x_r(t), \quad 18.75 \leq t < 30 \end{cases} \tag{5.37}$$

where $p_1 = x_r(3.75)$, $p_2 = [0.7; 0.325; 0.15]^\top$, $p_3 = x_r(11.25)$, and $p_4 = x_r(18.75)$ are fixed reference points. And as in the last simulation the human trajectory ends at the same time as the robot trajectory.

5.4.4 ICC simulation

Since the desired trajectories are redefined, the ICC definition is also redefined to produce high levels of activation in the appropriate periods of time:

$$icc(t) = \frac{(icc_{MAX} - icc_{min})}{1 + exp(-(2000\,||e_h(t)||) - 6)} + icc_{min} \tag{5.38}$$

5.4.5 Simulation Parameters

The Kinematic control parameter is given by $K_p = 50I_3$.

The maximum human stiffness is $K_{h0} = 400I_3$, which is also within the limits of human arm stiffness values in table 5.2.

5.4.6 Varying Stiffness Profile

For the varying stiffness profile, the desired admittance parameters are initially defined as: $\Lambda_d = 6I_3$; $D_d = 200I_3$; $K_{d0} = 800I_3$; $K_{d1} = 10I_3$. These parameters lead to the desired damping ratio varying from $\zeta = 1.48$ ($\alpha = 0$) to $\zeta = 12.91$ ($\alpha = 1$). Therefore, with this choice of D_d the desired impedance is overdamped for the entire simulation. In another simulation, the damping is fixed at $D_d = 139.43$ in order for

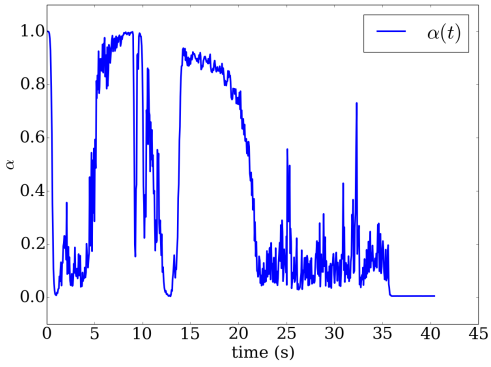

(a) Role factor variation with $D_d = 200I_2$

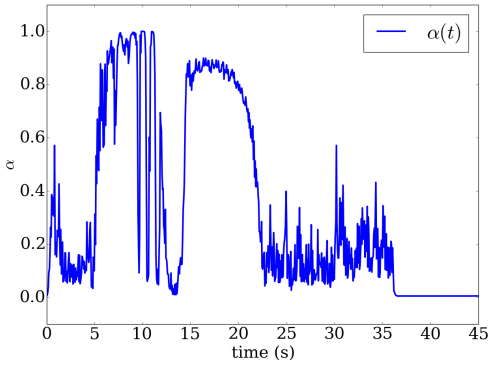

(b) Role factor variation with $D_d = 139.43I_2$

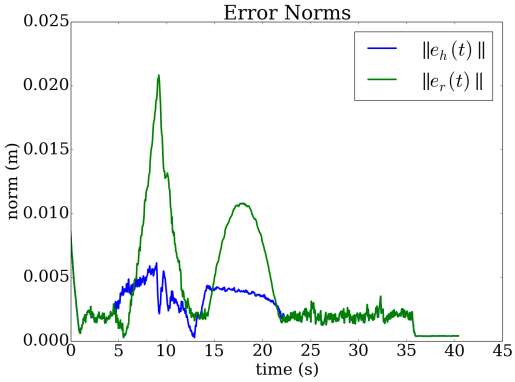

(c) Human, and robot position error norms with $D_d = 200I_2$

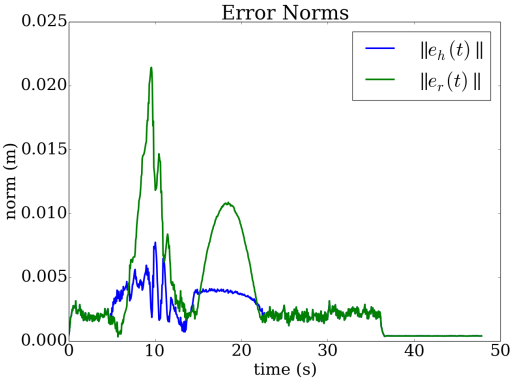

(d) Human, and robot position error norms with $D_d = 139.43I_2$

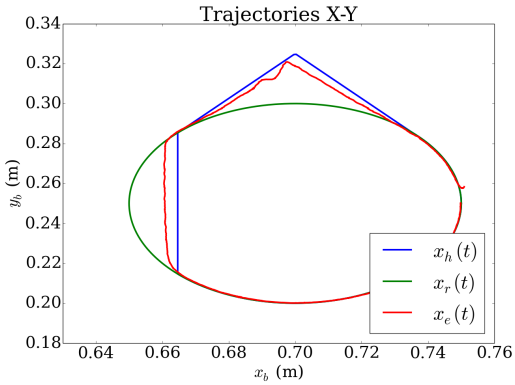

(e) Trajectories with $D_d = 200I_2$.

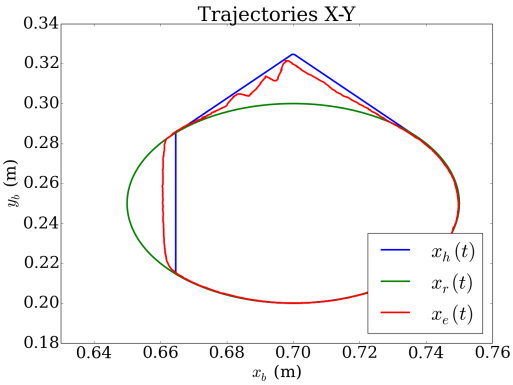

(f) Trajectories with $D_d = 139.43I_2$.

Figure 5.13: HR simulation with Baxter robot with varying stiffness profile and fixed damping

the desired impedance to have $\zeta = 1$ when $\alpha = 0$. For this configuration, $\zeta = 9$ when $\alpha = 1$.

The role factor variation in time is not smooth (fig. 5.13a, and 5.13b), as both simulations suffer from noise throughout the entire execution inside Gazebo which takes into account the robot dynamic equation of motion. This causes some noise in the human desired trajectory tracking, but most of all, the human desired trajectory

error, e_h, (5.13c, and 5.13d) shows that when x_h, and x_r diverge, x_e does not track x_h at any period of time (fig. 5.13e and 5.13f).

5.4.7 Varying Stiffness and Damping Profiles

For the varying stiffness and damping profile the desired admittance parameters are $\Lambda_d = 6I_3$; $K_{d0} = 800I_3$; $K_{d1} = 10I_3$, and the damping is given by :

$$D_d = 3\sqrt{k_y m_d} \tag{5.39}$$

which guarantees the overdamped desired damping ratio $\zeta = 1.5$ throughout the simulation.

In this simulation, the role factor variation is once again not smooth (fig. 5.14a), and it is similar to the variation from the last section. However, with the varying desired critical damping, more accentuated oscillations appeared both in the error norms (fig. 5.10b), and in the robot trajectory (fig. 5.14c).

5.4.8 Robot Experiment with Virtual Force

This time, a real Baxter robot is used instead of a simulation inside Gazebo. However, a virtual human force is still used. The kinematic controller parameter is now set as $K_p = 2000$; the human stiffness parameter $K_{h0} = 250$ while the desired admittance parameters are initially defined as: $\Lambda_d = 6I_3$; $D_d = 200I_3$; $K_{d0} = 800I_3$; $K_{d1} = 100I_3$, and result in a ζ variation from $\zeta = 1.44$ to $\zeta = 4.08$, therefore, always a desired overdamped impedance (to decrease oscillations). In the first experiment, only the desired varying stiffness is used (fig. 5.15e), this results in a similar behavior to the one from fig. 5.13e.

For the second experiment the varying stiffness and damping profile is used, in which the desired damping is defined here as:

$$D_d = 3\sqrt{k_y m_d} \tag{5.40}$$

Note, that this time, the varying desired damping results in an overdamped, instead of a critical ζ, to try to decrease oscillations further at the EEF. However, in order to obtain fewer oscillations (fig. 5.15f), the stiffness for $\alpha = 1$ had to be increased to $K_{d1} = 200$.

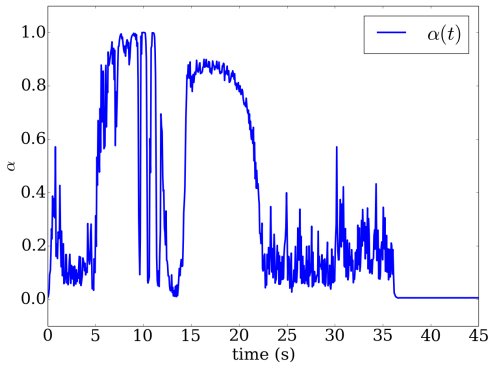

(a) Role factor variation

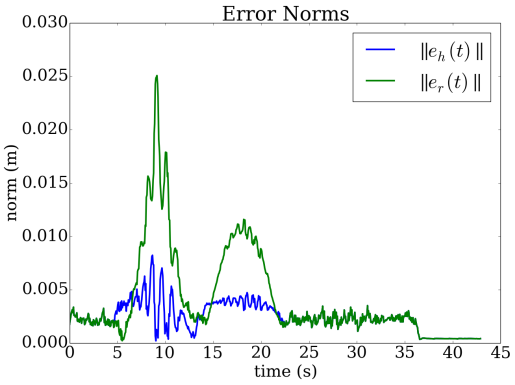

(b) Human, and robot position error norms

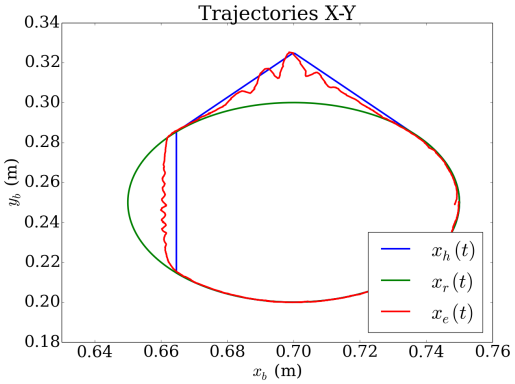

(c) Trajectories

Figure 5.14: HR simulation with Baxter robot with varying stiffness and damping profiles

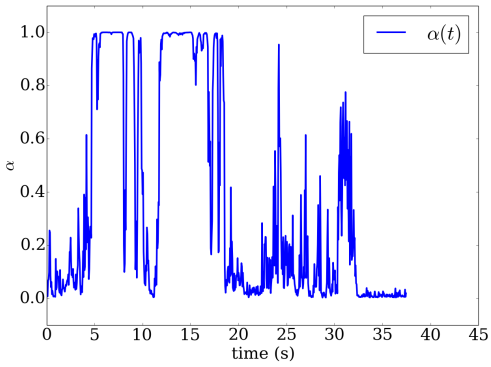

(a) α with fixed D_d

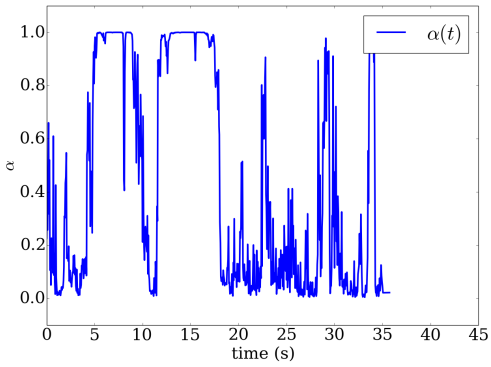

(b) α with varying D_d

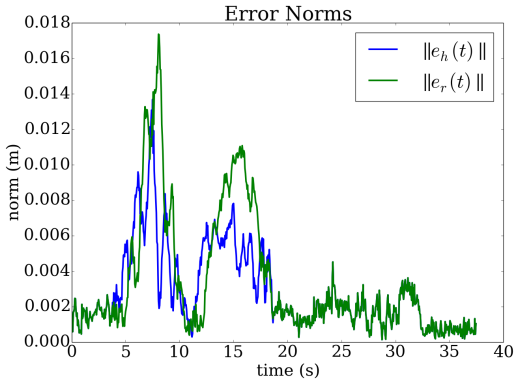

(c) Error norms with fixed D_d

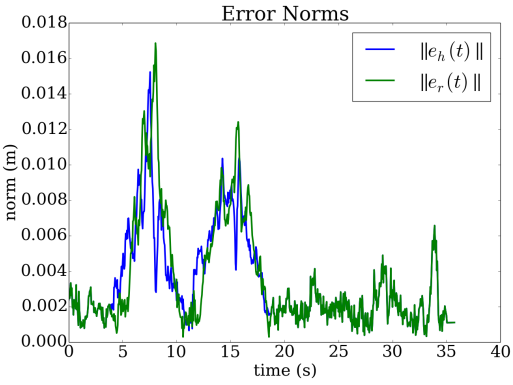

(d) Error norms with varying D_d

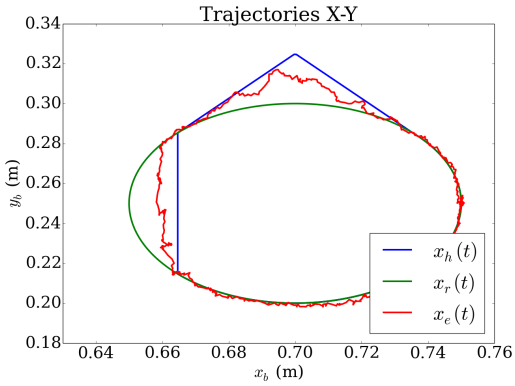

(e) Trajectory with fixed D_d

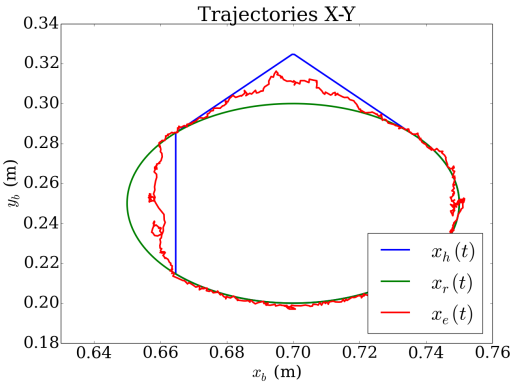

(f) Trajectory with varying D_d

Figure 5.15: Baxter experiment results

5.4.9 Discussion

The simulation results for the planar 3R robot behavior as a total leader or follower ($\alpha = 0$, or $\alpha = 1$), the norm of the human error, e_h, and of the robot error e_r were correctly predicted by the eq.'s (5.19) and (5.20). Furthermore, the mid value of $\alpha = 0.5$ also generated an object trajectory that was in between x_r and x_h. Those results corroborate that the proposed controller is not only able to assign roles by just varying the desired stiffness, but it is also able to generate similar trajectory patterns as seen on the HH dyads acting naturally in the dyad experiment of chapter 4.

Furthermore, in the simulations with fixed desired damping there is a variation of the damping ratio ζ, in such a way that the desired impedance goes from underdamped to overdamped with the variation of α. This can generate acceptable results (as shown in the simulations) even if oscillations appear when the robot is a follower, because the human stiffness increases when oscillations appear, and this is exactly one of the situations in which the robot should start behaving as a follower which for this case implies the overdamped desired impedance, resulting in less oscillations.

In the simulation with an online adaptation of $\alpha(t)$, other issues came to light when α was transitioning from total leader to total follower and vice-versa. The control strategy may present problems for the stability conditions depending on how quickly the human deactivates the role factor $\alpha(t)$. This is a concern especially when the human and robot desired trajectories overlap in just a few points in a neighborhood, like around the point p_3 in fig. 5.8, where both trajectories overlapped only at p_3.

In a real HR dyadic co-manipulation the human agent could have suddenly decreased his/her ICC in order to better track its own desired trajectory, which would have resulted in very high values for $\dot{k}_y$, and possibly created instability for the system. On the other hand, sudden ICC increases would quickly decrease the robot stiffness, which would not generate instability according to (5.22), and would quickly give the task leadership to the human agent.

Moreover, both impedance profiles, varying stiffness; and varying stiffness and damping profiles, once they are validated by the stability conditions, they show very similar trajectory results, even though in the latter case $\zeta = 1$ and the desired damping is critical.

The simulation executed with the Baxter robot in the Gazebo physics engine, presented noisy values of α due to its definition based on the norm of e_h (5.38). Because of the noisy α, the robot never constantly reached the role of total follower, therefore, whenever x_r, and x_h diverged, e_h was never null. Furthermore, The noisy

α also implies that theorem 1 can not be applied, as the smoothness of the time-varying stiffness profile is a requisite. In spite of the noisy role adaptation, the overdamped desired impedance was able to reduce the number of oscillations when D_d was fixed (fig. 5.13). However, when D_d was a function of the critical damping (fig. 5.14), the damping would decrease enough to produce oscillations as α started approaching the total follower behavior.

In the real robot experiment with virtual human force, the kinematic controller parameter K_p had to be increased in order for the robot to properly track the desired trajectories from the admittance control. The trajectory execution was not as good as in the previous simulations, but it was well within the 5 mm precision advertised by the robot manufacturer.

For the robot experiment, both the fixed damping and varying damping profiles resulted in similar trajectories to the one in fig. 5.13. Note that for the varying damping profile this was only possible due to the increase in the minimum value of stiffness, K_{d1}. This strategy is exactly the same as the one validated by the stability conditions in the planar 3R robot simulation.

5.5 Conclusions

The admittance controller proposed in this chapter provides a way to continuously change the desired stiffness at the robot EEF while maintaining stability conditions given a smooth variation in a scalar role factor. The change in desired stiffness affects the robot trajectory, and effectively interpolates the robot desired trajectory and the human desired trajectory, providing leadership of the task to the human or the robot. However, this control strategy depends highly on the choice of the role factor α adaptation to have more efficient role switching, and therefore, better human desired trajectory tracking.

In addition, as it was verified in the Baxter robot simulations and experiment, noisy values of α that cause noisy stiffness adaptation and thus noisy trajectories can be compensated by increasing the desired apparent inertia and desired damping matrices (Dimeas and Aspragathos, 2016).

Chapter 6

Discussion and Conclusions

6.1 Summary

In recent years, human-robot collaboration (HRC) has been a very active topic in the academic research community. This is mainly due to the fact that robots and humans may generally provide complementary skills to task execution. The robots may provide high power generation, and excellence at repetitive tasks, while the humans may provide learning capabilities and superior environment awareness.

When designing a HRC, the most important aspects are related to the robot's human partner: His/her comfort; ergonomic aspects of the task; how the robot and the human intercommunicate; and most importantly, the safety of the human partner. With those aspects in mind, the focus of this work was to develop a robot controller that would enable a robot not only to follow, but also to lead the co-manipulation of a shared object alongside its human partner. But in order to design such a controller, it was necessary to know exactly what are the requisites for a human-robot (HR) dyadic co-manipulation. To solve this issue, the approach used in this work was to study how a human-human (HH) dyad behaves in the face of different leadership assignments for each human partner, and then apply the knowledge obtained to propose a novel controller.

The study done on humans consisted of two experiments, one where a HH dyad co-manipulates an object around obstacles, and another where a single participant does the same. Surface EMG sensors were used along with a motion capture system, and custom contact sensors to provide data regarding the arm stiffness of the humans, the object trajectory and a performance criteria for both dyads and single participants.

The study on HH dyad behavior suggests that humans modulate their own arm endpoint stiffness in order to negotiate roles of leadership. The changes in the object trajectory are likely to be strongly related to the changes in the human agents'

stiffness. Moreover, the study also indicated that every agent in a certain position in a dyad has its own desired trajectory for the shared object, which it tries to track closely when assigned the role of a leader. The assumption that every agent has its own desired trajectory was further reinforced by the manipulation experiment with a single human. In addition to the stiffness/trajectory discussion, the performance criteria revealed that HH dyads performed better than single participants at executing the manipulation task, this a very important result that may imply that both humans in the HH dyad modulate their stiffness and trajectory while cooperatively optimizing for a better trajectory.

Experiments of this kind, with HH dyads and few position restrictions, to the best of the author's knowledge have not been extensively executed or analyzed, and possess a great potential not only to the human motor behavior community, but also to the robotics community.

The execution of those experiments presented many challenges, one of which was to develop software that could encapsulate all the necessary procedures for the use of surface EMG in a HRC. The developed software is now made available as open-source in `https://www.github.com/inria-larsen/emg-processing`. It is expected to be continuously improved in the future, and to be helpful for the academic community.

With the human motor behavior results in hand, a novel adaptive admittance controller was proposed. The controller aimed to emulate the same behavior of humans by modulating a desired robot stiffness in a HR dyad based on a single scalar role factor that depends on the human stiffness. The influence of the controller for different desired behaviors was predicted and validated through numerical simulations. Moreover, stability conditions for the desired stiffness variation were also found. The results from simulation are very promising since the effect on the object trajectory in the HH dyad experiment was observed in the HR simulation as well, especially the interpolations of desired trajectories for middle value stiffnesses.

The proposed controller, however, has some limitations. It expects the ICC signal from the human arm to be always smooth, which may not be the case in a real HR dyad experiment even if the ICC signal is processed in a more sophisticated form than it was processed in this work. And it also does not account for directional variations of stiffness, since when it changes the robot desired stiffness it always changes the stiffness in every direction.

6.2 Future Work Perspective

Despite the very good indications given by the HH dyad and the single human manipulation experiments, their results need to be further validated through a more

intricate statistical analysis. For this, more trials of each experiment may have to be done.

Furthermore, the HH co-manipulation experiment still has potential to offer more insight into the human natural behavior. In Sabes and Jordan (1997) for instance, the authors investigated the human planning for hand reaching movements while avoiding obstacles, and associated the hand trajectory with kinematic metrics like the velocity manipulability of the arm, and other metrics that took into account the inertia of the human arm. This type of study may be extended to HH dyads. One way of doing it would be to calculate the manipulability of the entire dyad after modeling them as a closed kinematic chain formed by two open chain manipulators, which are restricted by each other (Freitas *et al.*, 2011). Manipulability is of particular interest because it is associated with more comfort, and finer arm control for humans acting alone, and as partners in a HR dyad (Gopinathan *et al.*, 2017).

Another possibility already hinted in recent related works (Grafakos *et al.*, 2016; Peternel *et al.*, 2017) is to use the motion capture data alongside the ICC data for every human joint to obtain human arm endpoint stiffness in the operational space (for every direction). This study could even help to verify the findings from Mojtahedi *et al.* (2017) which state the existence of the haptic communication of motion intentions between humans during a co-manipulation task through the directional modulation of stiffness.

This could result in a readily augmentation of the proposed admittance controller, that could then feature a directional stiffness adaptation to both improve the desired trajectory tracking, and to communicate the robot intention of motion (legibility) more effectively to the human agent, hopefully improving the intuitiveness of the task as well. Furthermore, as presented in chapter 1, a secondary goal such as maximization of velocity manipulability, may be used in the internal kinematic controller of the admittance controller proposed here. It is also possible to control the robot with a quadratic program (QP) (Bouyarmane and Kheddar, 2011) or other optimization based controller (Spyrakos-Papastavridis *et al.*, 2018) in order to optimize for many different restrictions, and secondary goals, like the decoupling of apparent inertia in Ficuciello *et al.* (2015), while maintaining a desired admittance behavior.

Many control problems and design requirements are formulated with linear matrix inequalities (LMI) in such a way that the control problem may be solved by optimization techniques (Boyd *et al.*, 1994). Since the stability conditions in (5.21) and (5.22) also form a LMI, instead of defining desired impedance terms by trial and error, it could be possible to apply LMI solving techniques in order to obtain the desired impedance terms for the admittance controller.

The natural next step into the advance of the role factor adaptive admittance

controller is to test it in a real HR experiment. This has the potential to showcase issues, and suggest straightforward ideas for further development of the controller.

In addition, it is worth mentioning that the approach used here was to build a solid fundamental block with novel human motor behavior knowledge in which a new robot controller could be efficiently developed. Naturally, the more is known about the HH dyad behavior, the more control goals may be included in the robot control strategy. But this is not necessarily a one way direction. The results from controllers that mimic human motor behavior can be used to simulate human motor control and learning, which has the potential to help understanding human motor behavior as well. This is what Yang *et al.* (2011) called a virtuous human–machine motor learning cycle.

Bibliography

2006, *ISO 10218-1:2011 Robot for industrial environments - Safety requirements - Part 1 : Robot.* Technical report, International Organization for Standardization, Geneva, Switzerland.

Agravante, D. J., Cherubini, A., Bussy, A., et al., 2014, "Collaborative human-humanoid carrying using vision and haptic sensing". In: *2014 IEEE International Conference on Robotics and Automation (ICRA)*, pp. 607–612, May. doi: 10.1109/ICRA.2014.6906917.

Ahmadi-Pajouh, M. A., Towhidkhah, F., Moradi, M. H., 2012, "Estimation of time-varying human arm stiffness using electromyogram signal". In: *2012 19th Iranian Conference of Biomedical Engineering (ICBME)*, pp. 26–30, Dec. doi: 10.1109/ICBME.2012.6519654.

Ajoudani, A., Godfrey, S. B., Bianchi, M., et al., 2014, "Exploring Teleimpedance and Tactile Feedback for Intuitive Control of the Pisa/IIT SoftHand", *IEEE Transactions on Haptics*, v. 7, n. 2 (April), pp. 203–215. ISSN: 1939-1412. doi: 10.1109/TOH.2014.2309142.

Ajoudani, A., Fang, C., Tsagarakis, N. G., et al., 2015, "A reduced-complexity description of arm endpoint stiffness with applications to teleimpedance control". In: *2015 IEEE/RSJ International Conference on Intelligent Robots and Systems (IROS)*, pp. 1017–1023, Sept. doi: 10.1109/IROS.2015.7353495.

Ajoudani, A., Tsagarakis, N. G., Bicchi, A., 2017a, "Choosing Poses for Force and Stiffness Control", *IEEE Transactions on Robotics*, v. 33, n. 6 (Dec), pp. 1483–1490. ISSN: 1552-3098. doi: 10.1109/TRO.2017.2708087.

Ajoudani, A., Zanchettin, A. M., Ivaldi, S., et al., 2017b, "Progress and prospects of the human–robot collaboration", *Autonomous Robots*, (Oct). ISSN: 1573-7527. doi: 10.1007/s10514-017-9677-2.

Bandyopadhyay, T., Won, K. S., Frazzoli, E., et al., 2013, "Intention-Aware Motion Planning". In: *Algorithmic Foundations of Robotics X: Proceedings of the*

Tenth Workshop on the Algorithmic Foundations of Robotics, pp. 475–491, Berlin, Heidelberg, Springer Berlin Heidelberg. ISBN: 978-3-642-36279-8. doi: 10.1007/978-3-642-36279-8_29.

Basmajian, J., De Luca, C., 1985, *Muscles Alive: Their Functions Revealed by Electromyography*. Williams & Wilkins. ISBN: 9780683004144.

Bauer, A., Wollherr, D., Buss, M., 2008, "Human–Robot Collaboration: A Survey", *International Journal of Humanoid Robotics*, v. 05, n. 01, pp. 47–66. doi: 10.1142/S0219843608001303.

Bestick, A. M., Burden, S. A., Willits, G., et al., 2015, "Personalized kinematics for human-robot collaborative manipulation". In: *2015 IEEE/RSJ International Conference on Intelligent Robots and Systems (IROS)*, pp. 1037–1044, Sept. doi: 10.1109/IROS.2015.7353498.

Beton, L., Hughes, P., Barker, S., et al., 2017, "Leader-Follower Strategies for Robot-Human Collaboration". In: Aldinhas Ferreira, M. I., Silva Sequeira, J., Tokhi, M. O., et al. (Eds.), *A World with Robots: International Conference on Robot Ethics: ICRE 2015*, pp. 145–158, Cham, Springer International Publishing. ISBN: 978-3-319-46667-5. doi: 10.1007/978-3-319-46667-5_11.

Bicchi, A., Tonietti, G., Bavaro, M., et al., 2005, "Variable Stiffness Actuators for Fast and Safe Motion Control". In: Dario, P., Chatila, R. (Eds.), *Robotics Research. The Eleventh International Symposium: With 303 Figures*, pp. 527–536, Berlin, Heidelberg, Springer Berlin Heidelberg. ISBN: 978-3-540-31508-7. doi: 10.1007/11008941_56.

Bó, A. P. L., Poignet, P., 2010, "Tremor attenuation using FES-based joint stiffness control". In: *2010 IEEE International Conference on Robotics and Automation*, pp. 2928–2933, May. doi: 10.1109/ROBOT.2010.5509560.

Bó, A. P. L., Poignet, P., Zhang, D., et al., 2009, "FES-controlled co-contraction strategies for pathological tremor compensation". In: *2009 IEEE/RSJ International Conference on Intelligent Robots and Systems*, pp. 1633–1638, Oct. doi: 10.1109/IROS.2009.5354397.

Bouyarmane, K., Kheddar, A., 2011, "Using a multi-objective controller to synthesize simulated humanoid robot motion with changing contact configurations". In: *2011 IEEE/RSJ International Conference on Intelligent Robots and Systems*, pp. 4414–4419, Sept. doi: 10.1109/IROS.2011.6094483.

Boyd, S., El Ghaoui, L., Feron, E., et al., 1994, *Linear Matrix Inequalities in System and Control Theory*, v. 15, *Studies in Applied Mathematics*. Philadelphia, PA, SIAM. ISBN: 0-89871-334-X.

Burdet, E., Osu, R., Franklin, D. W., et al., 2001, "The central nervous system stabilizes unstable dynamics by learning optimal impedance", *Nature*, v. 414 (Nov).

Busch, B., Maeda, G., Mollard, Y., et al., 2017, "Postural Optimization for an Ergonomic Human-Robot Interaction". In: *IROS 2017 - IEEE/RSJ International Conference on Intelligent Robots and Systems*, pp. 1–8, Vancouver, Canada, sep.

Campeau-Lecours, A., Otis, M. J.-D., Gosselin, C., 2016, "Modeling of physical human–robot interaction: Admittance controllers applied to intelligent assist devices with large payload", *International Journal of Advanced Robotic Systems*, v. 13, n. 5, pp. 1729881416658167. doi: 10.1177/1729881416658167.

Cherubini, A., Passama, R., Crosnier, A., et al., 2016, "Collaborative manufacturing with physical human-robot interaction", *Robotics and Computer-Integrated Manufacturing*, v. 40, pp. 1 – 13. ISSN: 0736-5845. doi: https://doi.org/10.1016/j.rcim.2015.12.007.

Colgate, J. E., Peshkin, M., Klostermeyer, S. H., 2003, "Intelligent assist devices in industrial applications: a review". In: *Proceedings 2003 IEEE/RSJ International Conference on Intelligent Robots and Systems (IROS 2003) (Cat. No.03CH37453)*, v. 3, pp. 2516–2521 vol.3, Oct. doi: 10.1109/IROS.2003.1249248.

Colgate, J., Wannasuphoprasit, W., Peshkin, M., 1996, "Cobots: robots for collaboration with human operators". In: Kwon, Y., Davis, D., Chung, H. (Eds.), *Proceedings of the ASME Dynamic Systems and Control Division*, v. 58, pp. 433–439, ASME.

Corke, P., 2011, *Robotics, Vision and Control: Fundamental Algorithms in MATLAB*. Springer Tracts in Advanced Robotics. Springer Berlin Heidelberg. ISBN: 9783642201431.

Darainy, M., Ostry, D. J., 2008, "Muscle cocontraction following dynamics learning", *Experimental Brain Research*, v. 190, n. 2 (Sep), pp. 153–163. ISSN: 1432-1106. doi: 10.1007/s00221-008-1457-y.

De Serres, S. J., Milner, T. E., 1991, "Wrist muscle activation patterns and stiffness associated with stable and unstable mechanical loads", *Experimental Brain Research*, v. 86, n. 2 (Sep), pp. 451–458. ISSN: 1432-1106. doi: 10.1007/BF00228972. Available at: <https://doi.org/10.1007/BF00228972>.

Dermy, O., Paraschos, A., Ewerton, M., et al., 2017, "Prediction of Intention during Interaction with iCub with Probabilistic Movement Primitives", *Frontiers in Robotics and AI*, v. 4, pp. 45. ISSN: 2296-9144. doi: 10.3389/frobt.2017.00045.

Dimeas, F., Aspragathos, N., 2016, "Online Stability in Human-Robot Cooperation with Admittance Control", *IEEE Transactions on Haptics*, v. 9, n. 2 (April), pp. 267–278. ISSN: 1939-1412. doi: 10.1109/TOH.2016.2518670.

Dollar, A. M., Herr, H., 2008, "Lower Extremity Exoskeletons and Active Orthoses: Challenges and State-of-the-Art", *IEEE Transactions on Robotics*, v. 24, n. 1 (Feb), pp. 144–158. ISSN: 1552-3098. doi: 10.1109/TRO.2008.915453.

Dragan, A. D., Lee, K. C. T., Srinivasa, S. S., 2013, "Legibility and predictability of robot motion". In: *2013 8th ACM/IEEE International Conference on Human-Robot Interaction (HRI)*, pp. 301–308, March. doi: 10.1109/HRI.2013.6483603.

Dragan, A. D., Bauman, S., Forlizzi, J., et al., 2015, "Effects of Robot Motion on Human-Robot Collaboration". In: *Proceedings of the Tenth Annual ACM/IEEE International Conference on Human-Robot Interaction*, HRI '15, pp. 51–58, New York, NY, USA. ACM. ISBN: 978-1-4503-2883-8. doi: 10.1145/2696454.2696473.

Duchaine, V., Gosselin, C. M., 2007, "General Model of Human-Robot Cooperation Using a Novel Velocity Based Variable Impedance Control". In: *Second Joint EuroHaptics Conference and Symposium on Haptic Interfaces for Virtual Environment and Teleoperator Systems (WHC'07)*, pp. 446–451, March. doi: 10.1109/WHC.2007.59.

Duchaine, V., Gosselin, C. M., 2008, "Investigation of human-robot interaction stability using Lyapunov theory". In: *2008 IEEE International Conference on Robotics and Automation*, pp. 2189–2194, May. doi: 10.1109/ROBOT.2008.4543531.

Dumora, J., Geffard, F., Bidard, C., et al., 2012, "Experimental study on haptic communication of a human in a shared human-robot collaborative task".

In: *2012 IEEE/RSJ International Conference on Intelligent Robots and Systems*, pp. 5137–5144, Oct. doi: 10.1109/IROS.2012.6385721.

Enayati, N., Momi, E. D., Ferrigno, G., 2016, "Haptics in Robot-Assisted Surgery: Challenges and Benefits", *IEEE Reviews in Biomedical Engineering*, v. 9, pp. 49–65. ISSN: 1937-3333. doi: 10.1109/RBME.2016.2538080.

Evrard, P., Kheddar, A., 2009a, "Homotopy switching model for dyad haptic interaction in physical collaborative tasks". In: *World Haptics 2009 - Third Joint EuroHaptics conference and Symposium on Haptic Interfaces for Virtual Environment and Teleoperator Systems*, pp. 45–50, Marcha. doi: 10.1109/WHC.2009.4810879.

Evrard, P., Kheddar, A., 2009b, "Homotopy-based controller for physical human-robot interaction". In: *RO-MAN 2009 - The 18th IEEE International Symposium on Robot and Human Interactive Communication*, pp. 1–6, Septb. doi: 10.1109/ROMAN.2009.5326065.

Evrard, P., Gribovskaya, E., Calinon, S., et al., 2009, "Teaching physical collaborative tasks: object-lifting case study with a humanoid". In: *2009 9th IEEE-RAS International Conference on Humanoid Robots*, pp. 399–404, Dec. doi: 10.1109/ICHR.2009.5379513.

Ficuciello, F., Romano, A., Villani, L., et al., 2014, "Cartesian impedance control of redundant manipulators for human-robot co-manipulation". In: *2014 IEEE/RSJ International Conference on Intelligent Robots and Systems*, pp. 2120–2125, Sept. doi: 10.1109/IROS.2014.6942847.

Ficuciello, F., Villani, L., Siciliano, B., 2015, "Variable Impedance Control of Redundant Manipulators for Intuitive Human-Robot Physical Interaction", *IEEE Transactions on Robotics*, v. 31, n. 4 (Aug), pp. 850–863. ISSN: 1552-3098. doi: 10.1109/TRO.2015.2430053.

Franklin, D. W., Liaw, G., Milner, T. E., et al., 2007, "Endpoint Stiffness of the Arm Is Directionally Tuned to Instability in the Environment", *Journal of Neuroscience*, v. 27, n. 29, pp. 7705–7716. ISSN: 0270-6474. doi: 10.1523/JNEUROSCI.0968-07.2007.

Franklin, D. W., Burdet, E., Peng Tee, K., et al., 2008, "CNS Learns Stable, Accurate, and Efficient Movements Using a Simple Algorithm", *Journal of Neuroscience*, v. 28, n. 44, pp. 11165–11173. ISSN: 0270-6474. doi: 10.1523/JNEUROSCI.3099-08.2008.

Freitas, G. M., Leite, A. C., Lizarralde, F., 2011, "Kinematic control of constrained robotic systems", *Sba: Controle e Automacao. Sociedade Brasileira de Automatica*, v. 22 (12), pp. 559 – 572. ISSN: 0103-1759. Available at: <http://www.scielo.br/scielo.php?script=sci_arttext&pid=S0103-17592011000600002&nrm=iso>.

Fryman, J., Matthias, B., 2012, "Safety of Industrial Robots: From Conventional to Collaborative Applications". In: *ROBOTIK 2012; 7th German Conference on Robotics*, pp. 1–5, May.

Gallagher, W., Gao, D., Ueda, J., 2014, "Improved stability of haptic human–robot interfaces using measurement of human arm stiffness", *Advanced Robotics*, v. 28, n. 13, pp. 869–882. doi: 10.1080/01691864.2014.900162.

Gardner-Morse, M. G., Stokes, I. A., 2001, "Trunk stiffness increases with steady-state effort", *Journal of Biomechanics*, v. 34, n. 4, pp. 457 – 463. ISSN: 0021-9290. doi: https://doi.org/10.1016/S0021-9290(00)00226-8. Available at: <http://www.sciencedirect.com/science/article/pii/S0021929000002268>.

Gopinathan, S., Oetting, S. K., Steil, J. J., 2017, "A User Study on Personalized Stiffness Control and Task Specificity in Physical Human–Robot Interaction", *Frontiers in Robotics and AI*, v. 4, pp. 58. ISSN: 2296-9144. doi: 10.3389/frobt.2017.00058.

Grafakos, S., Dimeas, F., Aspragathos, N., 2016, "Variable admittance control in pHRI using EMG-based arm muscles co-activation". In: *2016 IEEE International Conference on Systems, Man, and Cybernetics (SMC)*, pp. 001900–001905, Oct. doi: 10.1109/SMC.2016.7844516.

Gribovskaya, E., Kheddar, A., Billard, A., 2011, "Motion learning and adaptive impedance for robot control during physical interaction with humans". In: *2011 IEEE International Conference on Robotics and Automation*, pp. 4326–4332, May. doi: 10.1109/ICRA.2011.5980070.

Hoeckelmann, M., Rudas, I. J., Fiorini, P., et al., 2015, "Current Capabilities and Development Potential in Surgical Robotics", *International Journal of Advanced Robotic Systems*, v. 12, n. 5, pp. 61. doi: 10.5772/60133. Available at: <https://doi.org/10.5772/60133>.

Hogan, N., 1984, "Adaptive control of mechanical impedance by coactivation of antagonist muscles", *IEEE Transactions on Automatic Control*, v. 29, n. 8 (Aug), pp. 681–690. ISSN: 0018-9286. doi: 10.1109/TAC.1984.1103644.

Jarrassé, N., Sanguineti, V., Burdet, E., 2014, "Slaves no longer: review on role assignment for human–robot joint motor action", *Adaptive Behavior*, v. 22, n. 1, pp. 70–82. doi: 10.1177/1059712313481044.

Kazerooni, H., Racine, J. L., Huang, L., et al., 2005, "On the Control of the Berkeley Lower Extremity Exoskeleton (BLEEX)". In: *Proceedings of the 2005 IEEE International Conference on Robotics and Automation*, pp. 4353–4360, April. doi: 10.1109/ROBOT.2005.1570790.

Khalil, H., 2002, *Nonlinear Systems*. Pearson Education. Prentice Hall. ISBN: 9780130673893.

Klingspor, V., Demiris, J., Kaiser, M., 1997, "Human-robot-communication and machine learning", *Applied Artificial Intelligence Journal*, v. 11, n. 11, pp. 719–746.

Koenig, N., Howard, A., 2004, "Design and Use Paradigms for Gazebo, An Open-Source Multi-Robot Simulator". In: *IEEE/RSJ International Conference on Intelligent Robots and Systems*, pp. 2149–2154, Sendai, Japan, Sep.

Konrad, P., 2005, "The ABC of EMG - A Practical Introduction to Kinesiological Electromyography". Available at: <`https://www.noraxon.com/wp-content/uploads/2014/12/ABC-EMG-ISBN.pdf`>.

Kosuge, K., Hirata, Y., 2004, "Human-Robot Interaction". In: *2004 IEEE International Conference on Robotics and Biomimetics*, pp. 8–11, Aug. doi: 10.1109/ROBIO.2004.1521743.

Kronander, K., Billard, A., 2016, "Stability Considerations for Variable Impedance Control", *IEEE Transactions on Robotics*, v. 32, n. 5 (Oct), pp. 1298–1305. ISSN: 1552-3098. doi: 10.1109/TRO.2016.2593492.

Leite, A. C., 2005. "Controle Híbrido de Força e Visão de um Manipulador Robótico Sobre Superfícies Desconhecidas". Master Thesis in Portuguese.

Li, Y., Tee, K. P., Chan, W. L., et al., 2015a, "Continuous Role Adaptation for Human-Robot Shared Control", *IEEE Transactions on Robotics*, v. 31, n. 3 (June), pp. 672–681. ISSN: 1552-3098. doi: 10.1109/TRO.2015.2419873.

Li, Y., Tee, K. P., Liang Chan, W., et al., 2015b, "Role adaptation of human and robot in collaborative tasks", v. 2015 (06), pp. 5602–5607.

Li, Z., Huang, Z., He, W., et al., 2017, "Adaptive Impedance Control for an Upper Limb Robotic Exoskeleton Using Biological Signals", *IEEE Transactions on Industrial Electronics*, v. 64, n. 2 (Feb), pp. 1664–1674. ISSN: 0278-0046. doi: 10.1109/TIE.2016.2538741.

Luca, C. J. D., 2008. "Practicum on the Use of Surface EMG Signals in Movement Sciences (v1.5)". `https://www.delsys.com/KnowledgeCenter/Practicum.html`. Accessed: 20-02-2018.

Luca, C. J. D., 1997, "The Use of Surface Electromyography in Biomechanics", *Journal of Applied Biomechanics*, v. 13, n. 2, pp. 135–163. doi: 10.1123/jab.13.2.135.

Luca, C. J. D., Adam, A., Wotiz, R., et al., 2006, "Decomposition of Surface EMG Signals", *Journal of Neurophysiology*, v. 96, n. 3, pp. 1646–1657. doi: 10.1152/jn.00009.2006. PMID: 16899649.

M. Smith, A., 1981, "The coactivation of antagonist muscles", *Canadian journal of physiology and pharmacology*, v. 59 (08), pp. 733–47.

Matthias, B., Kock, S., Jerregard, H., et al., 2011, "Safety of collaborative industrial robots: Certification possibilities for a collaborative assembly robot concept". In: *2011 IEEE International Symposium on Assembly and Manufacturing (ISAM)*, pp. 1–6, May. doi: 10.1109/ISAM.2011.5942307.

Maurice, P., 2015, *Virtual ergonomics for the design of collaborative robots*. Theses, Université Pierre et Marie Curie - Paris VI, jun.

McIntyre, J., Mussa-Ivaldi, F. A., Bizzi, E., 1996, "The control of stable postures in the multijoint arm", *Experimental Brain Research*, v. 110, n. 2.

Melendez-Calderon, A., Komisar, V., Ganesh, G., et al., 2011, "Classification of strategies for disturbance attenuation in human-human collaborative tasks". In: *2011 Annual International Conference of the IEEE Engineering in Medicine and Biology Society*, pp. 2364–2367, Aug. doi: 10.1109/IEMBS.2011.6090660.

Michalos, G., Makris, S., Tsarouchi, P., et al., 2015, "Design Considerations for Safe Human-robot Collaborative Workplaces", *Procedia CIRP*, v. 37, n. Supplement C, pp. 248 – 253. ISSN: 2212-8271. doi: https://doi.org/10.1016/j.procir.2015.08.014. CIRPe 2015 - Understanding the life cycle implications of manufacturing.

Mojtahedi, K., Whitsell, B., Artemiadis, P., et al., 2017, "Communication and Inference of Intended Movement Direction during Human–Human Physical Interaction", *Frontiers in Neurorobotics*, v. 11, pp. 21. ISSN: 1662-5218. doi: 10.3389/fnbot.2017.00021.

Murray, R. M., Sastry, S. S., Zexiang, L., 1994, *A Mathematical Introduction to Robotic Manipulation*. 1st ed. Boca Raton, FL, USA, CRC Press, Inc. ISBN: 0849379814.

Murray, W. M., Delp, S. L., Buchanan, T. S., 1995, "Variation of muscle moment arms with elbow and forearm position", *Journal of Biomechanics*, v. 28, n. 5, pp. 513–525.

Mörtl, A., Lawitzky, M., Kucukyilmaz, A., et al., 2012, "The role of roles: Physical cooperation between humans and robots", *The International Journal of Robotics Research*, v. 31, n. 13, pp. 1656–1674. doi: 10.1177/0278364912455366.

Navarro, B., Cherubini, A., Fonte, A., et al., 2016, "An ISO10218-compliant adaptive damping controller for safe physical human-robot interaction". In: *2016 IEEE International Conference on Robotics and Automation (ICRA)*, pp. 3043–3048, May. doi: 10.1109/ICRA.2016.7487468.

Nielsen, J., Sinkjær, T., Toft, E., et al., 1994, "Segmental reflexes and ankle joint stiffness during co-contraction of antagonistic ankle muscles in man", *Experimental Brain Research*, v. 102, n. 2 (Dec), pp. 350–358. ISSN: 1432-1106. doi: 10.1007/BF00227521. Available at: <https://doi.org/10.1007/BF00227521>.

Noohi, E., Žefran, M., Patton, J. L., 2016, "A Model for Human-Human Collaborative Object Manipulation and Its Application to Human-Robot Interaction", *IEEE Transactions on Robotics*, v. 32, n. 4 (Aug), pp. 880–896. ISSN: 1552-3098. doi: 10.1109/TRO.2016.2572698.

Ong, K. W., Seet, G., Sim, S. K., 2008, "An Implementation of Seamless Human-Robot Interaction for Telerobotics", *International Journal of Advanced Robotic Systems*, v. 5, n. 2, pp. 18. doi: 10.5772/5647.

Osu, R., Gomi, H., 1999, "Multijoint Muscle Regulation Mechanisms Examined by Measured Human Arm Stiffness and EMG Signals", *Journal of Neurophysiology*, v. 81, n. 4, pp. 1458–1468. doi: 10.1152/jn.1999.81.4.1458. PMID: 10200182.

Ott, C., Mukherjee, R., Nakamura, Y., 2010, "Unified Impedance and Admittance Control". In: *2010 IEEE International Conference on Robotics and Automation*, pp. 554–561, May. doi: 10.1109/ROBOT.2010.5509861.

Paul L. Gribble, Lucy I. Mullin, N. C., Mattar, A., 2003, "Role of Cocontraction in Arm Movement Accuracy", *Journal of Neurophysiology*, v. 89, n. 5, pp. 2396–2405. doi: 10.1152/jn.01020.2002. PMID: 12611935.

Peidong Liang, Chenguang Yang, N. W., Li, R., 2016, "A Discrete-Time Algorithm for Stiffness Extraction from sEMG and Its Application in Antidisturbance Teleoperation", *Discrete Dynamics in Nature and Society*.

Perreault, E. J., Kirsch, R. F., Crago, P. E., 2002, "Voluntary Control of Static Endpoint Stiffness During Force Regulation Tasks", *Journal of Neurophysiology*, v. 87, n. 6, pp. 2808–2816. doi: 10.1152/jn.2002.87.6.2808. PMID: 12037183.

Perroto, A., 2011, *Anatomical Guide for the Electromyographer*. Charles C Thomas.

Peternel, L., Tsagarakis, N., Caldwell, D., et al., 2016, "Adaptation of robot physical behaviour to human fatigue in human-robot co-manipulation". In: *2016 IEEE-RAS 16th International Conference on Humanoid Robots (Humanoids)*, pp. 489–494, Nov. doi: 10.1109/HUMANOIDS.2016.7803320.

Peternel, L., Tsagarakis, N., Ajoudani, A., 2017, "A Human-Robot Co-Manipulation Approach Based on Human Sensorimotor Information", *IEEE Transactions on Neural Systems and Rehabilitation Engineering*, v. 25, n. 7 (July), pp. 811–822. ISSN: 1534-4320. doi: 10.1109/TNSRE.2017.2694553.

Peternel, L., Babič, J., 2013, "Learning of compliant human–robot interaction using full-body haptic interface", *Advanced Robotics*, v. 27, n. 13, pp. 1003–1012. doi: 10.1080/01691864.2013.808305.

Punnett, L., Wegman, D. H., 2004, "Work-related musculoskeletal disorders: the epidemiologic evidence and the debate", *Journal of Electromyography and Kinesiology*, v. 14, n. 1, pp. 13 – 23. ISSN: 1050-6411. Available at: <`http://www.sciencedirect.com/science/article/pii/S1050641103001251`>.

Quigley, M., Conley, K., Gerkey, B. P., et al., 2009, "ROS: an open-source Robot Operating System". In: *ICRA Workshop on Open Source Software*.

Reed, K. B., 2012, "Cooperative Physical Human-Human and Human-Robot Interaction". In: Peer, A., Giachritsis, C. D. (Eds.), *Immersive Multimodal Interactive Presence*, pp. 105–127, London, Springer London. ISBN: 978-1-4471-2754-3. doi: 10.1007/978-1-4471-2754-3_7.

Rozo, L., Calinon, S., Caldwell, D. G., 2014, "Learning force and position constraints in human-robot cooperative transportation". In: *The 23rd IEEE International Symposium on Robot and Human Interactive Communication*, pp. 619–624, Aug. doi: 10.1109/ROMAN.2014.6926321.

Sabes, P. N., Jordan, M. I., 1997, "Obstacle Avoidance and a Perturbation Sensitivity Model for Motor Planning", *Journal of Neuroscience*, v. 17, n. 18, pp. 7119–7128. ISSN: 0270-6474. doi: 10.1523/JNEUROSCI.17-18-07119.1997. Available at: <http://www.jneurosci.org/content/17/18/7119>.

Santis, A. D., Siciliano, B., Luca, A. D., et al., 2008, "An atlas of physical human–robot interaction", *Mechanism and Machine Theory*, v. 43, n. 3, pp. 253 – 270. ISSN: 0094-114X. doi: https://doi.org/10.1016/j.mechmachtheory.2007.03.003.

Siciliano, B., Khatib, O., 2016, *Springer Handbook of Robotics*. 2nd ed. Germany, Springer Publishing Company, Incorporated. ISBN: 3319325507, 9783319325507.

Siciliano, B., Sciavicco, L., Villani, L., et al., 2008, *Robotics: Modelling, Planning and Control*. Springer Publishing Company, Incorporated. ISBN: 1846286417, 9781846286414.

Slotine, J.-J. E., Li, W., 1991, *Applied nonlinear control*. Upper Saddle River, NJ, Pearson.

Spong, M., Hutchinson, S., Vidyasagar, M., 2005, *Robot Modeling and Control*. Wiley. ISBN: 9780471649908.

Spyrakos-Papastavridis, E., Kashiri, N., Childs, P. R., et al., 2018, "Online impedance regulation techniques for compliant humanoid balancing", *Robotics and Autonomous Systems*, v. 104, pp. 85 – 98. ISSN: 0921-8890. doi: https://doi.org/10.1016/j.robot.2018.03.001. Available at: <http://www.sciencedirect.com/science/article/pii/S0921889017306176>.

Stegeman, D., Hermens, H., 2007, "Standards for suface electromyography: The European project Surface EMG for non-invasive assessment of muscles (SENIAM)", (01). Available at: <https://www.med.uni-jena.de/motorik/pdf/stegeman.pdf>. Accessed: 21-02-2018.

Stulp, F., Grizou, J., Busch, B., et al., 2015, "Facilitating intention prediction for humans by optimizing robot motions". In: *2015 IEEE/RSJ International Conference on Intelligent Robots and Systems (IROS)*, pp. 1249–1255, Sept. doi: 10.1109/IROS.2015.7353529.

Takagi, A., Ganesh, G., Yoshioka, T., et al., 2017, "Physically interacting individuals estimate the partner's goal to enhance their movements", *Nature Human Behaviour*.

Thoroughman, K. A., Shadmehr, R., 1999, "Electromyographic Correlates of Learning an Internal Model of Reaching Movements", *Journal of Neuroscience*, v. 19, n. 19, pp. 8573–8588. ISSN: 0270-6474. doi: 10.1523/JNEUROSCI.19-19-08573.1999.

Tomasello, M., 2009, *Why We Cooperate*. Boston review book. MIT Press. ISBN: 9780262013598.

Townsend, E. C., Mielke, E. A., Wingate, D., et al., 2017, "Estimating Human Intent for Physical Human-Robot Co-Manipulation", *ArXiv e-prints*, (may).

Tsumugiwa, T., Yokogawa, R., Hara, K., 2002, "Variable impedance control based on estimation of human arm stiffness for human-robot cooperative calligraphic task". In: *Proceedings 2002 IEEE International Conference on Robotics and Automation (Cat. No.02CH37292)*, v. 1, pp. 644–650 vol.1. doi: 10.1109/ROBOT.2002.1013431.

van der Wel, R. P. R. D., Knoblich, G., Sebanz, N., 2011, "Let the force be with us: Dyads exploit haptic coupling for coordination." *Journal of Experimental Psychology: Human Perception and Performance*, v. 37, n. 5, pp. 1420–1431. doi: 10.1037/a0022337.

Vanderborght, B., Albu-Schaeffer, A., Bicchi, A., et al., 2013, "Variable impedance actuators: A review", *Robotics and Autonomous Systems*, v. 61, n. 12, pp. 1601 – 1614. doi: https://doi.org/10.1016/j.robot.2013.06.009.

Wen, J. T. Y., Kreutz-Delgado, K., 1991, "The attitude control problem", *IEEE Transactions on Automatic Control*, v. 36, n. 10 (Oct), pp. 1148–1162. ISSN: 0018-9286. doi: 10.1109/9.90228.

Whitsell, B., Artemiadis, P., 2017, "Physical Human-Robot Interaction (pHRI) in 6 DOF With Asymmetric Cooperation", *IEEE Access*, v. 5, pp. 10834–10845. ISSN: 2169-3536. doi: 10.1109/ACCESS.2017.2708658.

Yang, C., Ganesh, G., Haddadin, S., et al., 2011, "Human-Like Adaptation of Force and Impedance in Stable and Unstable Interactions", *IEEE Transactions on Robotics*, v. 27, n. 5 (Oct), pp. 918–930. ISSN: 1552-3098. doi: 10.1109/TRO.2011.2158251.

Yoshikawa, T., 1985, "Manipulability of Robotic Mechanisms", *The International Journal of Robotics Research*, v. 4, n. 2, pp. 3–9. doi: 10.1177/027836498500400201.

Zhou, A., Hadfield-Menell, D., Nagabandi, A., et al., 2017, "Expressive Robot Motion Timing". In: *Proceedings of the 2017 ACM/IEEE International Conference on Human-Robot Interaction*, HRI '17, pp. 22–31, New York, NY, USA. ACM. ISBN: 978-1-4503-4336-7. doi: 10.1145/2909824.3020221.

Appendix A

Human-Human Dyad Co-Manipulation Experiment - ICC

Figures A.1,A.2, A.3 display all the ICC signals acquired from 7 dyads during the HH dyad experiment described in detail in chapter 4.

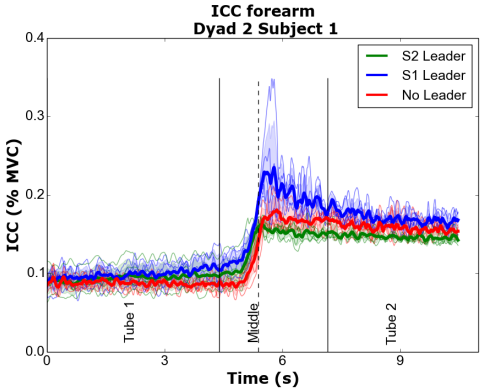

(a) Subject 1 in dyad 2.

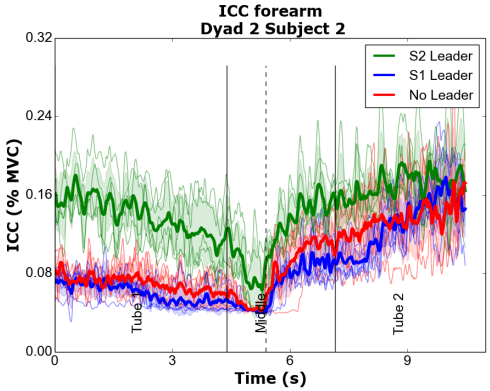

(b) Subject 2 in dyad 2.

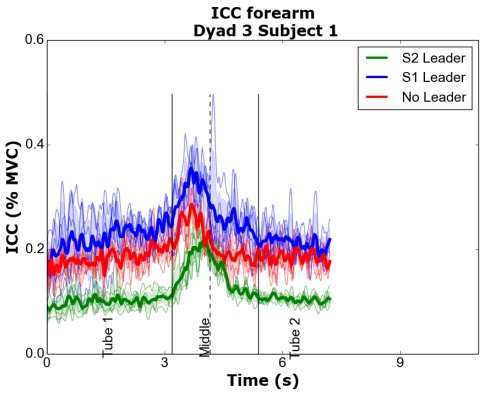

(c) Subject 1 in dyad 3.

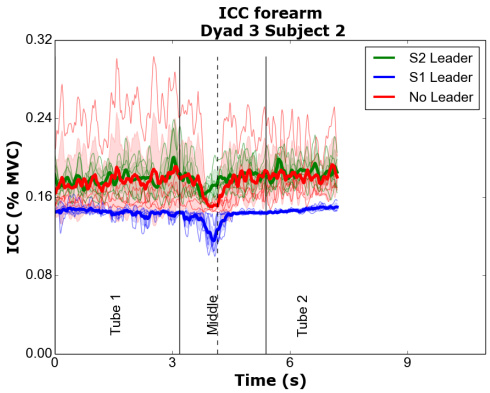

(d) Subject 2 in dyad 3.

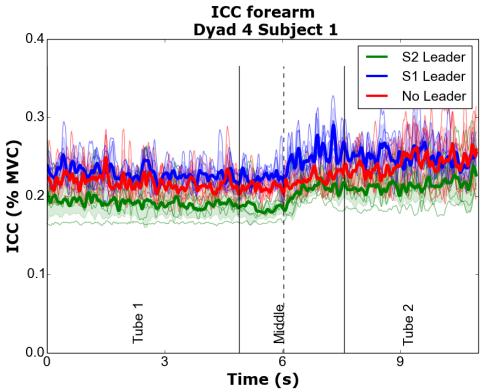

(e) Subject 1 in dyad 4.

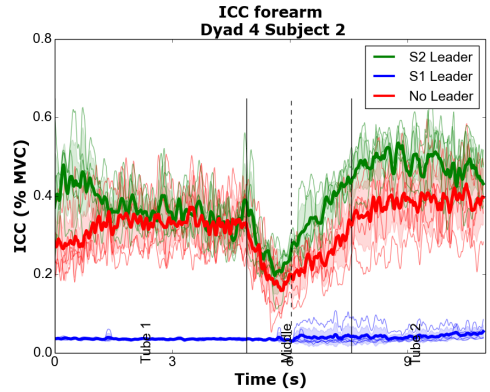

(f) Subject 2 in dyad 4.

Figure A.1: ICC acquired from forearm muscles relative to the wrist joint. Taken from dyad 2 to dyad 4

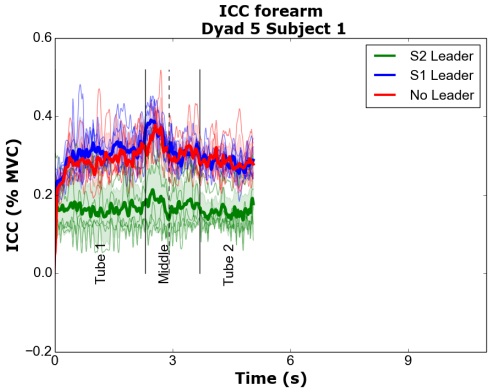

(a) Subject 1 in dyad 5.

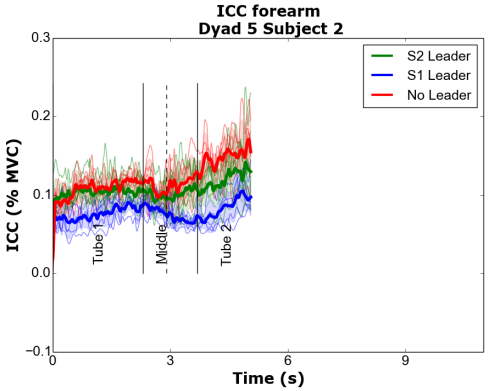

(b) Subject 2 in dyad 5.

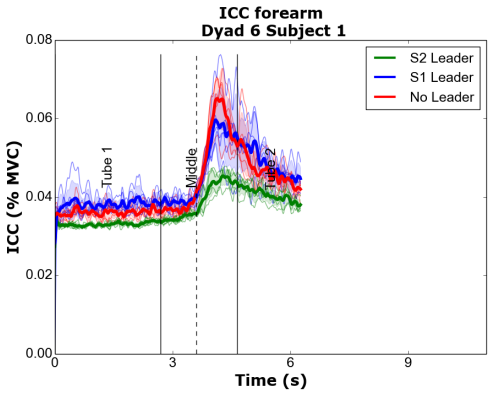

(c) Subject 1 in dyad 6.

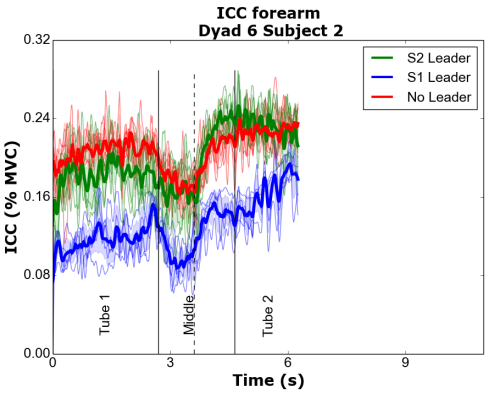

(d) Subject 2 in dyad 6.

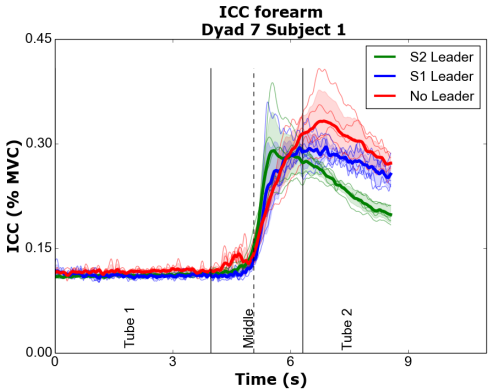

(e) Subject 1 in dyad 7.

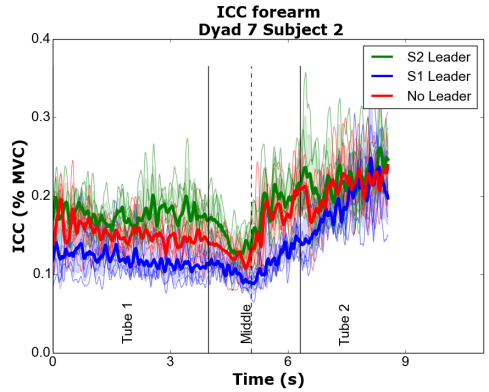

(f) Subject 2 in dyad 7.

Figure A.2: ICC acquired from forearm muscles relative to the wrist joint. Taken from dyad 5 to dyad 7

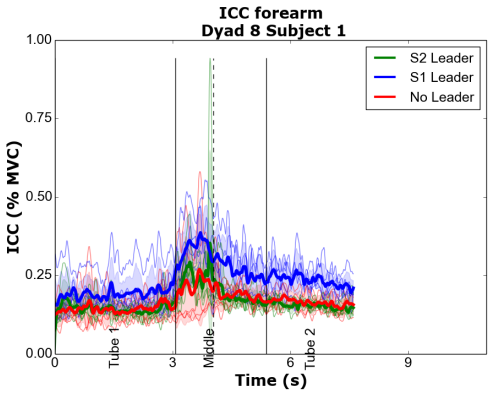

(a) Subject 1 in dyad 8.

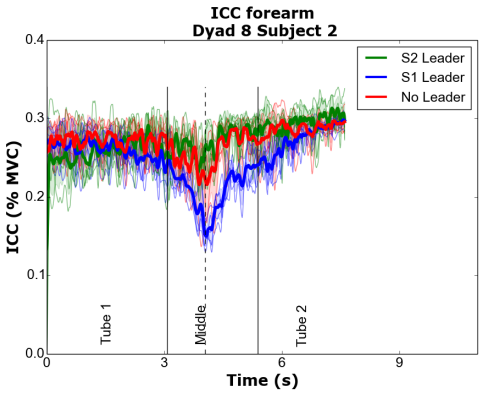

(b) Subject 2 in dyad 8.

Figure A.3: ICC acquired from forearm muscles relative to the wrist joint. Taken from dyad 8

Appendix B

Single Human Manipulation Experiment - ICC

Figure B.1 displays all the ICC signals acquired from 6 participants during the single human experiment described in detail in chapter 4.

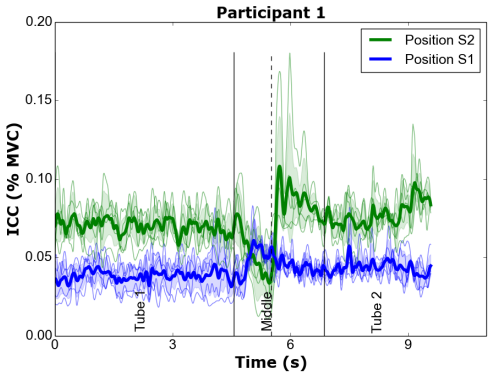

(a) Participant 1.

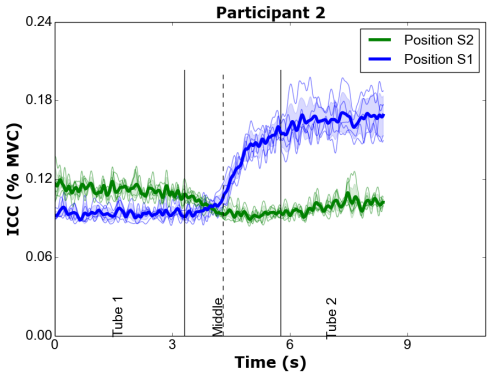

(b) Participant 2.

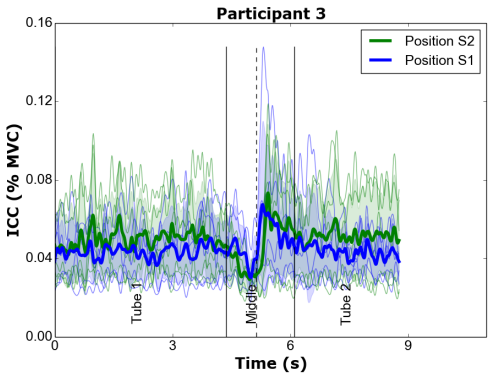

(c) Participant 3.

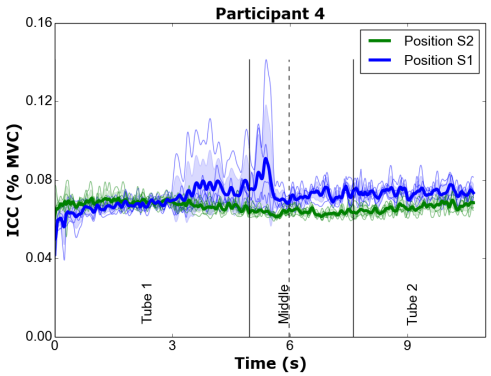

(d) Participant 4.

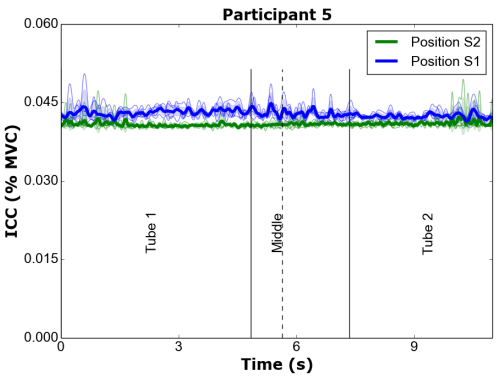

(e) Participant 5.

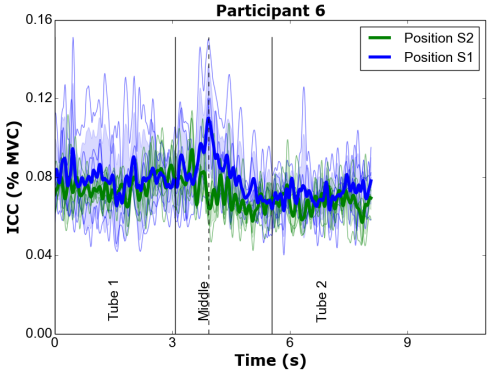

(f) Participant 6.

Figure B.1: ICC acquired from a given participant

Appendix C

Human-Human Dyad Co-Manipulation Experiment - Planar Trajectory

Figures C.1, C.2 displays all of the planar trajectories from the barycenter of the position of the hand markers acquired from every dyad during the HH dyad experiment described in detail in chapter 4.

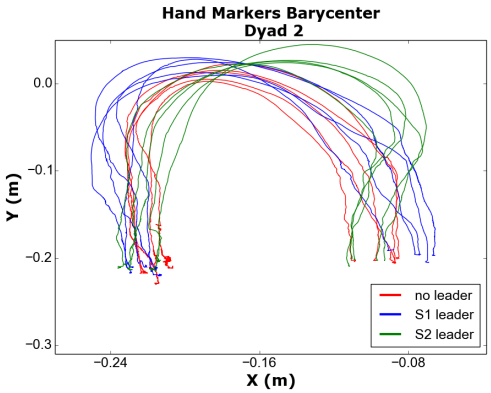

(a) Subjects in dyad 2.

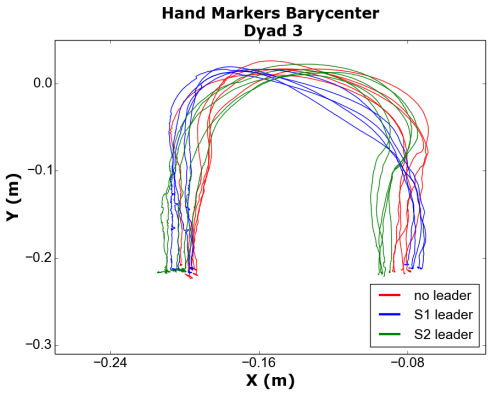

(b) Subjects in dyad 3.

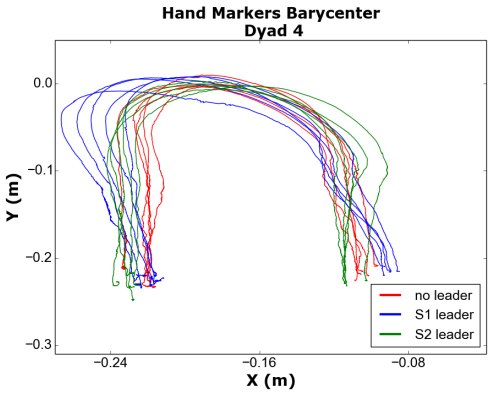

(c) Subjects in dyad 4.

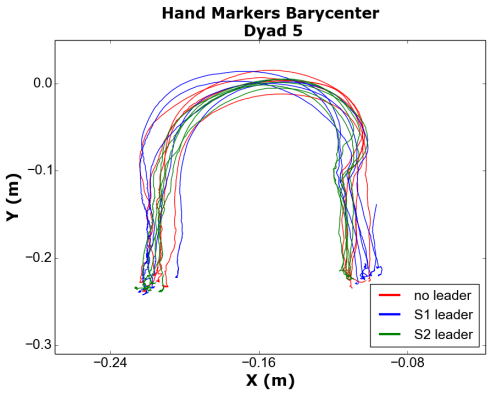

(d) Subjects in dyad 5.

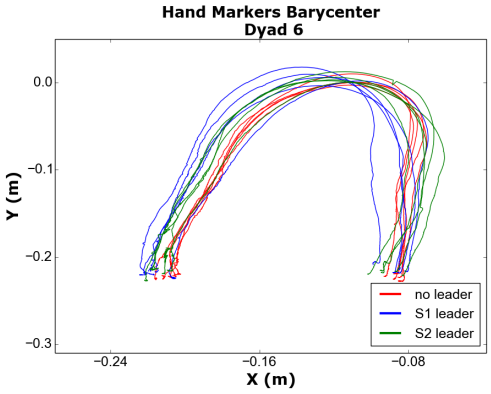

(e) Subjects in dyad 6.

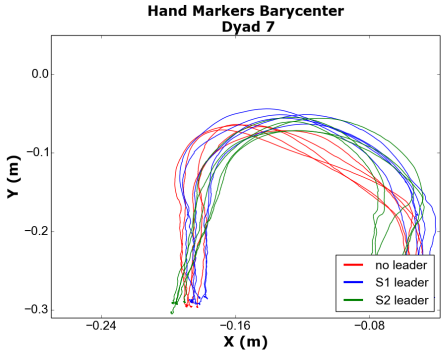

(f) Subjects in dyad 7.

Figure C.1: Trajectory of the barycenter of the position of the hand markers from both subjects in dyads 2 to 7.

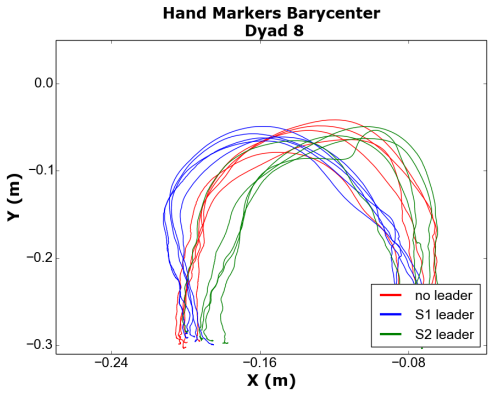

(a) Subjects in dyad 8.

Figure C.2: Trajectory of the barycenter of the position of the hand markers from both subjects in dyad 8.

Appendix D

Single Human Manipulation Experiment - Planar Trajectory

Figure D.1 displays all of the planar trajectories from the barycenter of the position of the hand markers acquired from every participant during the single human experiment described in detail in chapter 4.

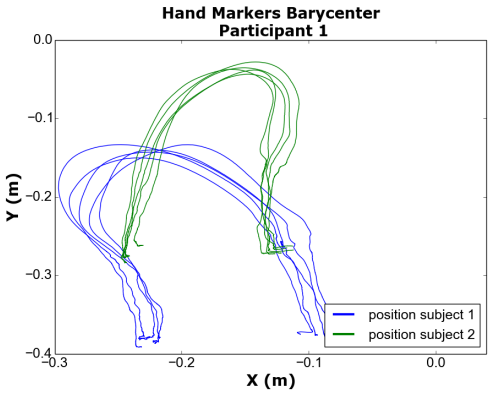

(a) Participant 1.

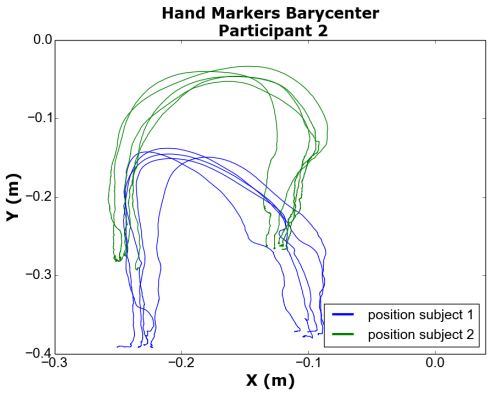

(b) Participant 2.

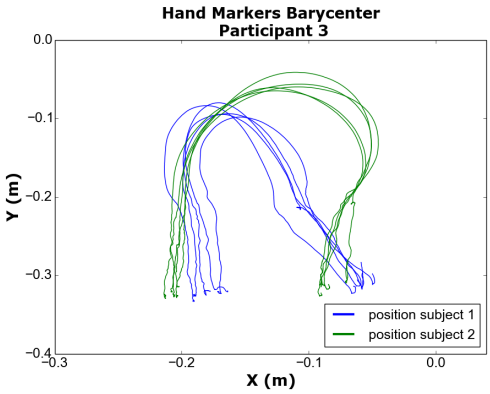

(c) Participant 3.

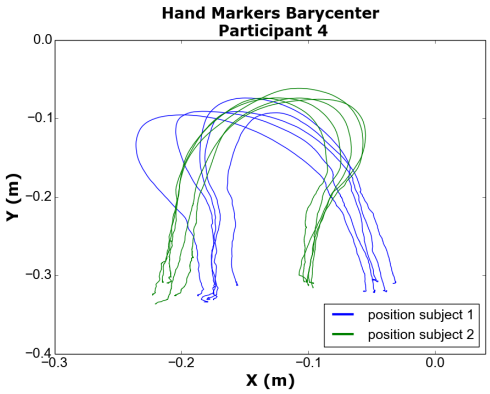

(d) Participant 4.

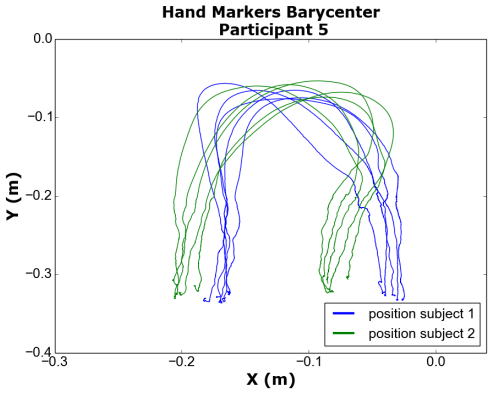

(e) Participant 5.

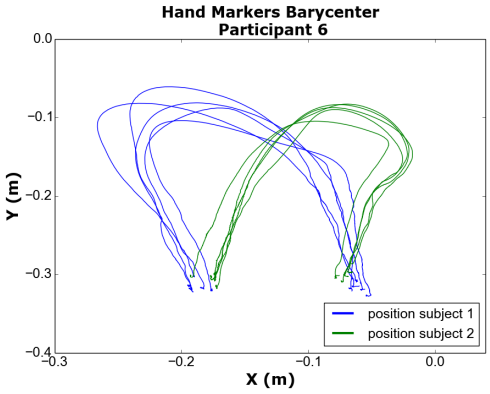

(f) Participant 6.

Figure D.1: Planar trajectory (X-Y) of the barycenter of the position of the hand markers from a given participant in the single human experiment

Appendix E

Stability in Impedance/Admittance Control

The control objective of a impedance/admittance controller is to obtain a desired dynamic relationship between a external wrench (force and torque) applied to the robot EEF, and the EEF pose (position and orientation). Hereafter, it is considered only the dynamic relationship between the external force and the EEF position.

The closed loop dynamic is defined by (see also 2.66):

$$\Lambda_d \ddot{e}_r + D_d \dot{e}_r + K_d e_r = F_{ext} \tag{E.1}$$

where $\Lambda_d \in \mathbb{R}^{3\times3}$ is the desired apparent inertia; $D_d \in \mathbb{R}^{3\times3}$ is the desired damping; and $K_d \in \mathbb{R}^{3\times3}$ is the desired stiffness, and $e_r(t) = x_e(t) - x_r(t)$. If Λ_d, D_d, K_d are constant, symmetric, and positive definite, then (E.1) is stable by the Routh-Hurwitz criteria.

E.1 Varying Desired Stiffness and Damping

If $K_d(t)$ and $D_d(t)$ are time-varying, the desired impedance is given by:

$$\Lambda_d \ddot{e}_r + D_d(t) \dot{e}_r + K_d(t) e_r = F_{ext} \tag{E.2}$$

It is possible to try to verify the stability of (E.2) with the Lyapunov candidate function V_1:

$$2V_1(e_r, \dot{e}_r, t) = e_r^\top K_d(t) e_r + \dot{e}_r^\top \Lambda_d \dot{e}_r \tag{E.3}$$

Then, deriving V_1 with respect to time, along the solution of (E.2), and consid-

ering $F_{ext} = 0$:

$$\dot{V}_1 = -\dot{e}_r^\top D_d \dot{e}_r + \frac{1}{2} e_r^\top \dot{K}_d(t) e_r \tag{E.4}$$

Therefore, $\dot{V}_1$ is only negative definite if $\dot{K}_d$ also is. In addition, if $e_r \neq 0$, and $\dot{K}_d > 0$, there is a potential energy injection into the system which could cause unstable behavior (Kronander and Billard, 2016).

In Kronander and Billard (2016), the authors proposed the following Lyapunov candidate function, V_2:

$$2V_2(e_r, \dot{e}_r, t) = (\dot{e}_r + \gamma e_r)^\top \Lambda_d (\dot{e}_r + \gamma e_r) + e_r^\top \beta(t) e_r \tag{E.5}$$

where $\gamma \in \mathbb{R}^+$, and $\beta(t) \in \mathbb{R}^{3\times 3}$ is symmetric and positive definite. V_2 is then used to verify the stability of eq. (E.2). And the derivative of $V_2(t)$ is given by:

$$\dot{V}_2 = (\dot{e}_r + \gamma e_r)^\top \Lambda_D (\ddot{e}_r + \gamma \dot{e}_r) + e_r^\top \beta(t) \dot{e}_r + \frac{e_r^\top \dot{\beta} e_r}{2} \tag{E.6}$$

$$\dot{V}_2 = (\dot{e}_r + \gamma e_r)^\top \Lambda_D \ddot{e}_r + (\dot{e}_r + \gamma e_r)^\top \Lambda_D \gamma \dot{e}_r + e_r^\top \beta(t) \dot{e}_r + \frac{e_r^\top \dot{\beta} e_r}{2} \tag{E.7}$$

Substituting eq. (E.1) with $F_e = 0$ into eq. (E.7):

$$\dot{V}_2 = (\dot{e}_r + \gamma e_r)^\top (-D_d(t)\dot{e}_r - K_d e_r) + (\dot{e}_r + \gamma e_r)^\top \Lambda_D \gamma \dot{e}_r + e_r^\top \beta(t) \dot{e}_r + \frac{e_r^\top \dot{\beta} e_r}{2} \tag{E.8}$$

$$\dot{V}_2 = -\dot{e}_r^\top D_d(t)\dot{e}_r - \dot{e}_r^\top K_d(t) e_r - e_r^\top \gamma D_d(t)\dot{e}_r - e_r^\top \gamma K_d(t) e_r + \dot{e}_r^\top \Lambda_d \dot{e}_r + e_r^\top \gamma^2 \Lambda_d \dot{e}_r + e_r^\top \beta(t)\dot{e}_r + \frac{e_r^\top \dot{\beta} e_r}{2} \tag{E.9}$$

Rewriting and rearranging terms:

$$\dot{V}_2 = \dot{e}_r^\top (-D_d(t) + \gamma \Lambda_d)\dot{e}_r + e_r^\top (-K_d(t)\gamma + \frac{\dot{\beta}}{2}) e_r + e_r^\top (-K_d(t) - \gamma D_d(t) + \gamma^2 \Lambda_d + \beta(t))\dot{e}_r \tag{E.10}$$

In order to eliminate the cross-terms in eq. (E.10), $\beta(t)$ is defined as:

$$\beta(t) := K_d(t) + \gamma D_d(t) - \gamma^2 \Lambda_d \tag{E.11}$$

whose derivative is

$$\dot{\beta}(t) = \dot{K}_d(t) + \gamma \dot{D}_d(t) \tag{E.12}$$

Substituting $\beta(t), \dot{\beta}(t)$ into $\dot{V}_2$:

$$\dot{V}_2 = \dot{e}_r^\top(-D_d(t) + \gamma\Lambda_d)\dot{e}_r + e_r^\top\left(-K_d(t)\gamma + \frac{\dot{K}_d(t)}{2} + \frac{\dot{D}_d(t)\gamma}{2}\right)e_r \tag{E.13}$$

Therefore, $\dot{V}_2$ is negative definite if, and only if:

$$-D_d(t) + \gamma\Lambda_d < 0 \tag{E.14}$$

$$-2\gamma K_d(t) + \gamma\dot{D}_d(t) + \dot{K}_d(t) < 0 \tag{E.15}$$

which according to the Lyapunov's stability theorem (Khalil, 2002) are also sufficient conditions for the global asymptotic stability of the closed-loop impedance model with varying desired stiffness and damping (E.2).